MULTI-MODE INSTABILITIES ARISING IN HYPERSONIC FLOW CONDITIONS FOR AEROSPACE APPLICATIONS

by

Tony Liang

A dissertation submitted to the Faculty of the University of Delaware in partial fulfillment of the requirements for the degree of Doctor of Philosophy in Mechanical Engineering

Winter 2024

MULTI-MODE INSTABILITIES ARISING IN HYPERSONIC FLOW CONDITIONS FOR AEROSPACE APPLICATIONS

by

Tony Liang

Approved: ______________________________
Greg Chirikjian, Ph.D.
Chair of the Department of Mechanical Engineering

Approved: ______________________________
Levi T. Thompson, Ph.D.
Dean of the College of Engineering

Approved: ______________________________
Louis F. Rossi, Ph.D.
Vice Provost for Graduate and Professional Education and
Dean of the Graduate College

I certify that I have read this dissertation and that in my opinion it meets the academic and professional standard required by the University as a dissertation for the degree of Doctor of Philosophy.

Signed: ______________________________

Joseph J. Kuehl, Ph.D.
Professor in charge of dissertation

I certify that I have read this dissertation and that in my opinion it meets the academic and professional standard required by the University as a dissertation for the degree of Doctor of Philosophy.

Signed: ______________________________

Ajay Prasad, Ph.D.
Member of dissertation committee

I certify that I have read this dissertation and that in my opinion it meets the academic and professional standard required by the University as a dissertation for the degree of Doctor of Philosophy.

Signed: ______________________________

Tyler Van Buren, Ph.D.
Member of dissertation committee

I certify that I have read this dissertation and that in my opinion it meets the academic and professional standard required by the University as a dissertation for the degree of Doctor of Philosophy.

Signed: ______________________________

Fabrice Veron, Ph.D.
Member of dissertation committee

ACKNOWLEDGEMENTS

I am extremely grateful and privileged for the opportunity to study, learn and interact with the countless staff and students at the University of Delaware. This work and other projects were only possible with the support and contributions by members of the university, college and department.

Foremost, I would like to express my extreme gratitude and appreciation for my advisor, Professor Joseph Kuehl, for giving me the opportunity to study under him in such a complex and demanding field as hypersonics and in particular, the arduous and daunting topic of boundary layer transition. His patience, encouragement and direction has had a profound impact on my development. I consider myself beyond fortunate to have him as my advisor during my time here.

I would also like to thank Dr. Armani Batista and Dr. Arham Amin Khan for their kind assistance and advice during the early part of my studies to help me get oriented and established as member of the research group. I cherish and am grateful for the countless of hours spent discussing both technical and nontechnical matters. I am above all grateful for their friendship. Many thanks to thank Professor Tyler Van Buren and the members of his research group for opening up their lab and extending their friendship to me. Their support and guidance has provided nourishment for both my professional and personal development.

I would like to thank my family for their continual love and support and especially my dog Ophie for her companionship over the years. Their understanding and encouragement has motivated me to undertake and complete this momentous work. I would not be where I am at today without them.

And finally, many thanks to coffee.

TABLE OF CONTENTS

LIST OF TABLES

LIST OF FIGURES

ABSTRACT

Research in hypersonic aerodynamics is important in understanding the practicality of sustained high-speed flight and the design parameters of such vehicles. Hypersonic boundary layer transition is dominated by the presence of various disturbance (Mack) modes present within the boundary layer which undergo modal growth and eventually transition the flow to turbulence. Understanding the dynamics of these modes and their interactions within the boundary layer can bridge the knowledge gaps in the fundamental causes of heat transfer, friction drag, lift and other properties which become critically important in hypersonic flight

The aim of this research is to perform an analytical study utilizing computational fluid dynamics (CFD) coupled with boundary layer stability analysis employing linear stability theory (LST) and parabolized stability equations (PSE) to help understand the dynamics of Mack modes and their nonlinear interactions. One question to be studied is the source of energy driving the 1st and 2nd mode instabilities. A characterization of the energetics of the 1st and 2nd modes was performed at various flow conditions to further understand physical mechanisms governing the modal growth pathway to transition, and was shown that the traditional 1st mode definition is incomplete. A design study into a geometry conducive to 1st and 2nd mode interactions was performed and investigated. With such a geometry, the dynamics between a 1st mode dominated boundary layer with an existing 2nd mode was investigated. Finally, with understanding of the thermoacoustic interpretation of the 2nd mode, a impedance boundary condition is applied to a canonical conical geometry in an attempt to analyze its effect on certain unstable waves within the boundary layer. Understanding the dynamics of these modes and their interactions within the boundary layer can bridge fundamental knowledge gaps governing various phenomena in hypersonic flight.

Chapter 1

INTRODUCTION & BACKGROUND

1.1 History & Motivation

Ever since the advent of powered flight, developments have been motivated by the urge to go faster, further and higher. Over the span of 50 years, within a typical human lifespan, one would have seen aeronautical advances ranging from the development of the first motor powered aircraft to commercial airliners, jets, rockets and early orbital satellites. From the first flight of the 1903 Wright Flyer above a beach in Kitty Hawk, South Carolina, to the breaking of the sound barrier by Chuck Yeager in the Bell X-1 over the Mojave 44 years later, humans have sought to expand their reach through flight.

With technological progress and increasingly higher flight speeds possible, the thermodynamic state of the flow becomes critically relevant. Engineers sought to correlate the vehicle dynamics to the thermodynamics of the flow medium via the Mach number. Named after physicist Ernst Mach, this dimensionless number relates flow velocity relative to the local speed of sound, and hence the thermodynamical state of the flow medium. The relevance of Mach numbers increased dramatically in the decades near the advent of faster-than-sound flight as flow compressibility effects become more pertinent. The first manned sustained supersonic fight occurred on October 14, 1947 with the Bell X-1 reaching Mach 1.06 [17], which experienced strong aerodynamic and thermal loading as well as decreased control authority previously uncommon in the subsonic regime. These new flight characteristics motivated efforts in understanding the foundational physics and phenomena associated with these flight conditions in compressible flow. New design features such as swept/delta wings, high thrust propulsion systems and new materials able withstand aerothermal heating were developed from these efforts. The design differences as vehicles achieve greater speeds where these compressibility effects become more and more important can be seen in examples such as the North American F-86 Sabre to McDonnell Douglas F-4 Phantom II to The Concorde.

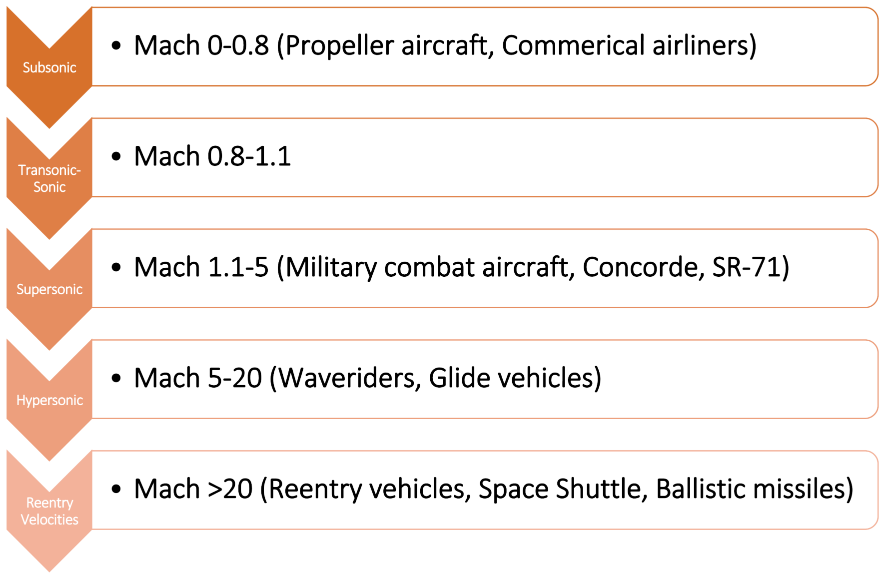

Figure 1.1: Mach number ranges for a variety of flight regimes

After Mach 5, one enters the realm of hypersonic flight. Here the aforementioned effects associated with supersonic flight are amplified, such that sustained cruise hypersonic flight becomes difficult to achieve. This however, has not discouraged efforts in exploring flight at these daunting speeds and conditions. Hypersonic flight itself has been experimented with extensively ever since the end of the Second World War. From the early unmanned testing of the V-2/WAV Corporal rocket of post-war USA to Yuri Gagarin in Vostok 1 of the USSR, sustained hypersonic flight both crewed and uncrewed have been explored with. Other well known examples include the development and flight of the North American X-15 in the late 1950-60s, which was one of the first manned hypersonic vehicles capable of exceeding Mach 6, launch and reentry of intercontinental ballistic missiles (ICBMs) developed during the Cold War, the space shuttle during the 1980s-2010s, the scramjet powered X-43 Hyper-X and most recently, the development of various glide vehicles and wave riders. Future applications of sustained hypersonic flight can allow for substantially reduced travel travel time for commercial flights and the safe re-entry of vehicles into the atmospheres of extraterrestrial bodies [18, 3].

Research in hypersonic aerodynamics is important in understanding the practicality of achieving sustained high-speed flight and the design parameters of such vehicles. Early on, the differences in heating and drag between the laminar and turbulent regions of the boundary layer over the vehicle body were noted, and the benefits of extending the laminar regime has been recognized. Thus, the study of transition methods from these two different flow regimes in the boundary layer can bridge the knowledge gaps in the fundamental causes of heat transfer, friction drag, lift and other properties of the system which become critically important in hypersonic flight. Understanding the various flow phenomenon in these extreme conditions can yield great advances in aerospace flight technologies, which in-turn can have a monumental impact on the space & aeronautical industries.

1.2 Hypersonics Background

Hypersonic aerodynamics is commonly considered distinct from traditional subsonic and supersonic aerodynamics. With the extremely high energy flow environment, one must now consider the importance of high temperature real gas physics, low density effects, shock and entropy layers and thermochemical interactions. The interaction between the aerobody and flow medium induces strong aerodynamic forces and consequently aerothermal heating. The thermal loading becomes so great in hypersonic conditions that design configurations are greatly influenced by this factor. Variations in vehicle design can have a drastic effect on the types of drag experienced by the vehicle. In slender geometric bodies for example, the main source of drag is from skin friction, whereas in blunt bodies, drag is primarily due to high pressures behind the strong bow shockwave.

Since the flow characteristics between hypersonic and supersonic flows are remarkably different, and understanding that the flow largely dictates vehicle design, the design of hypersonic vehicles are in turn drastically different than those of sub-supersonic vehicles. The various components of the subsonic-supersonic aircraft are clearly visually identifiable, such as its fuselage, wings and engines, as these components are not strongly coupled with each other [18]. However these physical characteristics become ambiguous for hypersonic vehicles. For instance, hypersonic vehicles experience strong bow shocks from the compression of air and results in a large change in pressure, temperature and density in the flow medium. Since lift is primarily provided by the high pressure bow shock against the under-surface of this geometry, defined wings are unnecessary. Also, this consequently can be utilized in specialized engines such as ramjets or scramjets to propel the craft to such high velocities, which are mounted as such to utilize this unique flow phenomena. In this new class of vehicle design, the components responsible for the mechanisms of lift, propulsion and control are thus integrated into the air-frame [18].

Aerodynamic heating and shear stress/skin friction drag are some of the most important aspects in hypersonic vehicle design. Towards the strong shock region, the highly compressible inviscid area in the shock layer serves as an important source of general heating in the system. As the flow passes through this region, a sharp increase in temperature and density occurs which can then be conducted onto the body. The extremely high energy flow also enters the boundary layer and is then slowed by the viscous effects. The high kinetic energy dissipates into internal energy of the gas that is then transferred onto the body through thermal conduction and radiation [18]. Understanding these mechanisms is important as, in addition to contributing to the thermal load of the vehicle, they are also strongly correlated to the drag experienced on the body and can influence the stability profile of the vehicle.

1.2.1 Entropy Layers

With highly curved shock layers, as commonly seen on blunted bodies, there exists a region of flow near the blunted section where there is a large entropy gradient. Flows with constant entropy when comparing between the streamlines are known as homentropic flows and these are commonly found in the freestream flow in front of the shock. Flows where there are no changes in entropy along the entire length of the streamline are known as isentropic flows, and are generally found behind the shock [3]. Streamlines crossing normal shocks experience greater changes in entropy than ones crossing oblique shocks [3]. Thus, for blunted nose geometries where there exists a strong normal shockwave, strong entropy density gradients (hence entropy layers) appear. That is, a streamline that enters the shock near the stagnation point of the body (i.e. near the normal shock), experiences a greater entropy than a streamline entering where the shock is oblique, hence a strong entropy layer occurs.

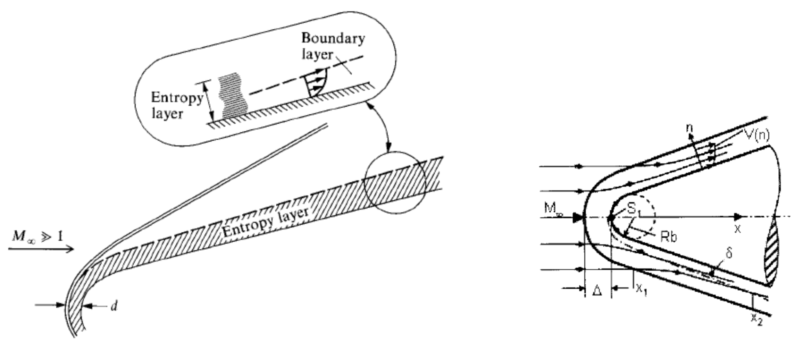

Figure 1.2: Left: Depiction of the shock and entropy layer along with its interaction with the boundary layer [2]. Right: Schematic of the streamlines near the nose; notably depicting the stagnation point (S_1), location where a streamline crosses the shock (x_1) and enters the boundary layer (x_2) [3]

The formed entropy layer spans a certain distance downstream along the body before it is "swallowed", which is generally classified when the entropy layer and boundary layer runs parallel to each other. An important aspect in the study of entropy layers in hypersonic flow is its swallowing length. The entropy layer at some distance from the nose, interacts with the formed boundary layer. These regions of strong entropy changes can have important influences on the thermodynamic conditions of the flow, which can have an effect on the boundary layer.

1.2.2 Thin Shock Layers

Flows over common hypersonic geometries exhibit oblique shocks where density increases over the shock as the Mach number is increased. With an increase in density behind the shock, reciprocates an decrease in volume, hence the height of the shock from the body also decreases [18]. This region of flow is commonly referred to as the shock layer, can be very small at higher Mach numbers and can be estimated utilizing $\theta - \beta - Mach$ diagrams. This usually also results in a smaller boundary layer height and can consequently induce in shock-boundary layer interactions (SBLI) which is itself another vastly complex problem [18].

1.2.3 High Temperature Gas Dynamics

Under certain high energy flow environments, the kinetic energy dissipated by the viscous boundary layer creates very high temperatures and enthalpies which may cause molecular dissociation and ionization of gas species. Generally, these types of flows occur with very high Mach numbers, velocities and shock temperatures, as shown in figure 1.3.

These types of flow environments can create a chemically reacting boundary layer along the body where chemical reacting dynamics and molecular vibrational energies must also be considered. If the change in time, in comparison with the movement of the flow particles with the chemical/vibrational reactions, is very small, this is considered a flow in chemical equilibrium, while if the opposite is true, this is considered a chemical non-equilibrium flow [18].

1.3 Progress on High Speed Boundary Layer Transition Theory

As noted by White [6], a boundary layer flow shifting over space and time from laminar to turbulence indicates a transition in the stability of the flow. Stability itself can be defined as the susceptibility of a system to withstand a disturbance and still

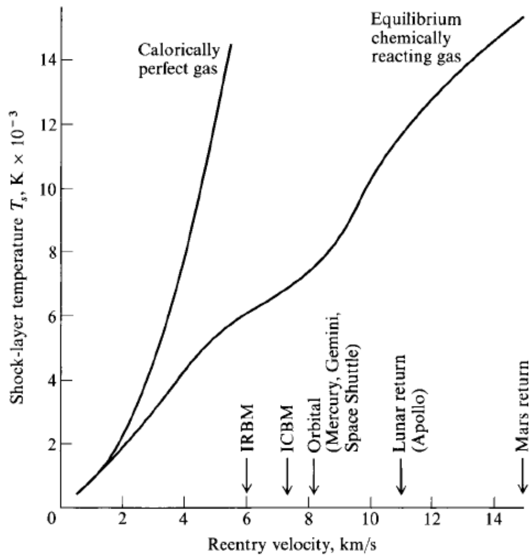

Figure 1.3: Temperatures and velocities of various scenarios and their relations with gas regimes [4]

return to its original state. If so, it is considered stable, while if not, it is considered an unstable system. Work on inviscid flows by Lord Rayleigh in the late 1800s, discovered the presence of an inflection point within flow profiles which can be correlated to disturbances that either grow and lead to instability or dampen out and remain stable [19, 20]. The introduction of the concept of boundary layers and its respective stability, along with its relationship with Reynolds numbers, by Prandtl, Taylor, Tollmein, Schlichting and others, brought to focus the importance of transition mechanisms. These works further expanded the theories behind transition of the boundary layer in various types of flows, in both the viscid and inviscid domains, through analytical and experimental work, and laid the foundation for more advanced studies [9].

In 1946, Lees & Lin [21], under advisement by Theodore Von Kármán, expanded on the theory behind the Rayleigh inflection theorem for stability and developed what is commonly known as the generalized inflection point theory, which is considered a necessary criterion for instability in high-speed locally parallel flow [9, 20]. Later, with the increasing relevance of high speed flow stability and transition in the field of super/hyper-sonic aeronautics, research work demanded the development of new mathematical and computational frameworks to handle more complex problems. Works from Lee [21], Mack [9], Bertolotti [22], Gaster [23], Malik [24], Schmid [25], Herbert [26] all investigated methods of analyzing and quantifying high speed inviscid and viscous flow stability utilizing various schemes in linear stability theory (LST) and parabolized stability equations (PSE) which can be solved by algorithms and programs on digital computers. Later, more modern work by Reed [27], Federov [28], Fasel [29], Saric [30], Tumin [31], Zhong [32], Schneider [33], Juliano [34], Kuehl [35], Balakumar [36], Candler [37], Paredes [38] and others in the latter part of the 20th century and early 21st century, investigated some of the more common instability mechanisms experienced during sustained hypersonic flight and verification of experimental studies incorporating aforementioned analysis methods and more modern computational techniques such as compressible reacting flow CFD, newer discretization methods, turbulence models and stability solvers.

1.4 Transition Mechanisms

The physical processes which describes transition phenomena are complex and has multiple routes as depicted in figure 1.5. The types of instabilities which may appear depends on the Reynolds/Mach numbers, geometry parameters, surface roughness, etc. and can be modulated by the shock, pressure and temperature gradients, surface mass transfer and more [39]. Generally, external disturbances relative to the boundary layer such as freestream sound waves, vorticities, temperature and density gradients, etc. may enter the boundary layer itself and provide an initial amplitude disturbance. These disturbances vary throughout the boundary layer and are evanescent as it approaches the freestream flow [9].

The pathways to transition may be predicted depending upon this initial amplitude disturbance as seen in figure 1.5. The transition pathways for extremely minuscule initial disturbances, such as those typically experienced in sustained cruise flight, can be described with pathway A. These disturbances experience modal growth until its

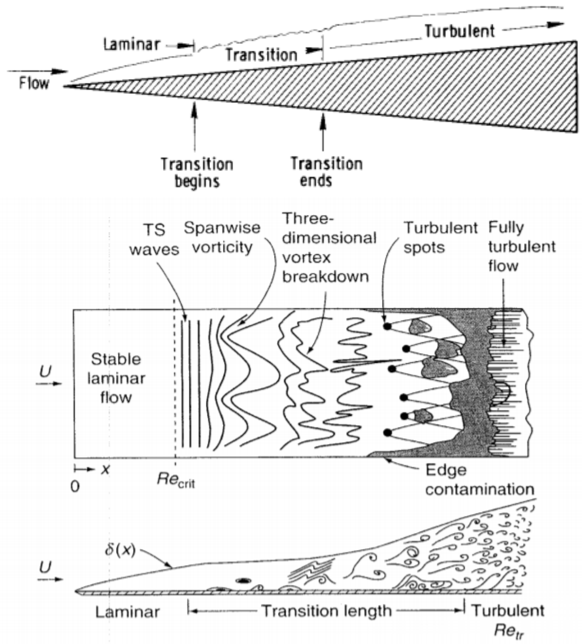

Figure 1.4: Top: Boundary layer transition denoting laminar, transition and turbulence stages [5], Bottom: Detailed boundary layer transition process on a flat plate [6]

amplitude is able to initialize various nonlinear interactions and secondary mechanisms which eventually breaks down the flow into turbulence [40, 28]. Transition following this pathway are commonly referred to as natural transition.

Other pathways, such as B and C are associated with transient (nonmodal) growth, occur when two non-orthogonal modes interact, which then undergoes algebraic growth which can then develop into larger secondary instabilities and eventually trip the flow to turbulence [41]. Paths D and E primarily represents transition commonly seen in internal flows or cases where there exists an high enough initial amplitude such that it forces the transition process without encountering any linear regimes [28]. These pathways are are considered forced transition and are common in noisy flight environments.

For 2D boundary-layers, some of the various instability mechanisms which can arise and can trigger transition are: first Mack modes (historically understood to be viscous instabilities akin to Tollmien-Schlichting waves) and second Mack modes (thermoacoustic instability). In 3D boundary layers, crossflow waves and Görtler waves

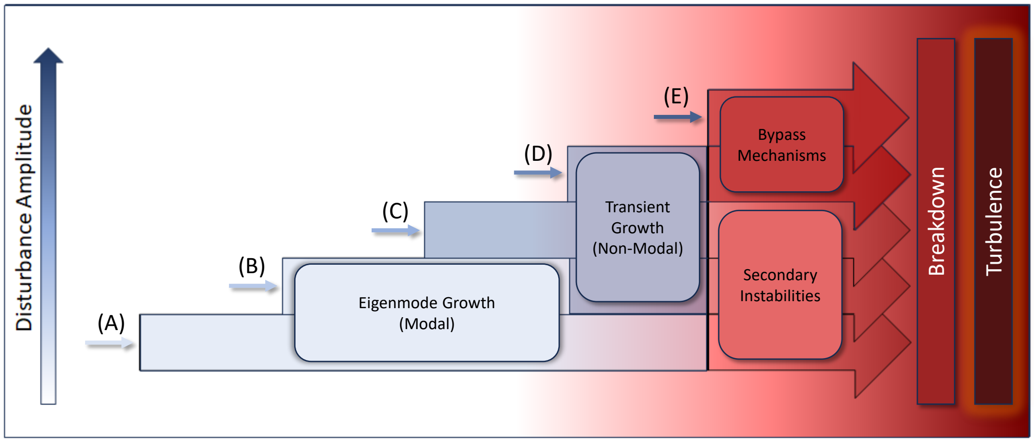

Figure 1.5: Laminar-turbulent boundary layer transition pathways, redrawn from Morkovin [7]

(associated with vorticies induced by geometric variations on the body) become transition mechanisms of concern. For this study, pathway A is studied due to its strong association with natural transition from unstable first and second modes commonly encountered in flight experiments.

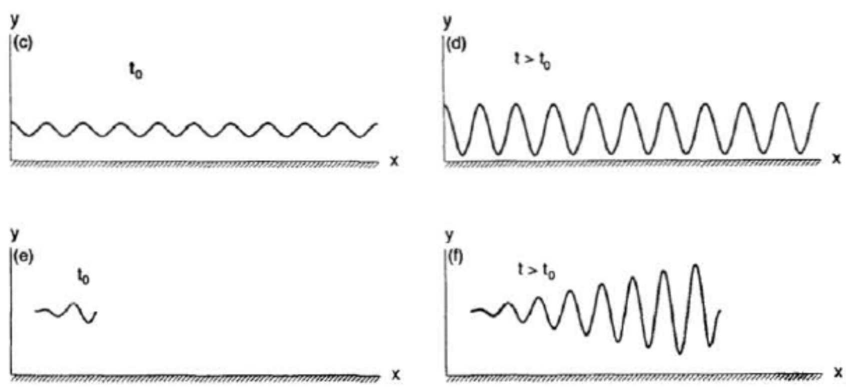

Figure 1.6: Excerpt from Schmid et al. [8] figure 1.3, depicting temporal (c,d) and spatial (e,f) evolution of disturbances

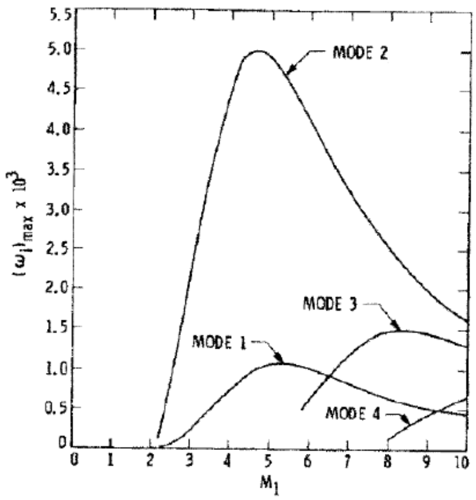

Figure 1.7: Mach number vs. amplification rate of the first four Mack modes [9]

1.4.1 Tollmien- Schlichting waves

Tollmein-Schlichting (TS) instability is considered to be a viscous type instability which generally occurs in boundary layer flows where viscosity acts as the source of energy gain driving the instability rather than as an energy sink. The current general understanding of TS wave instability is that it arises from a phase shifting between the Reynolds stress $u'v'$ within the shear layer near the wall such that these terms are no longer orthogonal to each other and are the source of energy for the disturbance.

With an energetics analysis, the Reynolds stress can be defined as the average of $u'v'$ over one wavelength in the x direction [42, 9, 43]:

$$\tau = \int_{x}^{x+\frac{2\pi}{\alpha}} u'v'dx \tag{1.1}$$

The disturbance state variables are decomposed to a viscous and inviscid solution, ϕ_v and ϕ_i such that $\phi = \phi_v + \phi_i$ satisfies the equations of motion. The boundary conditions for u are such that on the wall :

$$
\begin{aligned}
u(0) &= u_i(0) + u_v(0) \\
u(y) \to u_i(y) & \qquad \text{as} \qquad y \to \infty
\end{aligned}
$$

For invisicid flows, u' and v' are 90° out of phase and thus $\tau = 0$. However for the viscous velocity terms, the u and v will be 135° out of phase and this yields a non-zero τ which is shown intensively in works by Mack and Saric [44, 43]. That is, the presence of viscosity effects, particularly near the wall, motivates the implementation of the no-slip condition on the wall which can induce a phase shift between the disturbance velocity components. The phase shifting between the streamwise and wall normal disturbance velocity components near the wall yields a positive Reynolds stress and acts as an energy source for the instability.

1.4.2 1st Mack Mode

The 1st Mack Mode oblique instability is traditionally referred to as the supersonic analogy to the Tollmien–Schlichting instability. However recent work as described in chapter 3 indicates that this definition may not be complete. The classical interpretation for the energy source of 1st mode waves is akin to that of TS waves, which are driven by the non-orthogonality between the streamwise and normal disturbance velocity components induced by the viscous no-slip condition on the wall. That is, it is thought that the source of energy driving this instability arises only from the non-zero advective Reynolds stress from the phase shifted velocity components at the wall.

However a new study by Liang et al. [1], has indicated that this traditional definition of the 1st mode might not be complete, as it has been shown that, while TS waves and 1st modes are both driven by the phase shifting between the velocity based Reynolds stresses, a contribution from what is referred to as the thermoacoustic Reynolds stress is also seen for 1st modes, which is based on pressure and temperature.

These energy source terms appear to dominate in the vicinity of the generalized inflection point, which can be off the wall, and near the critical layer (area of flow in the boundary layer where the disturbance phase speed is equal to the mean flow velocity).

In other words, it appears that with an analysis using energy methods on 1st mode dominated flows, the thermoacoustic and velocity advective Reynolds stresses both influence the energetics which appear to collate around the area near the generalized inflection point. Thus, the first mode appears to be driven by dynamics around the "off the wall" generalized inflection point and critical layer.

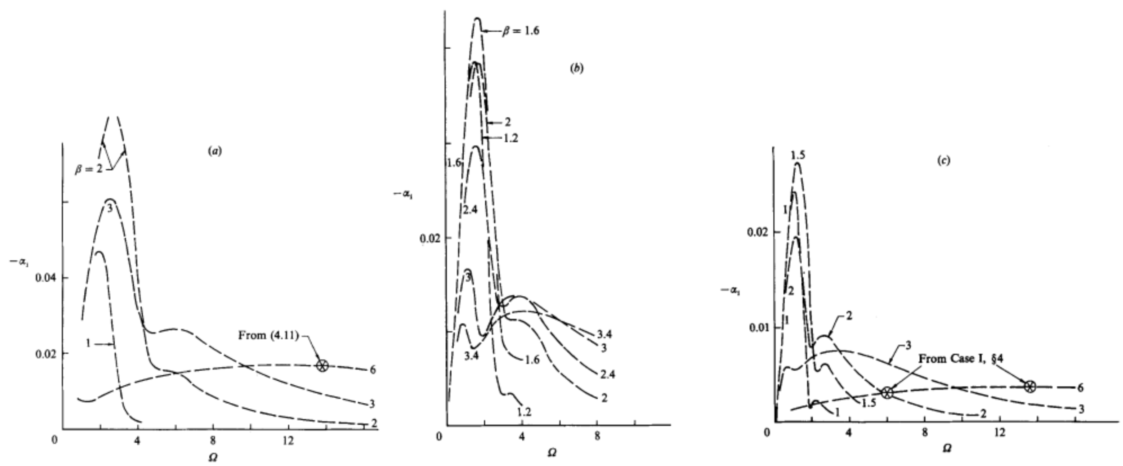

Figure 1.8: (Left-to-right): Spatial growth rates (α_i) with varying spanwise wavenumbers β vs frequency (Ω) for $M_\infty = 2, 3, 4$ (from Smith [10] fig. 2). Its obliqueness angle can be described as $\psi = tan^{-1}(\beta/\alpha)$

The first mode instability is most unstable when propagating at an angle relative to the freestream flow direction. Thus it tends to be referred to as an oblique type instability. It's obliqueness can be partially described with its coupling with vortical components arising near the generalized inflection point in the boundary layer [1]. The first mode also tends to be stabilized with wall cooling and destabilized with wall heating.

1.4.3 2nd Mack Mode

First identified by Mack [9], these modes tend to be dominant when the boundary layer edge velocity becomes large enough such that disturbances travel supersonic relative to the wall but subsonic to the boundary layer [28]. This forms a sharp density gradient within the boundary layer which acts as a "acoustic waveguide" for the these disturbances.

Thus, 2nd mode instabilities are described to be resonating thermoacoustic waves trapped in an thermoacoustic impedance well dictated by a strong density gradient within the boundary layer [35]. Also, an energy source which triggers second-mode growth is identified as the thermoacoustic Reynolds stress. That is, while first mode instability is driven primarily by traditional velocity based Reynolds stress, the second-mode is driven (at least partially) by the thermoacoustic Reynolds stress in conjunction with a well defined acoustic impedance well. The second mode is also highly sensitive to wall temperature variations such that an increase in wall temperature stabilizes the instability, while an decrease in wall temperature destabilizes it [45, 9, 28]. This behavior is the inverse that of the 1st mode. Second modes are commonly found at Mach 6 flow conditions and above.

1.4.4 Crossflow Mode

In 3D boundary layers as seen on rotating bodies, swept wings or bodies at an angle of attack, a type of instability that has been shown to be dominant are crossflow modes. In these types of instabilities, curved 3D streamlines form due to the influences of the sweep on the edge of the boundary layer. Within the boundary layer, the pressure gradient is no longer in balance with the centripetal acceleration and which induces a velocity gradient perpendicular to the streamline. Thus, a secondary flow emerges within the boundary layer (crossflow) which must vanish at the wall and at the boundary layer edge, hence the existence of an inflection point in the crossflow [11].

Depending on the freestream noise levels (boundary layer receptivity), crossflow instabilities tends to present itself either as stationary or traveling waves, with

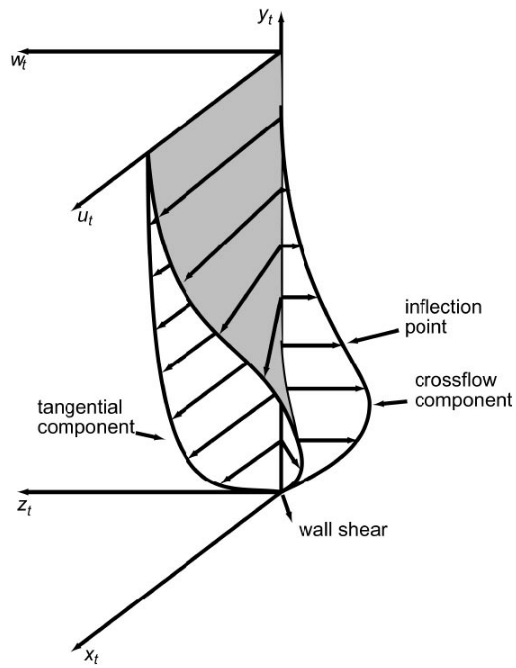

Figure 1.9: Crossflow profile [11]

transition dominated by one or the other, not both. Traveling crossflow instabilities tend to be dominant in noisy freestream flow environments while stationary crossflow instabilities tend to present itself in quiet conditions. It is noted that stationary crossflow instabilities are generally weak but exhibit nonlinear effects leading to secondary instabilities [11].

The trajectory of crossflow vorticies within the boundary layer are strongly correlated to the inflection point of the perpendicular velocity component to the streamline. Hence, vortex trajectories can subsequently be calculated and the crossflow paths can be traced along the geometry [46]. Crossflow instabilities are commonly found when the vehicle body experiences an angle of attack or when the flow is no longer axisymmetric.

1.4.5 Görtler Mode

Similar to crossflow modes, Görtler instabilities arise from vortex type disturbance modes within the boundary layer. However, Görtler modes are induced by geometric variations over the body (convex/concave surfaces) which then presents a weakly non-parallel flow [12]. This instability induces the formation of Görtler vorticies which are counter-rotating vorticies propagating parallel to the direction of flow. These instabilities are considered to be centrifugal type instabilities. Görtler modes have been found on flared cones. [47, 15]

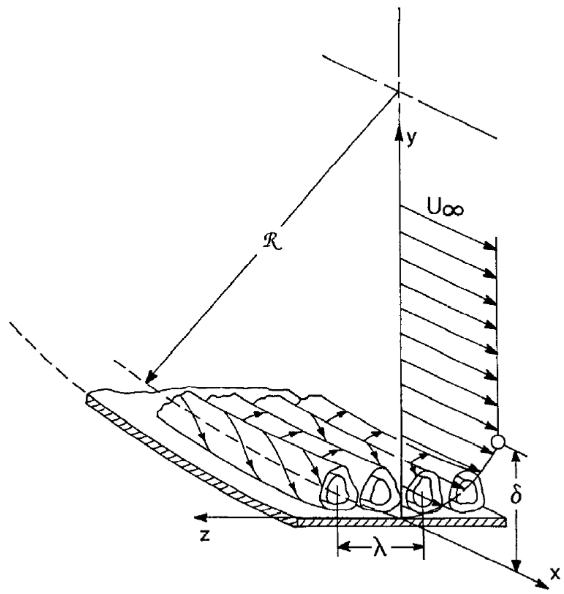

Figure 1.10: Görtler vorticies on a concave geometry [12]

Chapter 2

METHODOLOGY

2.1 Grid Generation

To effectively generate a continuous geometry for basic state calculations, a MATLAB script was developed to parametrically generate discrete coordinates of simple cone profiles for the meshing process. These discrete points of the geometry profile can then be imported into a CAD software such as Solidworks and splined through to generate the basis for the mesh.

Pointwise mesh generation was primarily used to generate the computational domain. A clustering scheme implemented to allow for higher computational fidelity towards anticipated areas where complex flow conditions are expected to occur, such as regions of shocks expansions, compressions, recirculation areas, etc. Special considerations such as fine wall clustering for better resolving of the computational region near the boundary layer, was allocated to the extrusion parameters when generating the computational grid, as this can have a large effect on the convergence of the solution. In order to ensure that the grid is large enough to capture the entire shock region, the shock height can be estimated utilizing $\theta - \beta - Mach$ diagrams along with the known length of the cone. The resulting 2D grid contains structured quadrilateral cells and an extrusion height towards the rear of the cone of approximately 1.3x that of the estimated shock height. This 2D grid is then rotationally extruded 1 degree around the central-axis of the cone to resolve a "slice", which is sufficient as we are considering cones at 0 angle-of-attack (AoA). To study 3D effects, such as crossflows or yawed flight profiles, a half or full body mesh is generated instead to resolve non-symmetric flow phenomena.

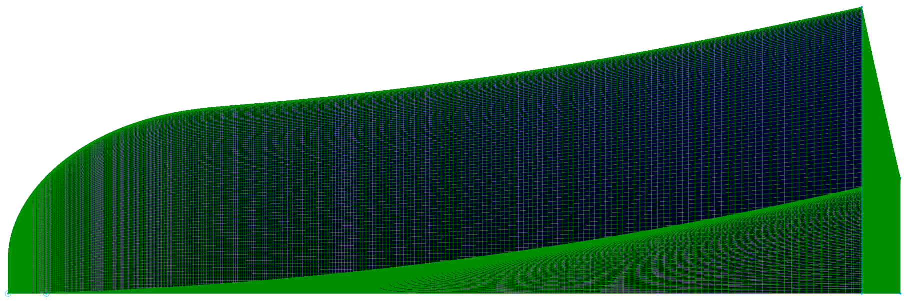

Figure 2.1: A XY plane view of the computational mesh of a flared cone in Pointwise

2.2 Basic States

The steady and laminar basic state solutions are calculated utilizing the US3D computational fluid dynamics software package developed by The University of Minnesota and NASA Ames Research Center and maintained by VirtusAero [37, 48, 49]. The US3D software package is influenced by work on the well-established NASA DPLR (Data Parallel Line Relaxation) CFD code for high-speed compressible flow calculations in chemical/thermal nonequilibrium. US3D is thus an implicit data parallel iterative line-relaxation finite volume solver which allows for the discretization of nonlinear PDEs utilizing finite volume methodologies (FVM) which divides the computational domain into finite control volumes with control surfaces, with fluxes across these surfaces being calculated as it enters and exits volumes.

US3D noted for its ability to integrate high order solving schemes, various viscosity and gas parameters, efficiency on unstructured grids and API integration [37]. A wide range of chemistry models also allows it to model complex reaction effects in high enthalpy flows which makes it highly desirable for hypersonic research[37]. For studies into modal growth of disturbances, a laminar steady state solution is generated (basic state) simulating low noise high-speed flow environments.

2.3 Stability

The JoKHeR (**Jo**seph **K**uehl **He**len **R**eed) stability package is utilized for performing a stability analysis and employ methods utilizing Linear Stability Theory

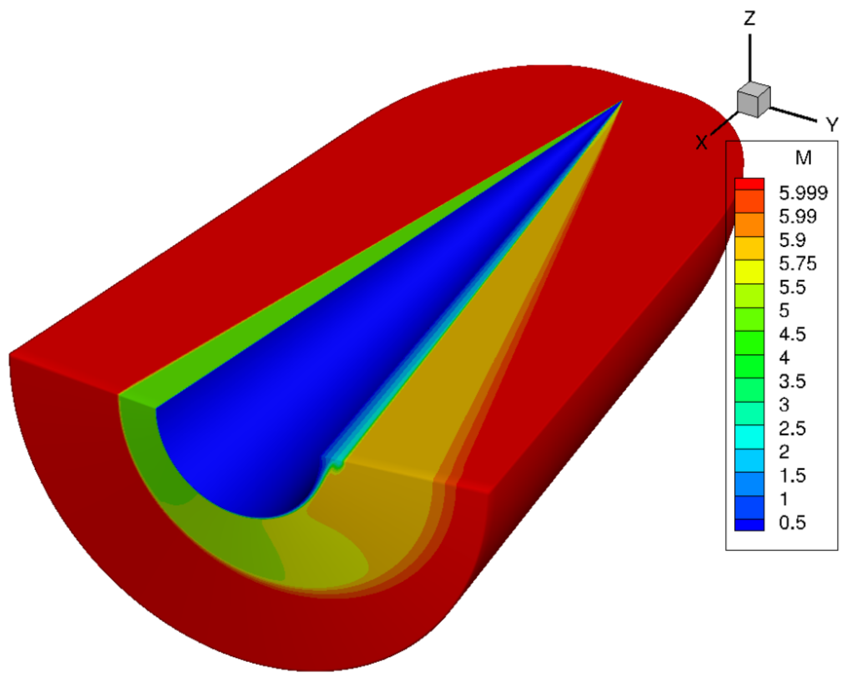

Figure 2.2: US3D results of a flared cone at a 6° angle of attack in M6 flow

(LST) and Linear and Non-linear Parabolized Stability Equations (PSE). The JoKHeR research code was developed at Texas A&M University as part of the National Center for Hypersonic Laminar-Turbulent Transition Research [50]. The code employs a 2D (Quasi-3D), compressible, ideal gas, primitive variable formulation which is capable of marching disturbances along a predefined path with the assumption of uniformity in the perpendicular direction.

2.3.1 Governing Equations

The 3D compressible Navier-Stokes equations assuming ideal gas and Stokes fluid ($\lambda = -\frac{2\mu}{3}$) are as follows:

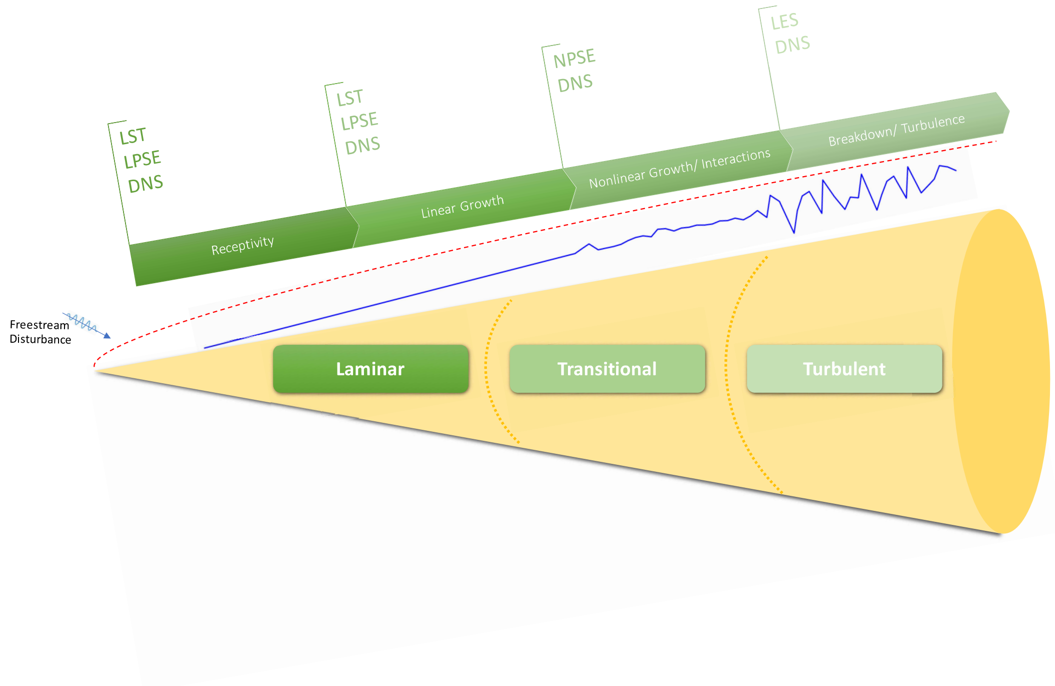

Figure 2.3: Some relevant stability analysis schemes throughout the transition process

$$
\begin{gathered}
\frac{\partial \rho}{\partial t} + \frac{\partial}{\partial x_i}(\rho u_i) = 0 \\
\rho\left(\frac{\partial u_i}{\partial t} + u_j \frac{\partial u_i}{\partial x_j}\right) = -\frac{\partial P}{\partial x_i} + \frac{\partial}{\partial x_j}\left(2\mu\left(\frac{\partial u_i}{\partial x_j} + \frac{\partial u_j}{\partial x_i}\right) + \lambda \frac{\partial u_k}{\partial x_k}\delta_{ij}\right) \\
\rho c_v\left(\frac{\partial T}{\partial t} + u_i \frac{\partial T}{\partial x_i}\right) = \dot{Q} + \frac{\partial}{\partial x_i}\left(k\frac{\partial T}{\partial x_i}\right) - P\left(\frac{\partial u_i}{\partial x_i}\right) + \frac{\mu}{2}\left(\frac{\partial u_i}{\partial x_j} + \frac{\partial u_j}{\partial x_i}\right)^2 + \lambda\left(\frac{\partial u_k}{\partial x_k}\delta_{ij}\right)^2
\end{gathered}
\tag{2.1}
$$

The state variables are non-dimensionalized with respect to the boundary layer edge values $*_e$ due to the highly advective nature of the problem and to simplify the equations to certain key variables.

$$
\begin{array}{llllll}
\hat{u} = \dfrac{u}{U_e} & \hat{v} = \dfrac{v}{U_e} & \hat{w} = \dfrac{w}{U_e} & \hat{x} = \dfrac{x}{L} & \hat{y} = \dfrac{y}{L} & \hat{z} = \dfrac{z}{L} \\
\hat{T} = \dfrac{T}{T_e} & \hat{\rho} = \dfrac{\rho}{\rho_e} & \hat{\mu} = \dfrac{\mu}{\mu_e} & \hat{\kappa} = \dfrac{\kappa}{\kappa_e} & \hat{c_p} = \dfrac{c_p}{c_{p_e}} & \hat{c_v} = \dfrac{c_v}{c_{v_e}} \\
\hat{t} = t\dfrac{U_e}{L} & \hat{p} = \dfrac{p}{\rho_e U_e^2} & & & &
\end{array}
$$

This results in the following parameters:

$$\Pr = \frac{\mu c_p}{\kappa} \qquad R = c_p - c_v \qquad \gamma = \frac{c_p}{c_v} \qquad M^2 = \frac{U^2}{\gamma R T_e} \qquad \delta = \sqrt{\frac{\nu x}{U_e}}$$

$$Re = \frac{U_e \delta}{\nu_e} \qquad = \sqrt{\frac{U_e x}{\nu_e}} = \sqrt{Re_l}$$

An advective time scaling is chosen with all velocities scaled by U_e, length scaled by L and pressure by $\rho_e U_e^2$. Substituting these parameters into equations 2.1, yields the final form:

$$\begin{aligned}
\frac{D\rho}{Dt} + \rho \frac{\partial u_i}{\partial x_i} = 0 \\
\rho \left(\frac{\partial u_i}{\partial t} + u_j \frac{\partial u_i}{\partial x_j} \right) = -\frac{\partial P}{\partial x_i} + \frac{1}{Re} \frac{\partial}{\partial x_j} \left(\mu \left(\frac{\partial u_i}{\partial x_j} + \frac{\partial u_j}{\partial x_i} \right) + \lambda \frac{\partial u_k}{\partial x_k} \delta_{ij} \right) \\
\rho c_v \left(\frac{\partial T}{\partial t} + u_i \frac{\partial T}{\partial x_i} \right) = \dot{Q} + \frac{1}{Re \Pr} \frac{\partial}{\partial x_i} \left(k \frac{\partial T}{\partial x_i} \right) + (\gamma - 1) M^2 \left(\frac{\partial P}{\partial t} + u_i \frac{\partial P}{\partial x_i} \right) \\
+ \frac{\gamma - 1}{Re} M^2 \left[\mu \left(\frac{\partial u_i}{\partial x_j} + \frac{\partial u_j}{\partial x_i} \right)^2 + \lambda \left(\frac{\partial u_k}{\partial x_k} \delta_{ij} \right)^2 \right]
\end{aligned} \tag{2.2}$$

2.4 Linear Stability Theory (LST)

The following assumptions must be considered for Linear Stability Theory (LST)

1. Basic state wall normal flow is zero ($\bar{v} = 0$), and other basic state variables are only functions of y, $\bar{u}(y), \bar{v}(y), \bar{w}(y), \bar{T}(y), \bar{\rho}(y)$. This is the "locally parallel flow" assumption.

2. The disturbance magnitudes are small enough such that non-linear interactions can be neglected ($\phi' \ll \bar{\phi}$).

3. Disturbances are bounded in the normal direction within the boundary layer ($\phi'_{y=0} = \phi'_{y=\delta_{bl}} = 0$)

4. Disturbances are assumed to have the form of a wave propagating in the unbounded directions (homogeneous domains z, t)

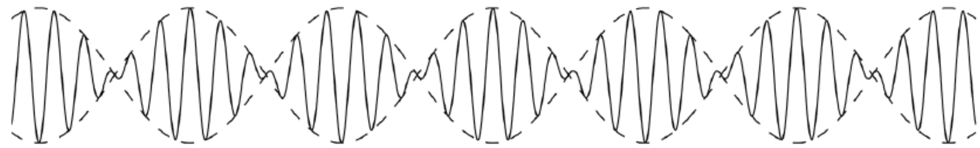

Figure 2.4: Traveling packet of waves where the phase velocity is the rate at which a wave period travels (i.e. the propagation rate of the crests in the figure). The wave group velocity is the velocity of the entire wavepacket. From Juniper et al. [13]

2.4.1 Modal expansions

Modal stability methods study the evolution of infinitesimally small disturbance within the flow and involves decomposing the flow into its mean $\bar{\phi}$ and disturbance ϕ' components.

$$\phi = \bar{\phi}(x, y) + \phi'(x, y, z, t) \tag{2.3}$$

The mean component is commonly referred to a the "basic state" and refers to the base laminar flow on which stability analysis is performed. These basic state solution are obtained via CFD solvers such as US3D.

It is noted that for LST, the governing equations are linear and, along with its boundary conditions, are independent of x, z and t. That is, the equations are functions of y only, and the two planes perpendicular to y, are doubly infinite. Thus these equations can be analyzed in terms of normal modes by the assumption of the disturbance as a monochromatic wave [43], or via methods involving Fourier and Laplace transform pairs [43, 51, 52, 53].

2.4.1.1 Fourier-Laplace Transform Pair

The disturbance can be written explicitly via treatment by Fourier-Laplace transform pairs. In this approach, an initial value problem (IVP) is considered for the system. For example, if spatial stability is considered (as in JoKHeR), an initial value problem arises in that domain (i.e. analysis is concerned with evolution of growth of an instability initiated within the boundary layer). A Laplace transform of the state variables is taken in the spatial coordinates of interest for this IVP, x. The problem can then be Fourier transformed in the z and t as the problem is unbounded in those domains. The resulting expression is considered a complete representation of the infinite summation of all possible solutions in the z and t domains [43, 8, 52, 54].

$$\begin{gathered}\phi'(\alpha,y,z,t) = L[\phi'(x,y,z,t)] = \phi'_L = \int_0^\infty \phi'(x,y,z,t)e^{-i(\alpha x)}\,dx \\ \phi'(\alpha,y,\beta,\omega) = F_{z,t}[\phi'_L] = \int_{-\infty}^\infty \int_{-\infty}^\infty \phi'_L e^{-i(\beta z+\omega t)}\,dzdt\end{gathered} \tag{2.4}$$

Where from the definition of the Laplace transform, α is the complex domain parameter. The expression can then be substituted into equation 2.6 and subsequently into equations 2.2, which the stability characteristics can then be analyzed in the transform domains. The following conditions must be met for this method to be equivalent to the normal mode solution [43]:

$$\lim_{z,t\to\pm\infty} \phi'(x,y,z,t) = 0 \qquad \lim_{z,t\to\pm\infty} \frac{\partial\phi'}{\partial x} = 0 \qquad F_{z,t}[\phi'(\alpha,y,\beta,0)] = 0 \tag{2.5}$$

2.4.1.2 Normal Modes

With the assumption of parallel flow and that the problem is linear, a solution can be also be sought via methods by separation of variables using normal modes. This can be derived by seeking a solution in the form of $\phi'(x,y,z,t) = X(x)Y(y)Z(z)T(t)$. The resulting 3D normal mode disturbance is expressed as a monochromatic wave (i.e. wave of single wavelength) in the form of:

$$\phi' + \phi'^* = \underbrace{\hat{\phi}(y)}_{\text{Shape}}\underbrace{e^{i(\alpha x+\beta z-\omega t)}}_{\text{Phase}} + \underbrace{\hat{\phi}(y)^* e^{-i(\alpha x+\beta z-\omega t)}}_{\text{complex conjugate (c.c.)}} \tag{2.6}$$

The disturbance amplitude $\hat{\phi}$ is a function of y and the phase component is a function of x, z and t. Thus it is implied that the disturbance ϕ is a function of α, β, ω and y, which are components of the stream wise, spanwise wavenumbers, frequency and wall normal direction receptively. Since the perturbations must be real, it is denoted along with its complex conjugate. This treatment results in an expression that is equivalent to methods involving Fourier-Laplace transforms.

Since the "locally parallel flow" assumption applies here, one of the limitations of this analysis is that it is only performed at a specific specified location and does not track any evolution downstream. The wall-normal velocity component and the streamwise derivatives of the mean flow are assumed to be negligible.

LST can be presented as a temporal or spatial stability problem. For a spatial stability problem, an initial value problem is considered in the spatial directions, and a solution is sought via a Laplace transform in the spatial domain of interest. For 2D LST for spatial stability as seen in JoKHeR, α is then complex ($\alpha = \alpha_r + i\alpha_i$) where α_r refers to the physical wavelength while α_i refers to the disturbance growth rate (i.e. growth rate in the x direction). However, for temporal stability, the initial value problem is instead considered in the t domain, which will yield a complex frequency ω such that ($\omega = \omega_r + i\omega_i$), with the real and imaginary components defining the frequency and temporal growth rate respectively. Similarly, for stability in the spanwise direction, β is the complex spanwise wave number where β_r is the physical spanwise wavelength and β_i being the growth rate in the z direction.

The disturbance wavenumber $\vec{k}$ with magnitude k is defined as

$$k = \sqrt{\alpha_r^2 + \beta_r^2} \tag{2.7}$$

and thus the angle of wave propagation ψ relative to the x axis is

$$\psi = tan^{-1}\left(\frac{\beta_r}{\alpha_r}\right) \tag{2.8}$$

2.4.2 Implementation

In the interest of brevity, only the 2D incompressible continuity and momentum equations are considered for this example to illustrate the general process of deriving the LST matrices for implementation in JoKHeR. Substituting in the disturbance equations 2.6 into equation 2.2 while assuming 2D parallel flow ($\bar{u}(y), \bar{w}(y), \bar{p}(y), \bar{v} = 0$) and expanded yields:

$$\frac{\partial u'}{\partial x} + \frac{\partial v'}{\partial x} + \frac{\partial w'}{\partial x} = 0 \tag{2.9}$$

$$\frac{\partial u'}{\partial t} + \bar{u}\frac{\partial u'}{\partial x} + v'\frac{\partial \bar{u}}{\partial y} + \bar{w}\frac{\partial u'}{\partial z} = -\frac{\partial p'}{\partial x} + \frac{1}{Re}\nabla^2 u' \tag{2.10}$$

$$\frac{\partial v'}{\partial t} + \bar{u}\frac{\partial v'}{\partial x} + \bar{w}\frac{\partial v'}{\partial z} = -\frac{\partial p'}{\partial y} + \frac{1}{Re}\nabla^2 v' \tag{2.11}$$

$$\frac{\partial w'}{\partial t} + \bar{u}\frac{\partial w'}{\partial x} + v'\frac{\partial \bar{w}}{\partial y} + \bar{w}\frac{\partial w'}{\partial z} = -\frac{\partial p'}{\partial z} + \frac{1}{Re}\nabla^2 w' \tag{2.12}$$

Substituting the disturbance equation 2.6 into eqs. (2.9) to (2.12) yields:

$$i\alpha\hat{u} + D\hat{v} + i\beta\hat{w} = 0 \tag{2.13}$$

$$\left(-i\omega + i\alpha\bar{u} + i\beta\bar{w} + \frac{\alpha^2}{Re} + \frac{\beta^2}{Re} - \frac{1}{Re}D^2\right)\hat{u} + \frac{\bar{u}}{\partial y}\hat{v} + i\alpha\hat{p} = 0 \tag{2.14}$$

$$\left(-i\omega + i\alpha\bar{u} + i\beta\bar{w} + \frac{\alpha^2}{Re} + \frac{\beta^2}{Re} - \frac{1}{Re}D^2\right)\hat{v} + D\hat{p} = 0 \tag{2.15}$$

$$\left(-i\omega + i\alpha\bar{u} + i\beta\bar{w} + \frac{\alpha^2}{Re} + \frac{\beta^2}{Re} - \frac{1}{Re}D^2\right)\hat{w} + \frac{\bar{w}}{\partial y}\hat{v} + i\beta\hat{p} = 0 \tag{2.16}$$

Expressed in matrix form is:

$$(L_0 + \alpha L_1 + \alpha^2 L_2)\phi = 0 \tag{2.17}$$

where:

$$L_0 = \begin{bmatrix} 0 & D & 0 & 0 & \\ -i\omega+i\beta\bar{w}+\frac{\beta^2}{Re}-\frac{1}{Re}D^2 & \frac{\partial\bar{u}}{\partial y} & 0 & 0 & \\ 0 & -i\omega+i\beta\bar{w}+\frac{\beta^2}{Re}-\frac{1}{Re}D^2 & \frac{\partial\bar{u}}{\partial y} & 0 & D \\ 0 & \frac{\partial\bar{w}}{\partial y} & -i\omega+i\beta\bar{w}+\frac{\beta^2}{Re}-\frac{1}{Re}D^2 & \frac{\partial\bar{u}}{\partial y} & i\beta \end{bmatrix}$$

$$L_1 = \begin{bmatrix} i & 0 & 0 & 0 \\ i\bar{u} & 0 & 0 & i \\ 0 & i\bar{u} & 0 & 0 \\ 0 & 0 & i\bar{u} & 0 \end{bmatrix} L_2 = \begin{bmatrix} 0 & 0 & 0 & 0 \\ \frac{1}{Re} & 0 & 0 & 0 \\ 0 & \frac{1}{Re} & 0 & 0 \\ 0 & 0 & \frac{1}{Re} & 0 \end{bmatrix} \phi = \begin{bmatrix} \hat{u} \\ \hat{v} \\ \hat{w} \\ \hat{p} \end{bmatrix}$$

To obtain a form of that can be solved via a generalized eigenvalue solver (i.e. MATLAB, Python NumPy, etc.), the nonlinear dependence is eliminated. This can be done by introducing the following three additional variables $\alpha\hat{u}, \alpha\hat{v}, \alpha\hat{w}$. This reduces 2.17 results to:

$$(M_0 + \alpha M_1)\psi = 0 \tag{2.18}$$

$$M_0 = \begin{bmatrix} 0 & D & 0 & 0 & 0 & 0 & 0 \\ -i\omega + i\beta\bar{w} + \frac{\beta^2}{Re} - \frac{1}{Re}D^2 & \frac{\partial \bar{u}}{\partial y} & \frac{\partial \bar{u}}{\partial y} & 0 & 0 & 0 & 0 \\ 0 & -i\omega + i\beta\bar{w} + \frac{\beta^2}{Re} - \frac{1}{Re}D^2 & \frac{\partial \bar{u}}{\partial y} & 0 & D & 0 & 0 \\ 0 & \frac{\partial \bar{w}}{\partial y} & -i\omega + i\beta\bar{w} + \frac{\beta^2}{Re} - \frac{1}{Re}D^2 & \frac{\partial \bar{u}}{\partial y} & i\beta & 0 & 0 \\ 0 & 0 & 0 & 0 & -1 & 0 & 0 \\ 0 & 0 & 0 & 0 & 0 & -1 & 0 \\ 0 & 0 & 0 & 0 & 0 & 0 & -1 \end{bmatrix}$$

$$M_1 = \begin{bmatrix} i & 0 & 0 & 0 & 0 & 0 & 0 \\ i\bar{u} & 0 & 0 & i & \frac{1}{Re} & 0 & 0 \\ 0 & i\bar{u} & 0 & 0 & 0 & \frac{1}{Re} & 0 \\ 0 & 0 & i\bar{u} & 0 & 0 & 0 & \frac{1}{Re} \\ 1 & 0 & 0 & 0 & 0 & 0 & 0 \\ 0 & 1 & 0 & 0 & 0 & 0 & 0 \\ 0 & 0 & 1 & 0 & 0 & 0 & 0 \end{bmatrix} \psi = \begin{bmatrix} \hat{u} \\ \hat{v} \\ \hat{w} \\ \hat{p} \\ \alpha\hat{u} \\ \alpha\hat{v} \\ \alpha\hat{w} \end{bmatrix}$$

The derivatives are then replaced by finite difference schemes as outlined in appendix A with boundary conditions:

$$\hat{u}(0) = \hat{v}(0) = 0$$
$$D\hat{p}(0) = \frac{1}{Re}D^2\hat{v}(0)$$
$$\hat{u}(\infty) = \hat{v}(\infty) = \hat{p}(\infty) = 0$$

Note the pressure boundary condition at the wall is to account for the fluctuating wall pressure. This can be modified to account for other user specified wall boundary conditions such as the impedance boundary condition (see chapter 6). The resulting system can then be solved in MATLAB via the its built in generalized eigenvalue solver utilizing a QZ algorithm. For full 3D compressible LST, the same steps are applied with the 3D compressible NS equations and boundary conditions:

$$\hat{u}(0) = \hat{v}(0) = \hat{w}(0) = \hat{T}(0) = 0$$

$$D\hat{p}(0) = \frac{1}{Re} D^2 \hat{v}(0)$$

$$\hat{u}(\infty) = \hat{v}(\infty) = \hat{p}(\infty) = \hat{T}(\infty) = \hat{p}(\infty) = 0$$

2.5 Linear PSE (LPSE)

PSE or Parabolized Stability Equations are also widely utilized for stability analysis. Originally identified by Herbert and Bertolotti [26], during a critical review of Gaster [55] early nonparallel work, the parabolized stability equations have been developed as an efficient and powerful tool for studying the stability of advection-dominated laminar flows. Excellent introductions to the PSE method and summary of its early development were provided by Herbert [56]. During the early stages of both linear and nonlinear development of this technique, much was established related to basic marching procedures, curvature, normalization conditions, and numerical stability of the method itself (Bertolotti [22]; Chang et al.[57], Joslin et al.[58], Li and Malik [59], and Haynes and Reed [60])

In a relatively short time, the field rapidly expanded to include complex geometries, compressible flow, and finite-rate thermodynamics (Stuckert and Reed [61], Chang et al.[62], Johnson et al.[63], Haynes and Reed [60], Malik [64], Chang [65], Johnson and Candler [66], Li et al.[67], Theofilis [68], Paredes et al.[69], Kuehl et al.[14], Kocian et al.[70], and Perez et al.[71])

Only linear interactions are considered for this section, which assumes that there are no coupling between modes, similar to LST. As such, the type of equations used in this analysis are dubbed Linear Parabolized Stability Equations (LPSE). One difference from LST is that LPSE eliminates the requirement for the "locally parallel flow" assumption. That is, while LST is able to determine local stability effects at a specific spatial (local) location, it does not yield any information on the historical effects of perturbations. On the other hand, LPSE can reveal stability effects from local and upstream flow conditions. As such, LST and LPSE are sometimes referred to as local and non-local stability methods respectively.

An important criterion for the success of LPSE is done by developing methods of analyzing the flow without solving PDEs of an elliptic nature. This is primarily done by considering the method of multiple scales (MMS), which takes advantage of the fact that the wall normal basic state quantities vary more rapidly than compared to the same basic state quantities in the streamwise direction, as commonly seen in flows within boundary layers. By applying this method of multiple scales, it is then possible to derive a parabolic system of PDEs which can be solved via a marching solution that can reflect upstream influences.[13]

The crux of MMS lies in the assumption that variations in the streamwise direction are much smaller than in the wall normal direction. Thus. slow and fast scales are introduced and related through the variable $\tilde{x} = \frac{x}{Re}$. This $\tilde{x}$ evolves slowly along the x direction (x over a large number Re). Ultimately, disturbances are assumed to be a monochromatic wave in the form of an fast varying amplitude shape component and a slow varying wave component. Recasting equation 2.6 here for a 2D disturbance,

$$\phi(x, y, t) = \underbrace{\bar{\phi}(x, y)}_{\text{basic state}} + \underbrace{\phi'(x, y, t)}_{\text{disturbance}} \tag{2.19}$$

The disturbance wave can be assumed to be represented as a sum of a discrete number of periodic functions with Fourier coefficients. Applying a Fourier transform F to the disturbance term now assumes the disturbance in the form of the shape and wave components:

$$F[\phi'] = \underbrace{\hat{\phi}(\tilde{x}, y)}_{\text{shape}} \underbrace{\Phi(x, t)}_{\text{wave}} + c.c.$$

where the wave part satisfies

$$\frac{\partial \Phi}{\partial x} = i\alpha(\tilde{x})\Phi \tag{2.20}$$

$$\frac{\partial \Phi}{\partial t} = -i\omega\Phi, \tag{2.21}$$

and where $Re = \frac{U_e \delta_r}{\nu_e}$ is the Reynolds number based on characteristic values of edge velocity (U_e), edge kinematic viscosity (ν_e), and the length scale of the reference boundary layer (δ_r). Now applying an inverse Fourier transform to F^{-1} results in the form of the disturbance which is considered for PSE:

$$F[\phi'(\tilde{x}, y, t)] = \phi'(\tilde{x}, y, \omega) = \int_{-\infty}^{\infty} \underbrace{\hat{\phi}(\tilde{x}, y, \omega)}_{\text{shape}} \underbrace{A(\tilde{x}, \omega)e^{-i\omega t}}_{\text{wave}} d\omega \tag{2.22}$$

where $A(\tilde{x}, \omega) = e^{i\int \alpha(\tilde{x},\omega)dx}$ and the dependence of the shape function ($\hat{\phi}$) and amplitude function (A) on ω has been made explicit. The shape and amplitude functions are essentially the Fourier transform of the disturbance. Upon expansion of the streamwise derivatives

$$\frac{\partial \phi'}{\partial x} = \int_{-\infty}^{\infty} \left(\frac{1}{Re}\frac{\partial \hat{\phi}}{\partial \tilde{x}} + i\alpha\hat{\phi} \right) Ae^{-i\omega t} d\omega$$

$$\frac{\partial^2 \phi'}{\partial x^2} = \int_{-\infty}^{\infty} \left(\frac{1}{Re^2}\frac{\partial^2 \hat{\phi}}{\partial \tilde{x}^2} + \frac{2i\alpha}{Re}\frac{\partial \hat{\phi}}{\partial \tilde{x}} + \frac{i\hat{\phi}}{Re}\frac{\partial \alpha}{\partial \tilde{x}} - \alpha^2\hat{\phi} \right) Ae^{-i\omega t} d\omega,$$

it is found that the second spatial derivative $\frac{\partial^2 \hat{\phi}}{\partial \tilde{x}^2}$ is of the highest order. By an order of magnitude analysis, it can be seen that the $\frac{\partial^2 \hat{\phi}}{\partial x^2}$ has terms that are scaled by $\frac{1}{Re^2}$ and some components of the NS components are then scaled by $\frac{1}{Re}$ coming from the viscous terms, which reveals that all $O\left(\frac{1}{Re^2}\right)$ streamwise x terms can be neglected. This leaves the disturbance equation nearly parabolized as the elliptic terms associated with the higher order derivatives are also eliminated (Li and Malik 1996 [59]), and an efficient marching solution may be sought. Results from an LPSE analysis can be processed into N-factors otherwise known as the e^N correlation method. N-factors can be computed by

$$N = ln\left(\frac{A}{A_0}\right) \approx -\int_{x_0}^{x} \alpha_i dx \tag{2.23}$$

Where A and A_0 is the disturbance amplitude at a local streamwise location and at the N_1 neutral point respectively. N factors can also be approximated by integrating the unstable growth rate obtained from LST results.

2.6 Normalization condition

To efficiently iterate for a solution, a normalization condition is introduced to provide closure for this system. Due to the assumption of a slowly growing boundary layer and the introduction of slow variables, the shape function is in turn also assumed to be slow varying in the streamwise direction. The introduced normalization condition applies restrictions for variations on the shape function and transfers the energy to the wave function.

$$\int\limits_0^\infty \sum_{k=1}^{n} \phi_k^* \frac{\partial \phi_k}{\partial x} dy = 0 \tag{2.24}$$

Where n is the total number of state variables and * denotes complex conjugate. It is noted that when this condition is expanded, the real components restricts growth in disturbance amplitude, while the imaginary components restricts the phase change.

2.7 Non-linear PSE (NPSE)

From chapter 1, it is commonly assumed that the modal growth interpretation follows a general series of steps which eventually leads to transition.

1. Small amplitude disturbances are introduced into the boundary layer via freestream disturbances or boundary imperfections.
2. The initial small amplitude disturbances can grow and is governed by linear stability dynamics.
3. With larger disturbance amplitudes, linear dynamics may no longer hold and non-linear interactions become important and dominant.

4. Non-linear interactions lead to spectral broadening and eventual transition to turbulence.

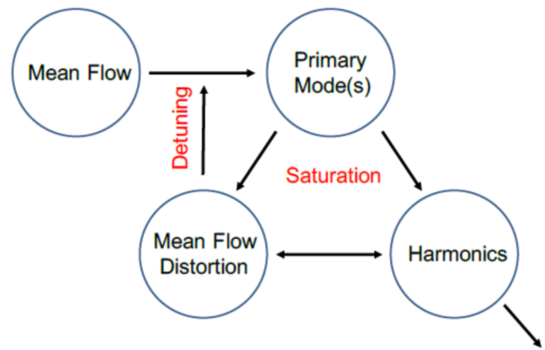

Figure 2.5: Schematic of energy flow between the basic state and disturbance modes. From Kuehl (2017)[14]

As the disturbance amplitude grows in the boundary layer, methods utilizing LST and LPSE are unable to model multi-mode interactions and are thus only able to consider dynamics of individual modes. In Nonlinear Parabolized Stability Equations (NPSE), this limitation can be overcome as all modes can be solved simultaneously and their interactions modeled and coupled through various nonlinear forcing terms.

With NPSE, a finite amplitude disturbance can be employed instead of an infinitesimally small amplitude as was considered with LST and LPSE. Within the boundary layer, the complex energy interactions between various mechanisms can be depicted with figure 2.5. Energy from the mean flow feeds into the primary (Mack) mode interactions. Non-linear interactions, also referred to as ”non-linear saturation”, leads to energy loss from the primary modes to the mean flow distortion and harmonics being comparable by the energy gained by the primary disturbance from the mean flow. This can cause a gradual decrease in the growth rate of the primary disturbance and can lead to the cessation of primary mode growth. The energy from the mean flow distortion can in turn, feedback and detune the primary modes. Schemes involving NPSE are able to model the stability of highly advective laminar flows while incorporating nonlinear, nonparallel effects to be with close agreement with DNS results, at the fraction of the computational demands.

2.7.0.1 Sum-Difference Interactions (Harmonics)

Derivation of the NPSE disturbance equations is similar to that of LPSE, however a discrete treatment is taken here. The total 2D disturbance is assumed to be periodic in time and the spanwise direction, hence a double discrete Fourier transform is taken in the z and t domain.

$$\begin{aligned} \phi' &= \sum_{-N}^{N} \sum_{-K}^{K} \left[\underbrace{\hat{\phi}(\tilde{x}, y)}_{\text{shape}} \underbrace{A(\tilde{x}) e^{-i(k\beta_0 z - n\omega_0 t)}}_{\text{wave}} \right] + c.c. \\ A(\tilde{x})_{(n,k)} &= e^{i \int \alpha(\tilde{x})_{(n,k)} dx} \end{aligned} \tag{2.25}$$

A shape and wave function arises again from this transformation. $A(\tilde{x})$ is the spectral amplitude function with streamwise wave number $\alpha(\bar{x})$. β_0 and ω_0 are the fundamental spanwise wavenumber and frequency respectively.

In the system, the primary mode is also modeled along with its harmonics (non-primary modes), which are integer multiples of the properties of itself. As short hand notation, modes are denoted by (n, k) which identifies the mode having as frequency and spanwise wavenumber respectively n and k times the frequency and spanwise wave number of the primary (fundamental) mode. Each mode is the product of the shape and wave (phase) function and is subject to the normalization condition as defined by equation 2.24.

The following derivatives presents themselves in the problem statement:

$$\frac{\partial \phi'}{\partial t} = \sum_{-N}^{N}\sum_{-K}^{K} -i\omega_0 n\phi'$$

$$\frac{\partial \phi'}{\partial z} = \sum_{-N}^{N}\sum_{-K}^{K} -i\beta_0 k\phi'$$

$$\frac{\partial \phi'}{\partial x} = \sum_{-N}^{N}\sum_{-K}^{K}(\frac{1}{Re_L}\frac{\partial \hat{\phi}}{\partial \tilde{x}} + i\alpha_{(n,k)}\hat{\phi})A_{(n,k)}e^{i(k\beta_0 z - n\omega_0 t)}$$

$$\frac{\partial^2 \phi'}{\partial x^2} = \sum_{-N}^{N}\sum_{-K}^{K}(\underbrace{\frac{1}{Re_L^2}\frac{\partial^2 \hat{\phi}}{\partial \tilde{x}^2}}_{\text{elliptic term}} + \frac{2i\alpha_{(n,k)}}{Re_L}\frac{\partial \hat{\phi}}{\partial \tilde{x}} + \frac{i\hat{\phi}}{Re_L}\frac{\partial \alpha_{(n,k)}}{\partial \hat{x}} - (\alpha_{(n,k)})^2\hat{\phi})A_{(n,k)}e^{i(k\beta_0 z - n\omega_0 t)}$$

The elliptic term in the second x derivative is on the order of $(\frac{1}{Re})^2$,which is much less than the other terms in that equation. Thus, this term can be neglected to again obtain "parabolized" equations of motions which can be effectively marched in a computational scheme. However, since disturbance amplitudes are no longer "infinitesimally" small, nonlinear terms from equations in appendix B must now be considered and reincorporated to properly model the governing dynamics. In addition to being non-negligibly finite, the disturbances must also be real so the solution is also coupled with its complex conjugates:

$$\alpha^*_{(n,k)} = -\alpha_{(-n,-k)} \qquad \beta^*_{0(n,k)} = \beta_{0(-n,-k)} \qquad A^*_{0(n,k)} = -A_{0(-n,-k)}$$
$$\hat{u}^*_{(n,k)} = \hat{u}_{(-n,-k)} \qquad \hat{v}^*_{(n,k)} = \hat{v}_{(-n,-k)} \qquad \hat{w}^*_{(n,k)} = \hat{w}_{(-n,-k)}$$
$$\hat{T}^*_{(n,k)} = \hat{T}_{(-n,-k)} \qquad \hat{\rho}^*_{(n,k)} = \hat{\rho}_{(-n,-k)}$$

A "harmonic balancing" condition is applied where the linear and nonlinear coefficients and higher order terms must match. This forces nonlinear interactions between mode-mode, mode-harmonic, harmonic-harmonic and results in coupling in order to fulfill this balancing criterion. The resulting system of governing equations are now coupled and must be solved for every (n, k) combination.

2.7.0.2 Note on Mean Flow Distortion (MFD)

Intensively expanding these equations with (n, k) combinations, there exists a mode with no frequency nor complex conjugate and is thus non-oscillatory which is denoted as (0,0). Physically, this arises from nonlinear interactions between the disturbances and base flows and appears as an energy buffer and provides feedback onto the primary mode disturbance by affecting the energy flow from the basic state into the primary mode, as shown by Liang et. al. [72].

2.7.0.3 Wavepacket representation

Classically, the modeling of nonlinear interactions within the boundary layer is done by assuming discrete frequency primary modes and its respective harmonics. This formulation fails to consider disturbance bandwidth effects and thus may misrepresent the actual frequency content of the disturbances and unable to model the complex energy flows present in nonlinear dynamics. In experimental studies, the disturbance frequencies spans a finite bandwidth range rather than at a discrete frequency; an example is noted in figure 2.6.

The wavepacket formulation seeks to rectify the discrepancy between experimental results and computational PSE studies by accurately and consistently accounting for redistribution of energy between finite bandwidth disturbances by representing disturbances as a composition of multiple discrete shape functions that each oscillate at a frequency and bandwidth [39]. The total disturbance is then modeled as spectrum of k number of discrete disturbances in a Fourier series:

$$A(x, \omega) = \underbrace{A_k(x; \omega_k)}_{\text{Amplitude}} \underbrace{W_k(\omega; \omega_k)}_{\text{Weighting}}$$

$$\phi' = \sum_k \hat{\phi}_k A e^{-i\omega_k t} = \sum_k \hat{\phi}_k A_k W_k e^{-i\omega_k t}$$

Note that each discrete shape function $\hat{\phi}_k$ oscillates at a frequency and amplitude function A comprising of an amplitude coefficient A_k and a weighting function W_k

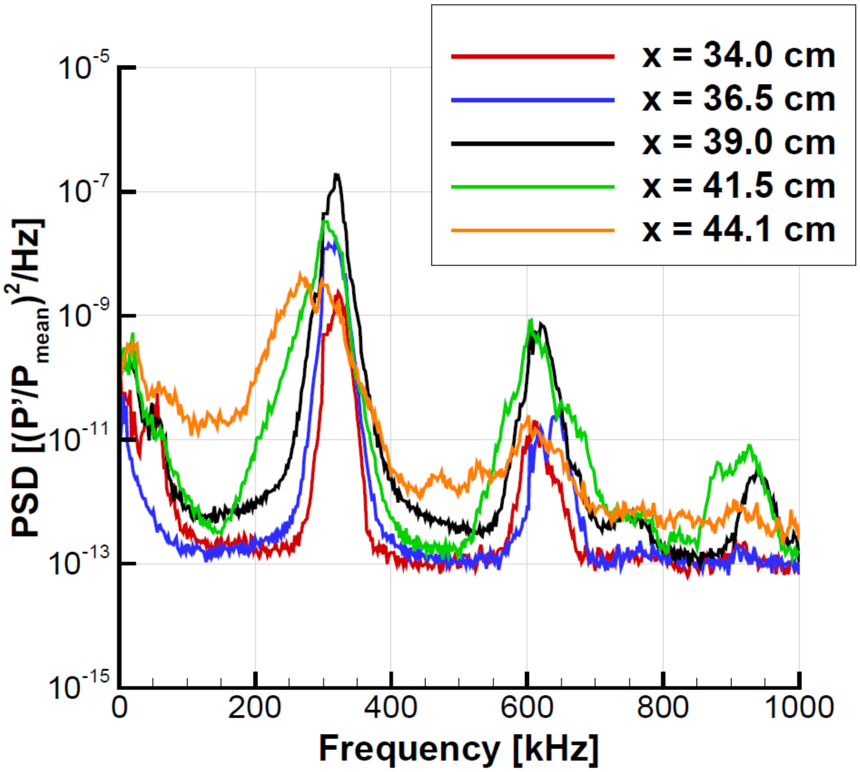

Figure 2.6: Typical streamwise normalized power spectral density (PSD) of a smooth wall cone exhibiting second mode instability waves obtained from experimental studies. Note the primary mode frequency at 25kHz along with its higher frequency harmonics. From Chynoweth et. al. (2019)[15]

which contains spectral information of the frequency bandwidth. Nonlinear interactions themselves can be modeled by applying the convolution property of the Fourier transform where the convolution of 2 functions f & g is such that:

$$(f * g)(s) = \int_{-\infty}^{\infty} f(\omega)g(s-\omega)d\omega$$

Applying this to two sample nonlinear terms is shown intensively by Kuehl[73] to be as follows.

$$F^{-1}[F[\phi_i'\phi_j']] = \hat{\phi}_i\hat{\phi}_j A_i A_j \int_{-\infty}^{\infty} (W_i * W_j)e^{-i\omega t}d\omega \tag{2.26}$$

The disturbance frequency content can be further modeled by considering the form of the weighting function. For the traditional discrete mode representation (Delta function weighting), the following is considered:

$$\begin{aligned} W_0 &= \delta(\omega - \omega_0) \\ (W_i * W_j) &= \delta(\omega - (\omega_i + \omega_j)) \end{aligned} \tag{2.27}$$

Where the subscript $*_0$ refers to linear terms while subscripts $*_i$ and $*_j$ refers to non-linear terms. For modeling as a continuous frequency spectrum, this approach is taken instead:

$$\begin{aligned} W_0 &= \frac{1}{\sqrt{2\pi\sigma_0^2}} e^{-\frac{(\omega-\omega_0)^2}{2\sigma_0^2}} \\ (W_i * W_j) &= \frac{1}{\sqrt{2\pi(\sigma_i - \sigma_j)^2}} e^{-\frac{(\omega-(\omega_i-\omega_j))^2}{2(\sigma_i-\sigma_j)^2}} \end{aligned} \tag{2.28}$$

as shown by Kuehl [73]. The dynamics between nonlinear and linear interactions with the new weighting formulation within the problem statement follows the harmonic balancing criterion such that:

$$\int_{-\infty}^{\infty} \hat{\phi}_0 A_0 W_0 e^{-i\omega t} d\omega \rightleftharpoons \hat{\phi}_i \hat{\phi}_j A_i A_j \int_{-\infty}^{\infty} (W_i * W_j) e^{-i\omega t} d\omega$$

Where again, all the linear and nonlinear coefficients and higher order quadratic terms must match. With the wavepacket formulation, the resulting harmonics has been shown to have a larger frequency bandwidth than the primary mode due to the properties of the convolution. Thus, during the process of nonlinear interactions between the harmonics back with its primary mode, the energy that is then projected, spans a wider range of frequencies. This in turn, leads to the spectral broadening phenomenon and evidence of low-frequency content generation that has been seen experimentally [74, 15].

2.8 Eigenmode search algorithm

Spurious eigenvalues appear when performing an computational numerical analysis on complex stability problems, which is particularly common in the field of hydrodynamic stability. There are many mathematical reasons for the emergence of spurious eigenvalues; one common reason may be due to the poor approximation of boundary values within the problem as is common with discrete derivatives schemes [75, 8]. Spurious eigenvalues are nonphysical and are considered byproducts of the numerical computation process. Efforts in the elimination of spurious eigenvalues were performed to determine the unstable mode of interest.

There has been great efforts by others to filter out these spurious results and to reduce the eigenproblem compute time associated with the full eigenvalue problem by using Chebyshev, Tau or Arnoldi iteration schemes to name a few [75, 76, 77, 78, 79]. The current version of JoKHeR solves the full eigenvalue problem. As it is mentally and physically draining for the user to manually verify each eigensolution, particularly if analyzing a problem with a range of frequency and streamwise location permutations, an automated algorithm was developed in an attempt to eliminate spurious eigensolutions. The primary method utilized is by computationally comparing the the current solution with historical trends of previous valid solutions.

2.8.1 Eigenvalue spectrum analysis

Each blue point as seen in figure 2.7, is a computed eigensolution from the full generalized eigenvalue problem. Note that this is a zoomed in view of the full spectrum plot, which depending on the LST setup parameters, can range up to 1800 values or more. The computed eigensolutions are first pass through a filter where through an iterative k-means clustering scheme to determine the general area where the continuous and discrete spectrums are clustered/centered, which results in a plot centered like figure 2.7.

As eigenvalues associated with 1st and 2nd modes are historically situated near

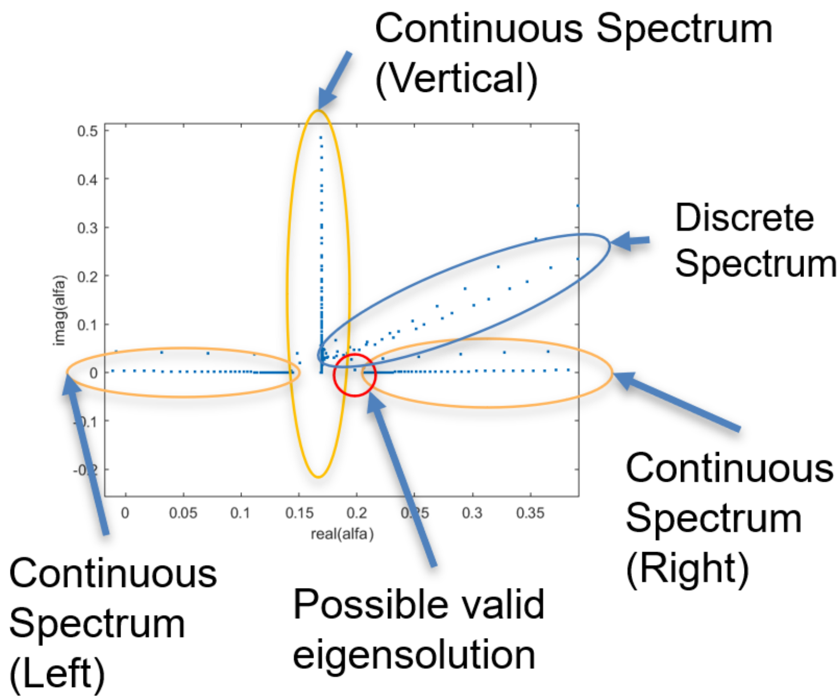

Figure 2.7: Typical eigenvalue spectrum (zoomed in) from a solved full eigenvalue problem in JoKHeR. Note the discrete eigenvalue spectra circled in purple and the continuous spectrum circled in red.

the right discrete spectrum, an simple iterative curve fitting scheme was then implemented in order to detect the span of the continuous spectrum and to remove values left of the fitted curve. The iterative nature of this scheme allows the curve to be more "refined" with each pass as outlier points from the k-means clustering are iteratively removed as depicted in the left of figure 2.8. The resulting eigensolutions after this filtering scheme are shown on the right of said figure.

2.8.2 Shape function analysis

Wit the number of eigensolutions for analysis being substantially decreased after the eigenspectrum analysis, a shape function analysis can be performed. 1st and 2nd modes have a distinct U' profiles which can be compared with existing examples in order to further filter out spurious results. A typical 2nd mode profile is shown in figure 2.10, with a large primary peak near the wall and a smaller trailing secondary

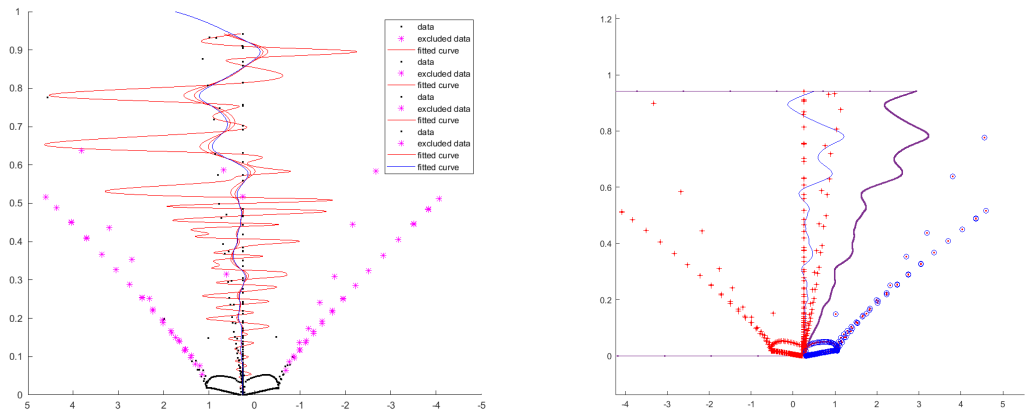

Figure 2.8: Left: Iterative continuous spectrum curve fitting with excluded points at each iteration. The final fitted curve is highlighted blue. Right: Removed eigensolution (red plus) and eigensolutions passed on to shape function analysis (blue circle)

peak which decays to the freestream. If these shape functions are assumed analogous to signals, a simple cross-correlation MATLAB function (xcorr) is then utilized to correlate the current shape function with a repository of user-validated 2nd modes. The cross-correlation between two functions is expressed as:

$$(S_{int} * S_{ref}) = \sum_{m=-\infty}^{\infty} S^{*}_{int}(m-n) S_{ref}(n) \tag{2.29}$$

Where $*$ denotes the convolution between the current signal of interest S_{int} and reference signal S_{ref}. The superscript * denotes the complex conjugate and n the signal displacement(lag) [80, 81]. This cross-correlation between signals is normalized with 0 lag utilizing the *'-coeff'* argument and scales the output coefficient values to the range of -1 to 1, where 1 represents perfect correlation, -1 represents perfect anti-correlation, and 0 represents no correlation. This allows for a comparison of similarity between the each signal of interest and reference signals in the repository regardless of their respective amplitudes.

A statistical analysis is then performed across these correlation coefficients, where the frequency density of coefficients are plotted in a histogram as depicted in figure 2.9. A gaussian distribution is then fitted over the frequency densities and the coefficient of its peak is recorded. Shape functions with coefficient peaks below a user defined threshold and their corresponding eigensolutions are filtered out.

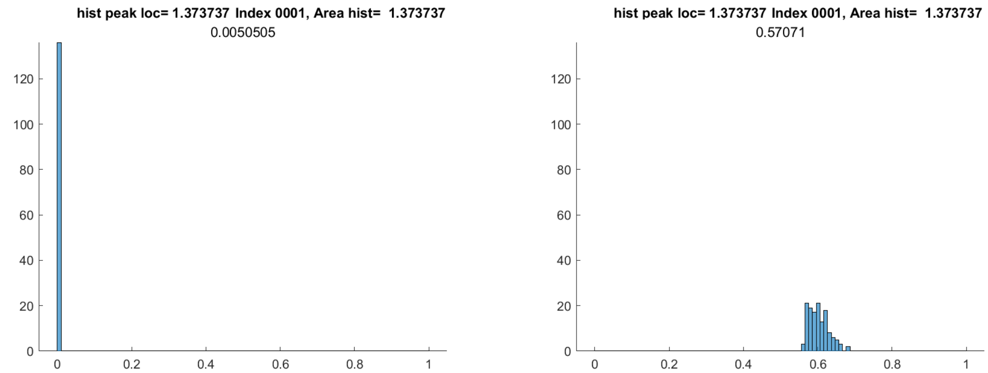

Figure 2.9: Left: A relatively "dissimilar" shape function. Right: A relatively "similar" shape function

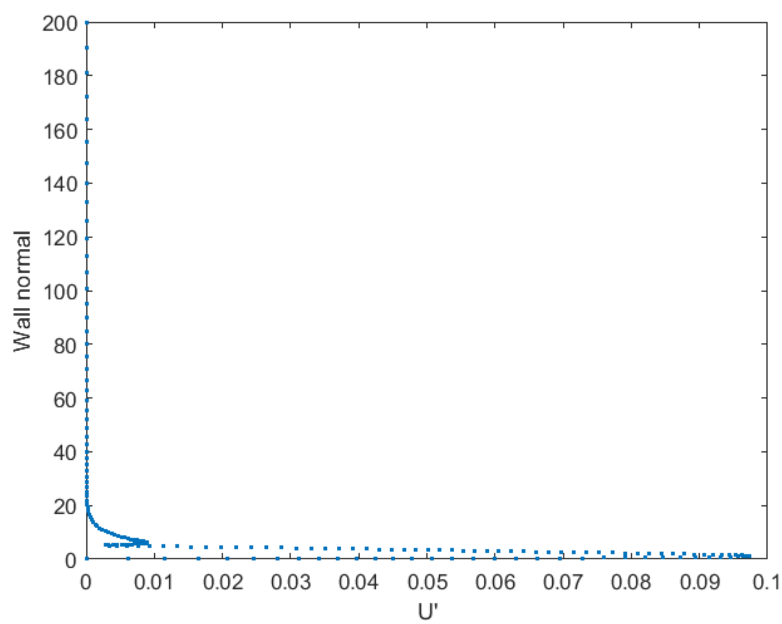

Figure 2.10: A typical 2nd mode disturbance U' velocity profile (shape function)

The shape functions of the resulting eigensolutions are placed through a final simple filtering scheme where its freestream decay, shape function "noisiness", and other quantified characteristics of the mode of interest are analyzed and is given a summed "score". The highest score of all remaining eigensolution is then determined to be the valid eigenmode solution, with an example shown in figure 2.11. It is stressed that this methodology is not guaranteed to filter out and select the valid eigensolution, however it provides a basis for the user to filter out a vast majority of spurious eigensolutions and simplify the analysis task. It is also anticipated that as more user-validated shape functions are appended to the repository and more mode specific metrics are quantified, the likelihood of valid mode-finding also increases. This method is considered to be a temporary workaround for efficiently performing LST on a wide data set until a more permanent method such as Arnoldi or Chebyshev schemes are implemented.

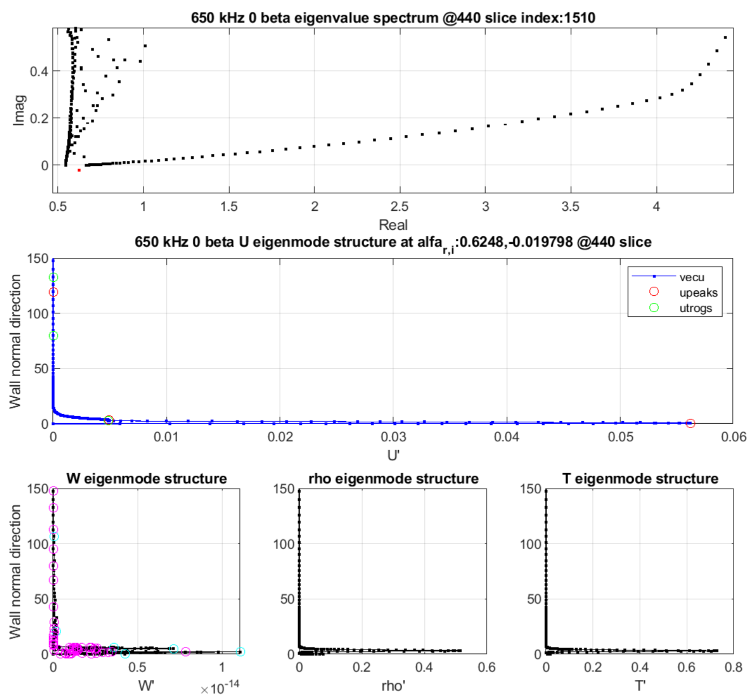

Figure 2.11: Unstable mode detected by JoKHeR at 650 kHz

Chapter 3

ON THE INVISCID ENERGETICS OF MACK'S FIRST MODE INSTABILITY

The following chapter is adapted from [1]

In two-dimensional boundary layers, different instability mechanisms dominate the modal growth phase depending on the flight speed, particularly as the flight profile encompasses both the incompressible and compressible regimes (increasing Mach numbers). Planar Tollmien-Schlichting (TS) waves are the most unstable in the incompressible regime and are known to be driven by phase shifting between the streamwise and wall normal velocity perturbation components, due to the viscous no-slip wall boundary condition. As the Mach number is increased, the boundary layer transition mechanism switches from planar TS wave dominated instabilities to oblique Mack's first mode wave dominated instabilities. It was shown by linear stability theory (LST), that the switch from planar TS wave dominated to oblique Mack's first mode wave dominated is not continuous and occurs at Mach 1, when a generalized inflection point forms in the boundary layer profile [82]. As the boundary-layer-edge Mach number continues to increase, first mode dominated transition persists until the Mach number becomes larger than approximately 4.5 to 6.5, depending on the wall-to-adiabatic temperature ratio, at which point the planar acoustic Mack's second mode becomes dominant.

Despite the long history of hypersonic boundary layer instability calculations (in particular the works of Mack [42, 44]), ambiguity remains concerning the fundamental physical mechanisms governing super/hypersonic boundary layer instability. As mentioned, incompressible boundary layer TS waves are well understood and the thermoacoustic resonance interpretation appears explain Mack's second mode. Thus, the focus of this chapter is an energetics characterization of the instabilities introduced above, with an emphasize on Mack's first mode [42, 83], on a flat plate for a range of Mach numbers. Note, a significant body of literature exists concerning the spectral properties of high-speed boundary layer instabilities (for example [84, 85, 86] with an excellent recent summary provided by [87]). In these and other works, many properties of the spectrum, spectral branching and spectral sensitivity to various parameters have been established. These properties are particularly important when solving the receptivity problem, as forcing can excite different parts of the spectrum [88] which may interact transiently. However, in this chapter, focus is placed on the later stages of disturbance evolution. That is, the dynamics after initial transients have died out is considered. In such cases, all stable modes of the spectrum will become evanescently small, leaving only the unstable modes to dominate the disturbance field. By characterizing the energetics of such disturbances, it is hoped that new insights into the physical mechanisms governing the modal growth route to transition for high-speed boundary layers are gained.

3.1 Problem Formulation

3.1.1 Mathematical Model Formulation

Consider the Euler equations (inviscid Navier-Stokes) ([89] chapter 3):

$$\frac{D\rho}{Dt} = -\rho\nabla\cdot\vec{u} \tag{3.1}$$

$$\rho\frac{D\vec{u}}{Dt} = -\nabla P \tag{3.2}$$

$$\rho\frac{DT}{Dt} - (\gamma-1)M^2\frac{DP}{Dt} = 0. \tag{3.3}$$

Derivation of the total energy equation follows as a series of known steps: $\vec{u}\cdot(3.2) + (T(3.1) + (3.3))$ yielding

$$\underbrace{\frac{1}{2}\rho\frac{D\mathbf{u}^2}{Dt} + M^2\frac{DP}{Dt}}_{\text{energy}} + \underbrace{\vec{u}\cdot\nabla P + \gamma M^2 P\nabla\cdot\vec{u}}_{\text{div. acst. pwr.}} = 0, \tag{3.4}$$

or

$$\underbrace{\frac{1}{2}\rho\frac{D\mathbf{u}^2}{Dt}+\frac{\gamma M^2}{2\rho c^2}\frac{DP^2}{Dt}}_{\text{energy}}+\underbrace{\vec{u}\cdot\nabla P+\gamma M^2 P\nabla\cdot\vec{u}}_{\text{div. acst. pwr.}}=0, \tag{3.5}$$

where $M^2 = \frac{U_e^2}{\gamma R T_e}$, $c = \sqrt{\frac{\gamma P}{\rho}}$, $\gamma = c_p/c_v$, $\mathbf{u}^2 = u^2 + v^2 + w^2$ (with u and v being the streamwise and wall normal components of velocity respectively for the 2D case and w the spanwise velocity component), T is temperature, ρ is density and P is pressure. This is essentially the same as the thermoacoustic energy equation of Nicoud and Poinsot [90]. Other than the inviscid approximation, (3.4) is generally valid. The first two terms represents the Lagrangian derivative of acoustic energy and the second two terms represent the divergence of acoustic power.

To be consistent with the LST methodology, disturbance energy is calculated as follows. Flow variables are decomposed into mean and perturbation components, $\phi = \bar{\phi} + \phi'$. This decomposition is substituted into equations 3.1 - 3.3, and each equation is linearized. Then, these linearized equations are used to construct a disturbance energy equation, 5.1. Sources of disturbance energy are derived from either the divergence of acoustic power or the nonlinear advective terms, and generically take the form of traditional Reynolds stresses or thermal Reynolds stresses. We have assumed 3D flow that is parallel in the X and Z directions. It should be noted that the energy norm derived here is consistent with the energy norm used in the analysis of compressible turbulence [91]. It is also very similar to the Chu energy norm [92], if pressure is expanded into density and temperature perturbation quantities, which is very popular in optimal growth studies [93]. However, here we chose to use the norm consistent with our derivation, beginning with the compressible Euler equations (eqns 3.1-3.3). Note also, based on our past work with Mack's second mode, it is natural to discuss energy budgets in terms of acoustic power. Again, these terms could be expanded into density and temperature disturbance quantities, if desired.

$$\underbrace{\frac{\bar{\rho}}{2}\frac{\bar{D}\langle\vec{u'}^2\rangle}{Dt} + \frac{\gamma M^2}{2\bar{\rho}c^2}\frac{\bar{D}\langle\vec{P'}^2\rangle}{Dt}}_{\text{dist. energy}} = \langle\underbrace{-\bar{\rho}u'v'\frac{\partial\bar{U}}{dy} - \bar{\rho}v'w'\frac{\partial\bar{W}}{dy}}_{\text{velocity advective}}\underbrace{-\left(\vec{u'}\cdot\vec{\nabla}\right)p' - \gamma M^2 P'\left(\vec{\nabla}\cdot\vec{u'}\right)}_{div.\ acst.\ pwr}\rangle. \tag{3.6}$$

3.1.2 Blasius Solution

The canonical Blasius boundary layer profile is considered in this work and a brief derivation is presented for completeness. The flat plate compressible Blasius boundary layer at zero angle of attack is described by the equation ([94] pg 507),

$$(Cf'')' + ff'' = 0 \tag{3.7}$$

$$(Cg')' + Prfg' = -PrC\left(\gamma - 1\right)M^2 f''^2 \tag{3.8}$$

where $C = \frac{\rho\mu}{\rho_e\mu_e}$. We now apply Sutherland's Law

$$\mu = C_\mu \frac{T^{\frac{3}{2}}}{T+S} \qquad (Dimesional) \tag{3.9}$$

with $C_\mu = 1.458 \times 10^{-6}$ and $S = 110.4$. Note $C_\mu = \frac{\mu_{ref}}{T_{ref}^{\frac{3}{2}}}(T_{ref} + S)$, where $\mu_{ref} = 1.716 \times 10^{-5}$ and $T_{ref} = 273.15$. For an ideal gas and constant base state pressure across the boundary layer, $\frac{\rho}{\rho_e} = \frac{T_e}{T}$. Also remember $g = \frac{h}{h_e} = \frac{T}{T_e} \rightarrow T = T_e g$. Putting it all together results in the exactly similar behavior for C:

$$C = \frac{C_\mu T_e^{\frac{1}{2}}}{\mu_e}\frac{g^{\frac{1}{2}}}{g + \frac{S}{T_e}} = C_0\frac{g^{\frac{1}{2}}}{g + C_1}. \tag{3.10}$$

Substitution into the above Blasius equations leads to the final Sutherland's Law Blasius boundary layer equation ([95] chapter 6)

$$f''' = \frac{g'f''}{g + C_1} - \frac{g'f''}{2g} - \frac{ff''\left(g + C_1\right)}{C_0 g^{\frac{1}{2}}} \tag{3.11}$$

$$g'' = \frac{g'^2}{g + C_1} - \frac{g'^2}{2g} - Pr\left(\gamma - 1\right)M^2 f''^2 - \frac{Prfg'\left(g + C_1\right)}{C_0 g^{\frac{1}{2}}} \tag{3.12}$$

These equations are solved with a fourth order Runge-Kutta method, in combination with a shooting method scheme in MATLAB. Several different Mach numbers are considered in this work, but each run assumes that density = 0.0147 kg/m^3 and temperature = 100 K for edge values outside the boundary layer. Also, $\gamma = 1.4$ and adiabatic wall conditions are applied, unless otherwise specified. In addition, all calculations presented in this work are taken for a boundary layer Reynolds number, $R_\delta = \sqrt{\delta\rho_e U_e/\mu_e} = 1000$, where $\delta = \sqrt{x/(\rho_e U_e/\mu_e)}$.

3.2 Stability Results

3.2.1 Subsonic Case

To make clear and complete distinction between TS waves and first mode instability, analysis is initiated with consideration of a sufficiently sub-sonic boundary layer ($M = 0.5$ Blasius boundary layer). The most unstable 2D TS instability is found to have a frequency of 500Hz ($\omega = 0.0005$) with an unstable eigenvalue of $\alpha_{2D} = 0.1448 - 0.0043i$.

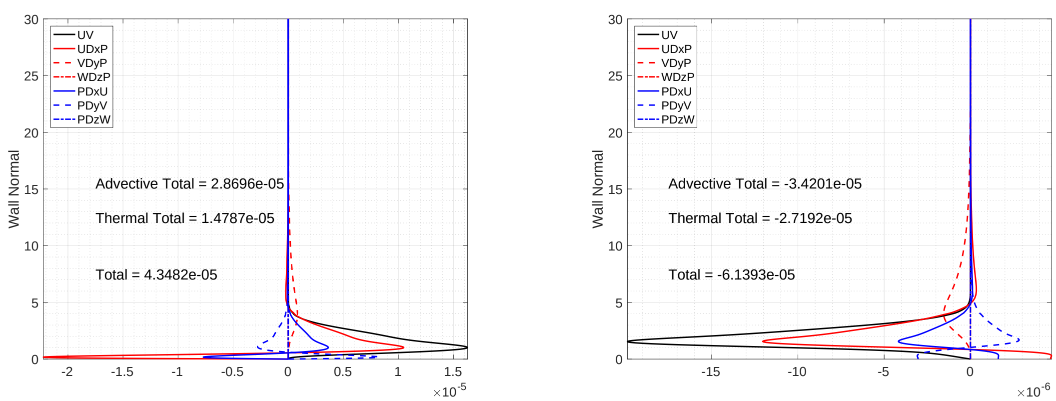

Figure 3.1: Profiles of Reynolds stress energy source/sink terms at $M = 0.5$ with a frequency of 500Hz, $\beta = 0$, and $Re_\delta = 1000$. Left) Regular TS mode: $\alpha_{TS} = 0.1448 - 0.0043i$. Right) 2D mode with slip boundary condition: $\alpha_{TS-slip} = 0.1501 + 0.0085i$.

The fundamental physical process governing TS instability is known to be a phase shifting between the u' and v' velocity disturbances due to the viscous no-slip boundary condition (see Stoke's 2nd problem for details of this phase shifting) [96].

The phase shift results in non-zero advective Reynolds stresses which constitute the energy source of this instability in the fully incompressible limit. Figure 3.1 (left panel) shows that the inviscid energy source for this instability is predominantly the velocity advective terms. Notice that when a slip velocity boundary condition is applied (zero gradient condition for the u' and w' velocity components), the energy source is removed and the disturbance stabilizes (right panel), $\alpha_{2D-slip} = 0.1501 + 0.0085i$. That is, by applying a slip boundary condition, the phase shifting mechanism responsible for TS instability is removed. This is all consistent with the current understanding of TS instability physics.

Note, for the following figures, legends have been labeled as follows: UV indicates tradition Reynolds Stress $-\bar{\rho}u'v'\frac{\partial \bar{U}}{dy}$. UDxP, VDyP and WDzP indicate the components of $-\left(\vec{u}' \cdot \vec{\nabla}\right) p'$. PDxU, PDyV and PDzW indicate the components of $-\gamma M^2 P' \left(\vec{\nabla} \cdot \vec{u}'\right)$. The black dot indicates the location of the generalized inflection point and the red dot indicates the location of the critical layer. All DAP indicates the profile of all the divergence of acoustic power terms, with Thermal Total being the integral total, positive indicating an energy source. Advective Total is the integral of the traditional velocity advective Reynolds Stress terms (UV), positive indicating an energy source. Total is the sum of Thermal Total and Advective Total.

3.2.2 Transonic Case

Next, we consider a slightly compressible boundary layer ($M = 0.9$ Blasius boundary layer, figure 3.2). In general, the same trends as were observed for the $M = 0.5$ case, hold for the $M = 0.9$ case, with the significant addition of unstable oblique modes. At 1300Hz ($\omega = 0.0013$), an unstable 2D mode is found, $\alpha_{2D} = 0.1064 - 0.0041i$ and an unstable oblique mode, $\alpha_{obl} = 0.1061 - 0.0040i$ with azimuthal wave number $\beta = 0.025$ (in the following, β is chosen to consider the most unstable mode). Again, the velocity advective Reynolds stresses are dominant and the slip boundary condition stabilizes the disturbances, $\alpha_{2D-slip} = 0.1105 + 0.0035i$ and $\alpha_{obl-slip} = 0.1102 + 0.0036i$. However, the thermal terms have gained in importance, accounting for approximately

40% and 33% of the energy source of the 2D and 3D disturbances, respectively. Also note, that the oblique disturbance mode presents a larger velocity advective Reynolds stress than the 2D disturbance mode.

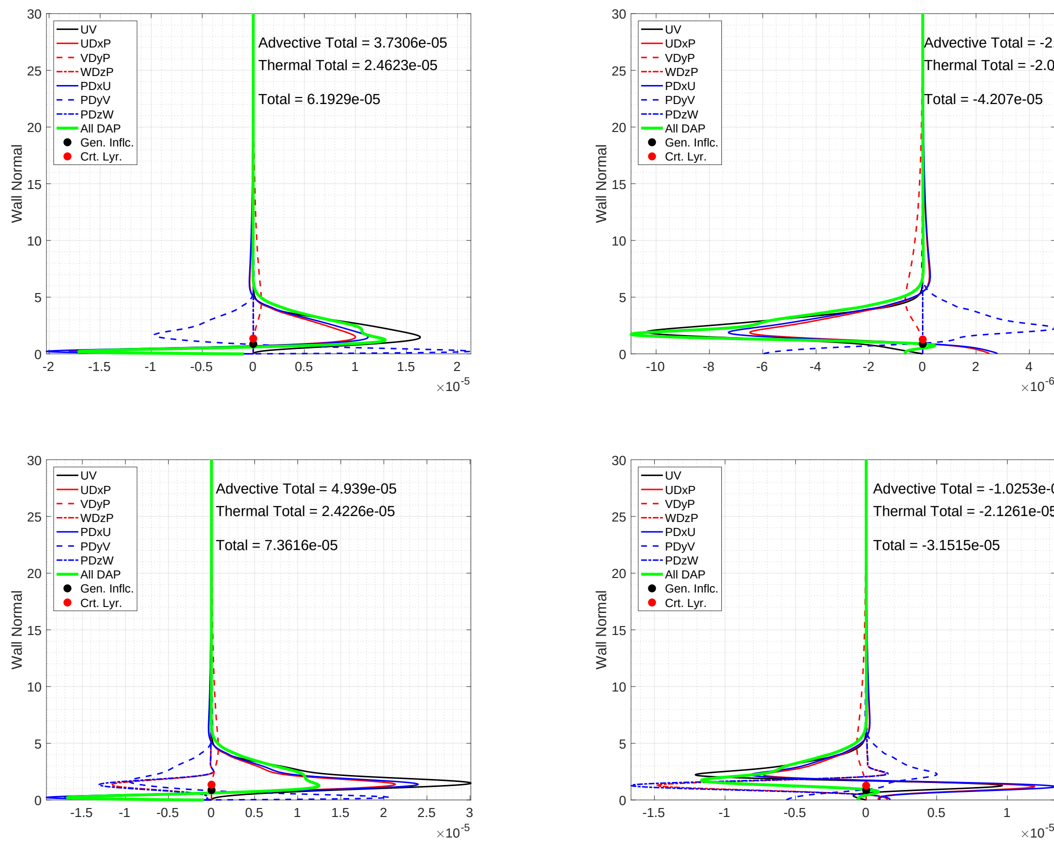

Figure 3.2: Profiles of Reynolds stress energy source/sink terms at $M = 0.9$ with a frequency of 1300Hz, $\beta = 0.025$, and $Re_\delta = 1000$. Upper Left) 2D mode: $\alpha_{2D} = 0.1064 - 0.0041i$. Upper right) 2D mode with slip boundary condition: $\alpha_{2D-slip} = 0.1105 + 0.0035i$. Lower left) Oblique mode: $\alpha_{Obl} = 0.1061 - 0.0040i$. Lower right) Oblique mode with slip boundary condition:$\alpha_{Obl-slip} = 0.1102 + 0.0036i$.

As the edge flow conditions becomes supersonic, i.e., the edge Mach number becomes larger than 1, a generalized inflection point appears in the profile, and the following trends are observed:

- The oblique disturbance modes become more unstable than the 2D modes.
- The stabilizing effects of the slip boundary condition is reduced.

- The energy source for the instabilities drifts away from the wall to the vicinity of the generalized inflection point.

3.2.3 Super/ Hypersonic Cases

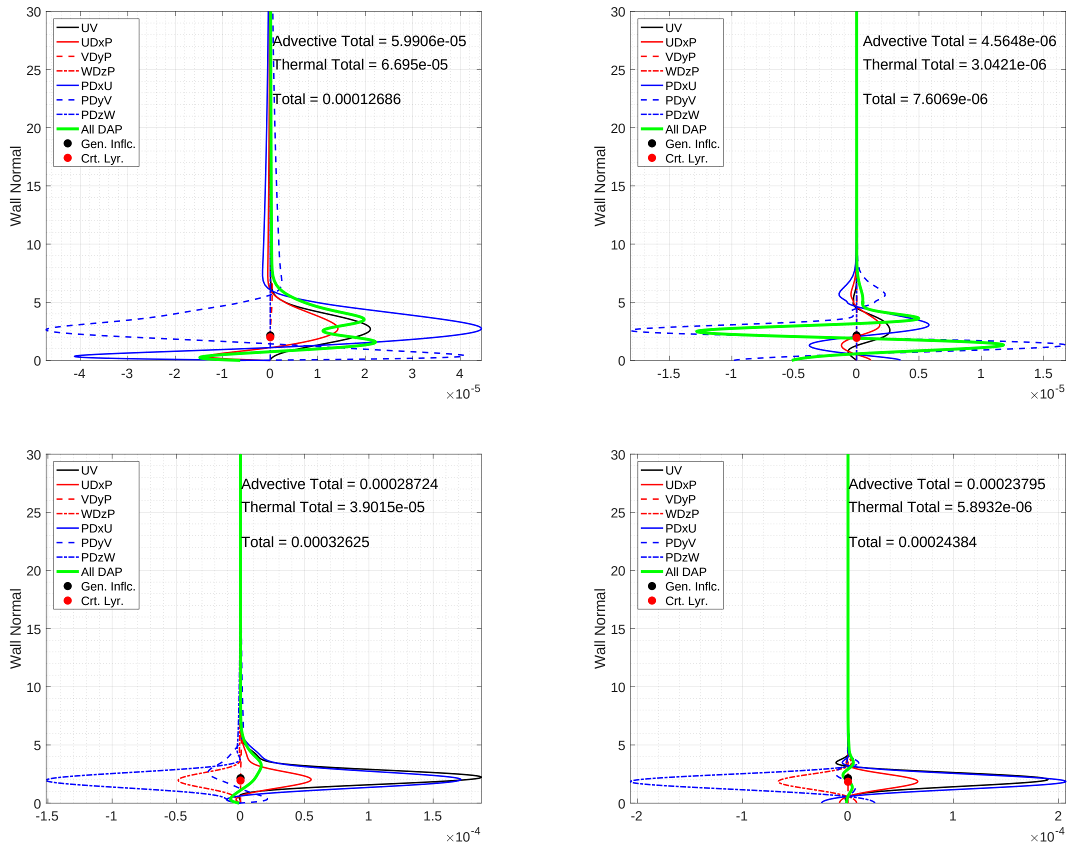

Figure 3.3: Profiles of Reynolds stress energy source/sink terms at $M = 1.5$ with a frequency of 2200Hz, $\beta = 0.075$, and $Re_\delta = 1000$. Upper Left) 2D mode: $\alpha_{2D} = 0.0542 - 0.0020i$. Upper right) 2D mode with slip boundary condition: $\alpha_{2D-slip} = 0.0557 - 0.00005i$. Lower left) Oblique mode: $\alpha_{Obl} = 0.0548 - 0.0035i$. Lower right) Oblique mode with slip boundary condition:$\alpha_{Obl-slip} = 0.0580 - 0.0005i$.

At $M = 1.5$ (2200Hz, $\omega = 0.0022$, $\alpha_{2D} = 0.0542 - 0.0020i$, $\alpha_{2D-slip} = 0.0557 - 0.00005i$, $\alpha_{Obl} = 0.0548 - 0.0035i$, $\alpha_{Obl-slip} = 0.0580 - 0.0005i$), the contribution of velocity advective and thermal Reynolds stresses are balanced for the 2D mode energetics, while velocity advection continues to dominate the oblique disturbance (figure 3.3). Also, the slip condition is unable to stabilize either mode.

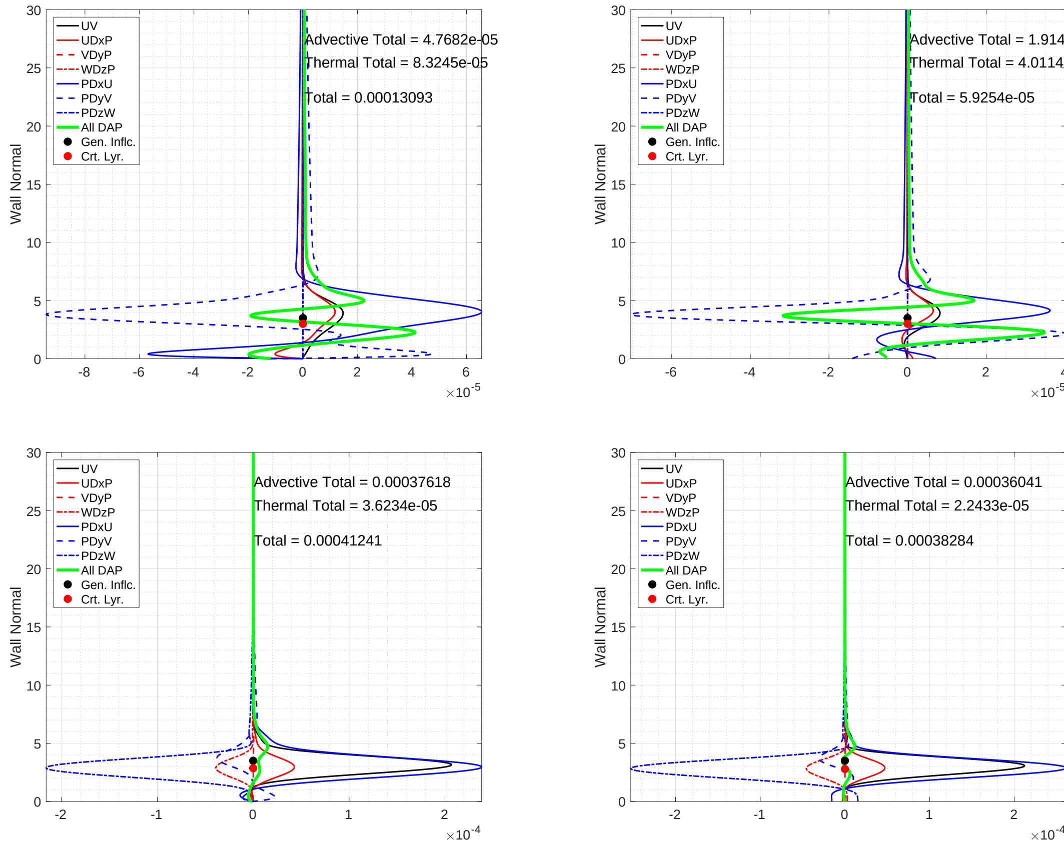

Figure 3.4: Profiles of Reynolds stress energy source/sink terms at $M = 2$ with a frequency of 4250Hz, $\beta = 0.090$, and $Re_\delta = 1000$. Upper Left) 2D mode: $\alpha_{2D} = 0.0475 - 0.0008i$. Upper right) 2D mode with slip boundary condition: $\alpha_{2D-slip} = 0.0475 - 0.0003i$. Lower left) Oblique mode: $\alpha_{Obl} = 0.0507 - 0.0024i$. Lower right) Oblique mode with slip boundary condition:$\alpha_{Obl-slip} = 0.0513 - 0.0012i$.

$M = 2.0$ (4250Hz, $\omega = 0.0043$, $\alpha_{2D} = 0.0475 - 0.0008i$, $\alpha_{2D-slip} = 0.0475 - 0.0003i$, $\alpha_{Obl} = 0.0507 - 0.0024i$, $\alpha_{Obl-slip} = 0.0513 - 0.0012i$) is similar to $M = 1.5$ but with an increased important of the thermal terms and a clear dominance of the oblique instability (figure 3.4).

At $M = 3.0$ (20kHz, $\omega = 0.0200$, $\alpha_{2D} = 0.0747 - 0.0010i$, $\alpha_{2D-slip} = 0.0748 - 0.0001i$, $\alpha_{Obl} = 0.0762 - 0.0024i$, $\alpha_{Obl-slip} = 0.0763 - 0.0024i$), the trend continues and we see the oblique disturbance unaffected by the slip/no-slip boundary condition (figure 3.5).

By $M = 4.0$ (60kHz, $\omega = 0.0601$, $\alpha_{2D} = 0.1103 - 0.0013i$, $\alpha_{2D-slip} = 0.1104 -$

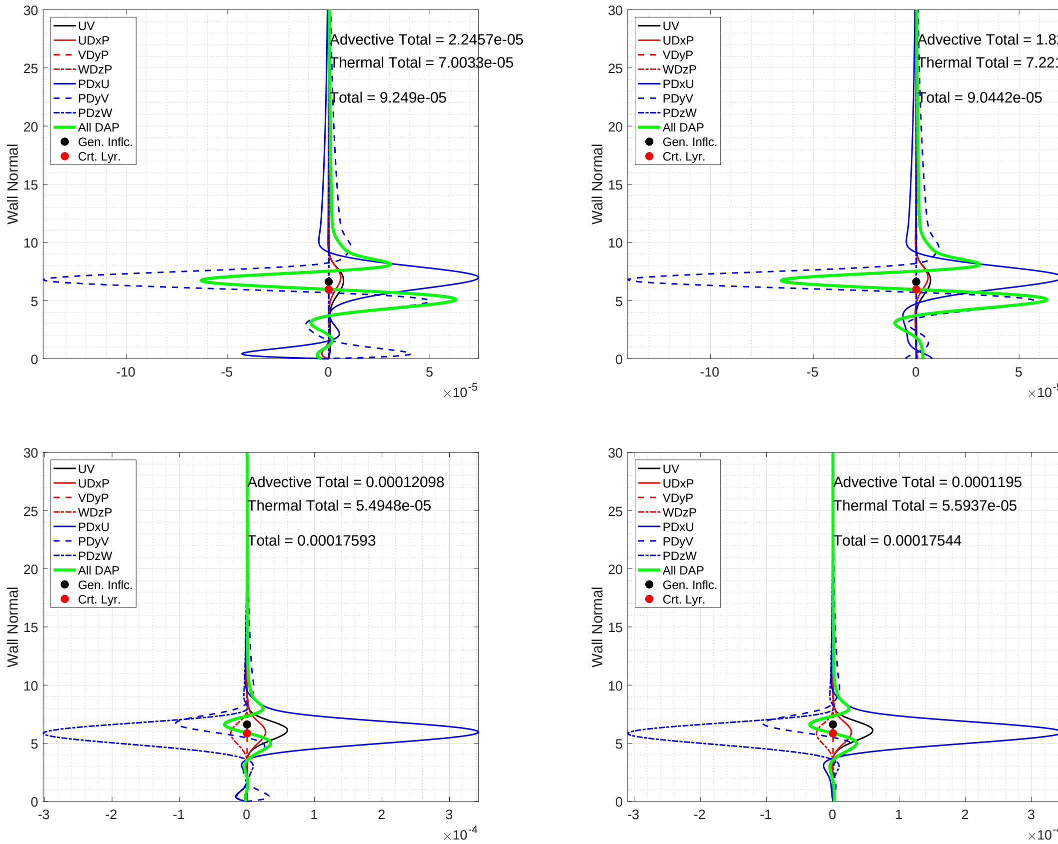

Figure 3.5: Profiles of Reynolds stress energy source/sink terms at $M = 3$ with a frequency of 20kHz, $\beta = 0.075$, and $Re_\delta = 1000$. Upper Left) 2D mode: $\alpha_{2D} = 0.0747 - 0.0010i$. Upper right) 2D mode with slip boundary condition: $\alpha_{2D-slip} = 0.0748 - 0.0001i$. Lower left) Oblique mode: $\alpha_{Obl} = 0.0762 - 0.0024i$. Lower right) Oblique mode with slip boundary condition:$\alpha_{Obl-slip} = 0.0763 - 0.0024i$.

$0.0012i$, $\alpha_{Obl} = 0.1105 - 0.0023i$, $\alpha_{Obl-slip} = 0.1106 - 0.0023i$), the slip/no-slip boundary condition has lost its control over both the oblique and 2D modes, which is consistent with the observation that the dominant energy source terms are removed from the boundary and concentrated in the vicinity of the generalized inflection point (figure 3.6).

At $M = 5.0$ (75kHz, $\omega = 0.0751$, $\alpha_{2D} = 0.0855 - 0.0011i$, $\alpha_{2D-slip} = 0.0856 - 0.0011i$, $\alpha_{Obl} = 0.0855 - 0.0023i$, $\alpha_{Obl-slip} = 0.0856 - 0.0023i$), the thermal Reynolds stresses begin to dominant over the advective velocity Reynolds stresses for the 2D mode (figure 3.7) and by $M = 6.0$ (85kHz, $\omega = 0.0851$, $\alpha_{2D} = 0.0658 - 0.0007i$,

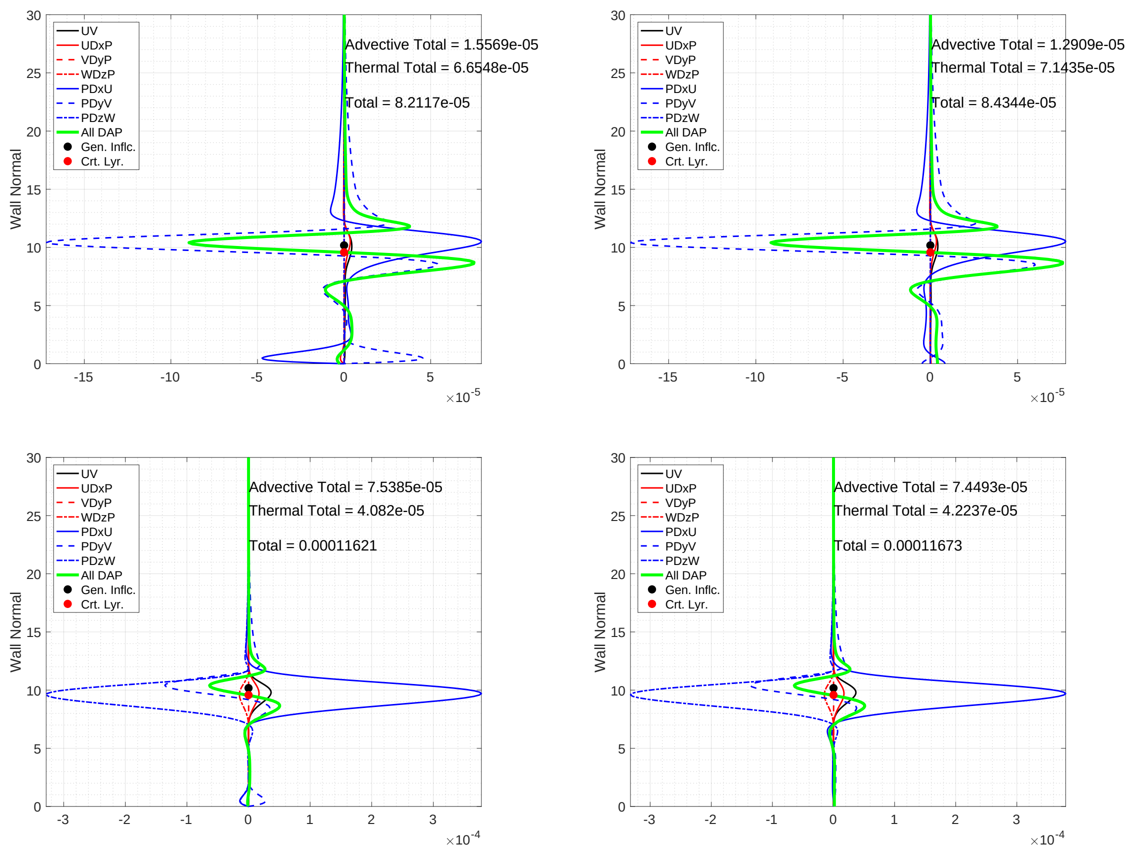

Figure 3.6: Profiles of Reynolds stress energy source/sink terms at $M = 4$ with a frequency of 60kHz, $\beta = 0.110$, and $Re_\delta = 1000$. Upper Left) 2D mode: $\alpha_{2D} = 0.1103 - 0.0013i$. Upper right) 2D mode with slip boundary condition: $\alpha_{2D-slip} = 0.1104 - 0.0012i$. Lower left) Oblique mode: $\alpha_{Obl} = 0.1105 - 0.0023i$. Lower right) Oblique mode with slip boundary condition:$\alpha_{Obl-slip} = 0.1106 - 0.0023i$.

$\alpha_{2D-slip} = 0.0659 - 0.0007i$, $\alpha_{Obl} = 0.0660 - 0.0017i$, $\alpha_{Obl-slip} = 0.0660 - 0.0018i$), the thermal Reynolds stresses are dominant for both 2D and oblique disturbances (figure 3.8). Note that, at $M = 6.0$ (190kHz, $\omega = 0.1903$, $\alpha_{2D-Mack-Mode} = 0.1433 - 0.0040i$), Mack's second mode was also calculated. It is observed that the energy source of second mode instability is dominated by the divergence of acoustic power (figure 3.8). This is consistent with thermoacoustic interpretation of second mode instability [97], suggesting that second mode behaves as a thermoacoustic resonance, and is clearly distinct from the first mode energetics which are concentrated around the generalized inflection point.

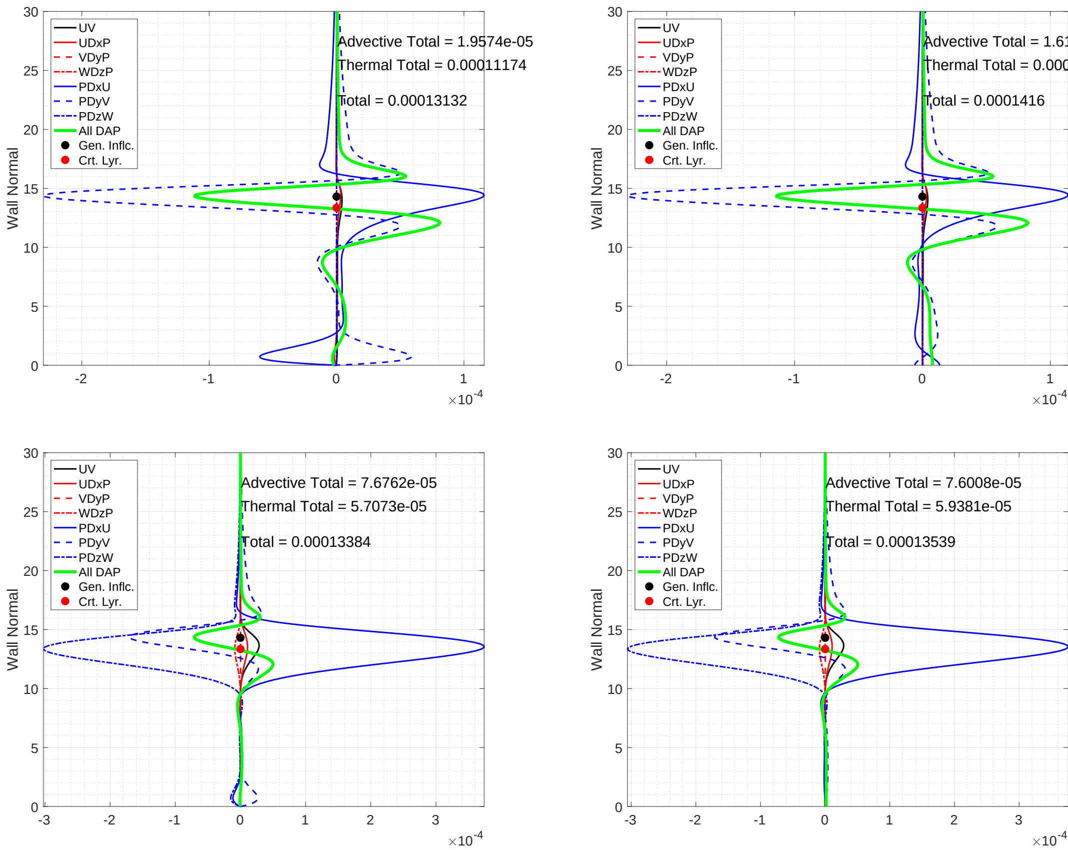

Figure 3.7: Profiles of Reynolds stress energy source/sink terms at $M = 5$ with a frequency of 75kHz, $\beta = 0.100$, and $Re_\delta = 1000$. Upper Left) 2D mode: $\alpha_{2D} = 0.0855 - 0.0011i$. Upper right) 2D mode with slip boundary condition: $\alpha_{2D-slip} = 0.0856 - 0.0011i$. Lower left) Oblique mode: $\alpha_{Obl} = 0.0855 - 0.0023i$. Lower right) Oblique mode with slip boundary condition:$\alpha_{Obl-slip} = 0.0856 - 0.0023i$.

3.3 Discussion

Based on an inviscid energetics investigation, the distinct energetics signatures of TS, first mode and second mode instability have been identified. As expected, Tollmien-Schlichting (TS) waves are driven by phase shifting between the streamwise and wall normal velocity perturbation components. Physically, this phase shifting is caused by the viscous no-slip condition at the wall. Despite links reported in the literature between the spectrum of TS waves and first mode waves [84], here it is found that once initial transients have died out and the disturbance field is dominated by only unstable modes, that first mode waves have a distinctly different energetics signature

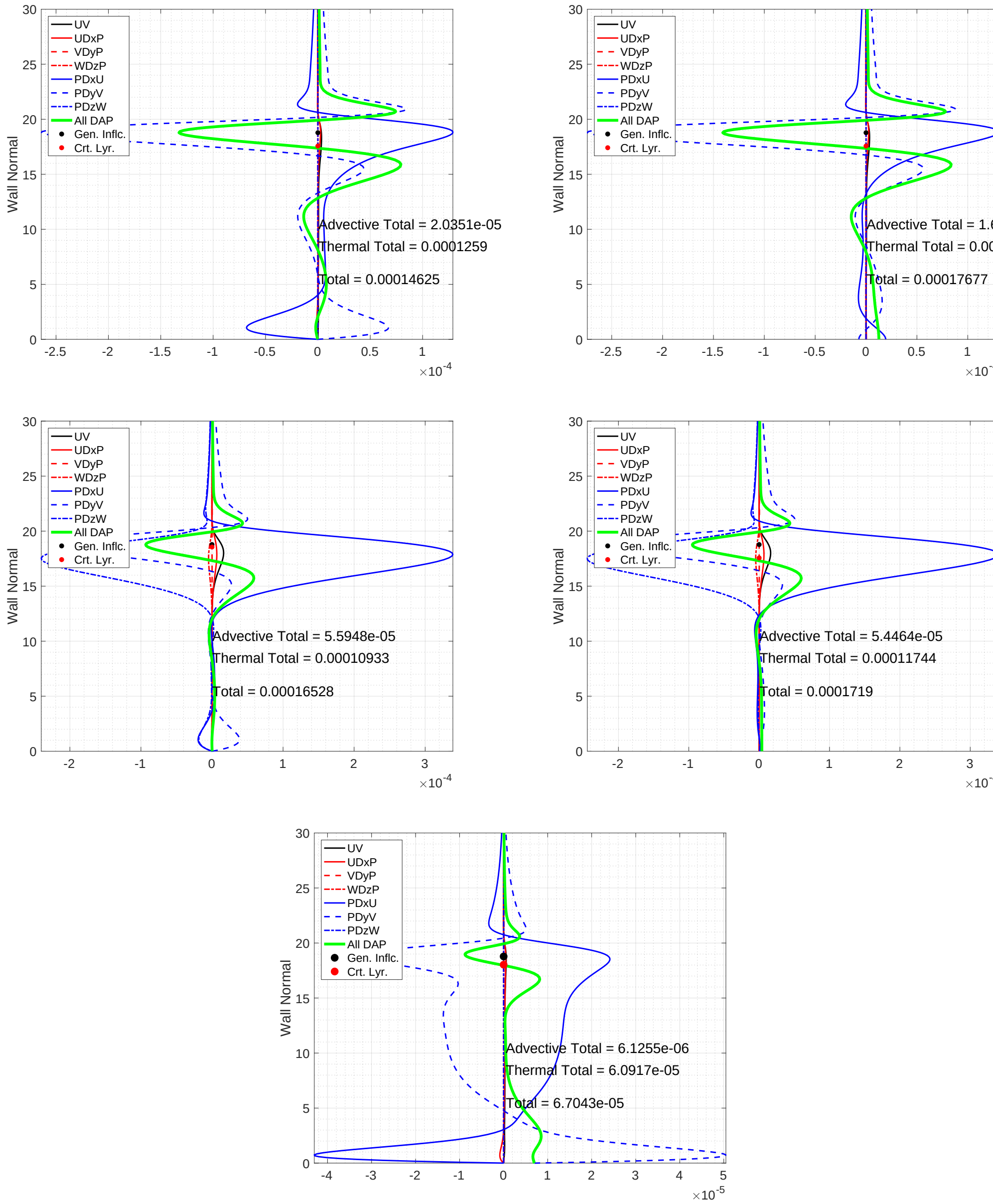

Figure 3.8: Profiles of Reynolds stress energy source/sink terms at $M = 6$ with a frequency of 85kHz, $\beta = 0.0660$, and $Re_\delta = 1000$. Upper Left) 2D mode: $\alpha_{2D} = 0.0658 - 0.0007i$. Upper right) 2D mode with slip boundary condition: $\alpha_{2D-slip} = 0.0659 - 0.0007i$. Middle left) Oblique mode:$\alpha_{Obl} = 0.0660 - 0.0017i$. Middle right) Oblique mode with slip boundary condition:$\alpha_{Obl-slip} = 0.0660 - 0.0018i$. Lower Central) A 190kHz Mack's second mode $\alpha_{2D-Mack-Mode} = 0.1433 - 0.0040i$

than TS waves. Indeed, it is found that first mode energy is derived from a phase shifting between streamwise velocity and pressure perturbations in the vicinity of the generalized inflection point. Though it is observed that at moderate Mach numbers the thermal and velocity advective Reynolds stresses interact.

3.3.1 Effect of increasing Mach number on the energy totals

It is seen that in the purely subsonic regime with a no-slip condition applied, the unstable mode appears to be a 2d mode with advective terms dominating the Reynolds stress energy source. Summation of all thermal components of the Reynolds stress yields near net zero value, indicating that the advective component is the sole dominating source of energy into the instability.

As Mach number is increased from M0.5 to M0.9, the most unstable mode starts to appear as an oblique mode rather than a 2d mode. While the advective component is still dominating the energy source, there is now a net non-zero thermal component which is increasing. The location of the critical layer is slightly above the generalized inflection point, which is itself very close to the wall.

At M1.5, for the 2d unstable mode, the thermal total balances with the advective total, with it being slightly above the advective. The most unstable mode for this case is still the oblique mode with its advective total dominating over the thermal. The location of the critical layer appears to now be below the generalized inflection point. The generalized inflection point is increasingly being pushed off the wall. This trend continues to hold as the Mach number is increased to M2 and M3. The thermal total dominates over the advective total for the 2d mode while vice versa for the oblique mode.

At M4, while the previous trends still hold, there is a noticeable increase in the thermal total for the unstable oblique mode with the increase in Mach number. The location of the generalized inflection point and the critical layer are increasingly being pushed off the wall with the generalized inflection point increasing its distance from above the critical layer.

At M5, the thermal total dominates for the 2d case. For the oblique mode, while the advective total is still dominant, the thermal total is reaching parity with the advective and starting to slightly dominate over the advective. The location of the generalized inflection point and critical layer continues to follow the previous seen trends.

Finally at M6, for the 2d mode, the thermal total overly dominates the advective total. Interestingly noted here is that for the oblique mode, the thermal total now appears to be greater than that of the advective total and is now dominant. The location of the generalized inflection point and critical layer continues to follow the previous seen trends.

3.3.2 Effect of the slip condition

Generally, the viscous mechanisms responsible for the phase shift between the disturbance velocity components are due to the no-slip wall conditions. For the subsonic M0.5 case, the implementation of the slip condition on the wall (a zero gradient condition for the u' and w' velocity components), appears to suppress the unstable 2d mode such that it becomes completely stable as the energy terms for both the advective and thermal components both go negative. This is indication that the classical interpretation of the energy mechanisms of TS waves are correct. However, as Mach number is increased and the compressible regime is fully realized, the slip condition does not appear to have any affect on the stabilization of either the 2d or oblique modes. This implies that the energy mechanisms that has been previously prescribed for TS modes do not completely apply to the supersonic 1st mode. This is consistent with an interpretation that the energy source terms driving 1st mode instability are displaced from wall boundary and instead concentrated in the vicinity of the generalized inflection point.

3.4 Conclusion

It is important to emphasize that the first mode energy source is driven by dynamics 'off the wall' while the TS wave energy source is driven by dynamics 'at the wall.' This was emphasized by considering the sensitivity to the slip or no-slip wall boundary condition. It was found that the first mode was insensitive to the slip boundary conditions for Mach numbers greater than 2. Finally, is was shown that second mode instability energetics are driven by a phase shifting between wall-normal velocity and pressure perturbations, consistent with the thermoacoustic resonance interpretation [97]. Note, as the LST code is viscous and the energetics analysis is inviscid, a complete energy accounting has not been considered. However, a complete accounting is not necessary to gain insight into the fundamental physical mechanisms associated with the instabilities considered, as the neglected effects of viscosity and thermal conduction are likely to be solely dissipative.

Chapter 4

DESIGN OF A FLARED CONE FOR FIRST-SECOND MODE MECHANISMS INTERACTIONS

The following chapter is adapted from [98]

Over the last couple of decades, research on laminar-turbulent transition physics have shed considerable insights on the behavior of high speed transition mechanisms. However, as flight technologies continue to advance, the emergence of unique phenomena and complications common to the more complex flight geometries and parameters begin to be come more relevant. With the understanding of some of the driving mechanisms for various modal instabilities as described in the previous chapter, one question that must now be considered is that of multiple interacting instabilities. As most common research to date has been focused on cases where a single type of instability is dominant, transition for these new cases are likely to be subject to multiple competing instability mechanisms and thus, the prediction schemes developed from the primitive canonical geometries may be ineffective at predicting transition on these more complex flight geometries and profiles.

Here attention is focused on the interactions between the first and second Mack modes, with the goal of designing a Mach 5 flared cone which will allow for the experimental study of these instability types. That is, our goal is to design a geometry which will allow for study of:

1. The dynamics of a first-mode instability in a second-mode dominated boundary layer.
2. The dynamics of a second-mode instability in a first-mode dominated boundary layer.
3. The transitional dynamics of a boundary layer in which the first- and second mode instability mechanisms interact.

Note, the intent of 1 and 2 is the study the behavior of the less dominant mode in the "perturbed basic state" [35] of the dominant mode, while the intent of 3 is to focus not on modes but instead on generating mechanisms. This study is not just emphasizing understanding of direct interactions between first- and second-mode waves, but also in the potential interactions between the physical mechanisms which are responsible for driving growth of first- and second-mode instability.

4.1 Geometry and Basic states

It is known that wall heating/cooling and geometry curvature (Johnson et at., Juliano et al., Fedorov et al., Batista et al.) [99, **?**, 100, 45] both exhibit a controlling influence over first- and second-mode instability. Thus, the first step in this analysis was to calculate a set of basic flow states which span an experimentally feasible parameter space of cone flare radii and wall temperature. These basic state solutions can be described as the background or initial state of the system to which stability analysis is then applied. Here, the basic states are calculated utilizing US3D. To avoid entropy layer effects (Stetson et al., Batista et al.)[101, 45], a nominally sharp nosed geometry is chosen for analysis. The initial parameter space considered spanned cone flare radii from 2.5 to 3.5 meters and 250K to 350K wall temperatures.

Due to the flared nature of the cone, a MATLAB script was created to parametrically generate the cone geometry for import into a CAD software for model creation. Four user specified input arguments, flare radius, cone tip radius, cone length and opening angle (1.5 ° was used), are used to create the cone profile. To identify a flared cone as "sharp", a small but finite ($\approx$ 0.15mm to allow the model to be physically realized) cone tip radius is specified. The flared cone geometry is generated utilizing modified parameterized equations for a circle, with the resulting x and y coordinate data imported into a Solidworks which provides a basis for meshing in Pointwise.

For this study, the flow parameters similar to the nominal operating conditions of the Mach 5 tunnel at the University of Arizona were utilized. Wall temperatures

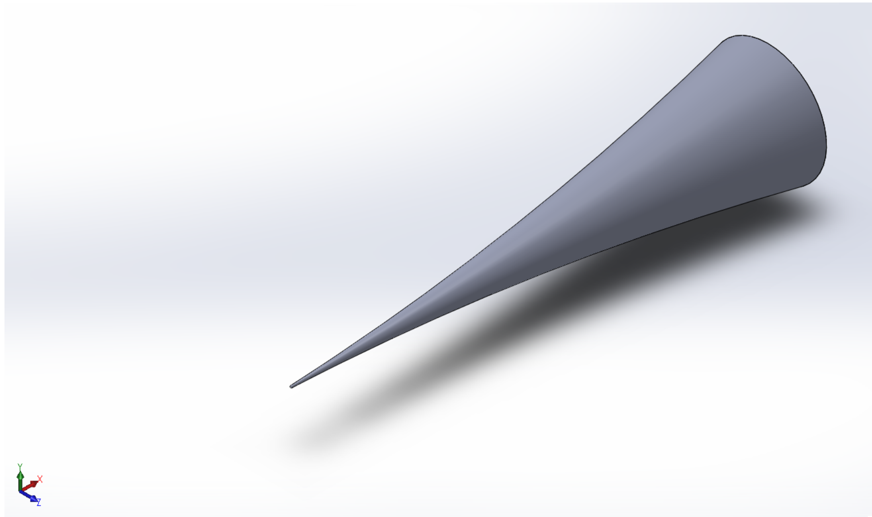

Figure 4.1: A 0.5m length, 300K wall temperature, 3m flare radius cone geometry used as one of the base cases

ranging from 250K to 350K (and eventually to 700K) were also selected for investigation (figure 1). The 'base' case (motivated by works of Chynoweth et al.[102, 15]) is a "sharp" cone with 3m flare radius at 300K wall temperature and flow conditions corresponding to table 1.

M_∞	$\rho_\infty(kg/m^3)$	$T_\infty(K)$	$T_{wall}(K)$	$U_\infty(m/s)$
5	1.362e^{-}1	66.667	300	818.3337

4.2 Stability Analysis

4.2.1 LST

A standard LST analysis of basic states with conditions spanning wall temperatures and curvatures about the base case (0.5m long cone at 300K with 3m flare radius) is performed. Results for cones with flare radius ranging from 2.5m to 3.5m along with wall temperatures from 250K to 350K are shown in figure 4.3. As first-mode instability is oblique (travels at an angle to the mean flow) a range of spanwise wavenumbers, β_z , are considered. Note, in the figure only the most unstable wave is plotted and isolines of spanwise wave number are provided.

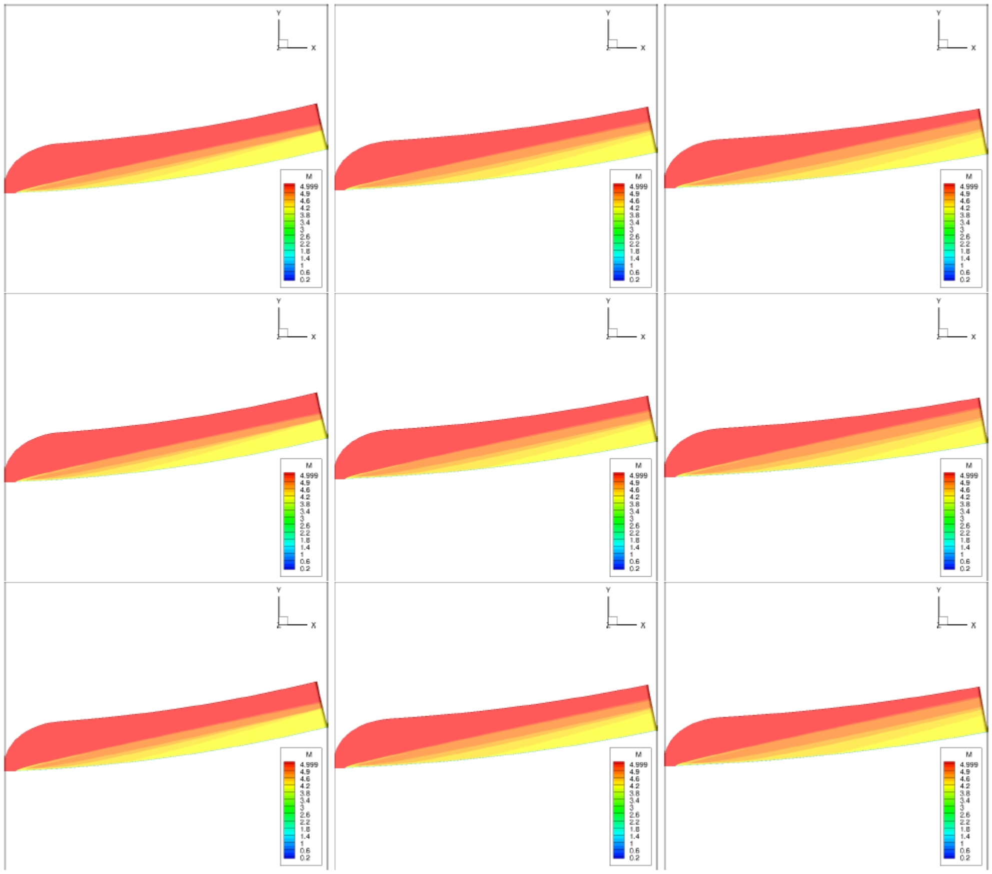

Figure 4.2: Basic state Mach contour plots of flared cones. Top row: 250K wall temperature. Middle row: 300K wall temperature. Bottom row: 350K wall temperature. Left column: 2.5m flare. Middle column: 3.0m flare. Right column: 3.5m flare.

It can readily be seen that with increasing wall temperature, comes a strengthening of the first-mode and a lowering of the most unstable second-mode frequency. Also, with an increasing flare radius, comes a lowering of the most unstable second-mode frequency and a slight weakening of the first-mode instability. With the goal being to generate an "overlap region" between the first- and second-mode instability, the data trends indicate that larger flare radius and hotter temperatures are required. The set of basic state calculation was thus extended to include: 4m flare with 400K wall temperature, 5m flare with 500K wall temperature, 6m flare with 600K wall temperature and 7m flare with 700K wall temperature cones. In addition, the cones were extended in length to 1m.

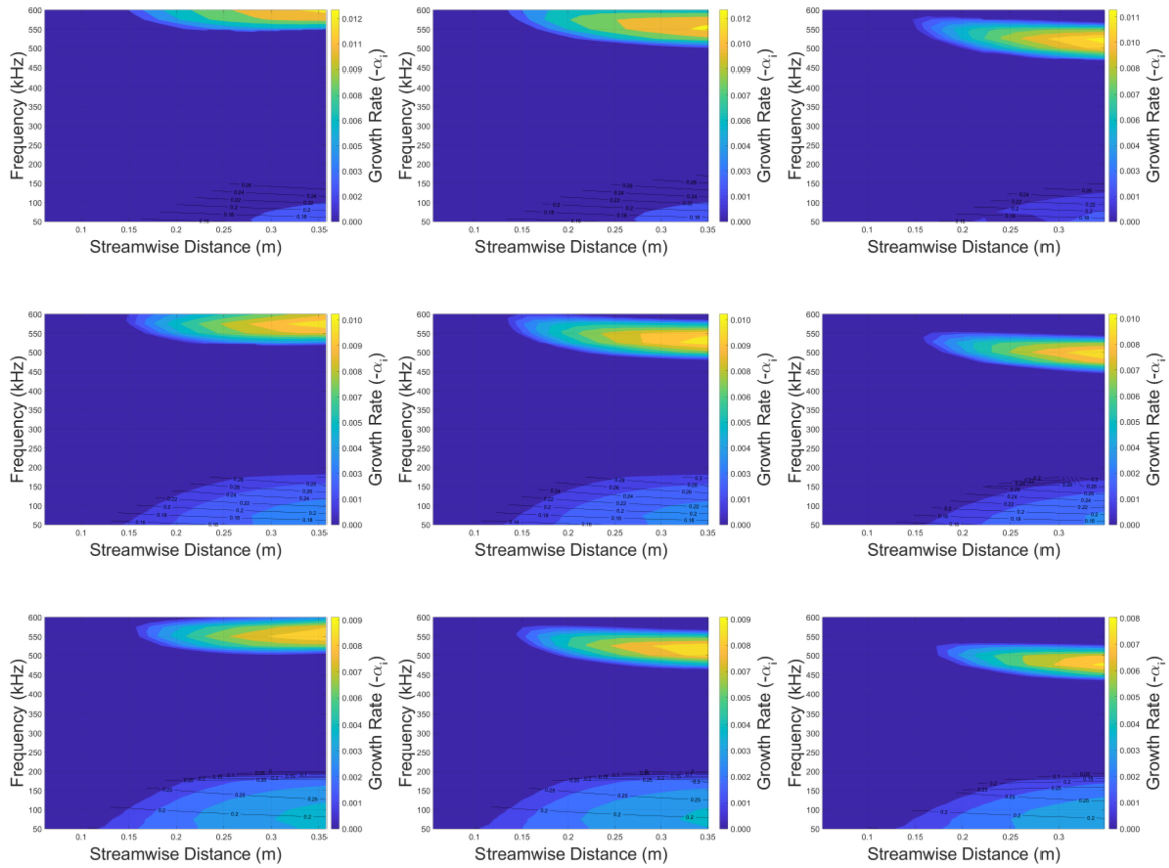

Figure 4.3: LST base stability diagrams for 0.5m long cones each basic flow state with varying wall temperature (250K-350K) and flare radius (2.5m-3.5m) and β_z contour lines. Top row: 250K wall temperature. Middle row: 300K wall temperature. Bottom row: 350K wall temperature. Left column: 2.5m flare. Middle column: 3.0m flare. Right column: 3.5m flare.

LST analysis of these new basic states are shown in figure 4.4. It is found that the first- and second-mode regions just begin to overlap for the 6m flare with 600K wall temperature case, and more fully so for the 7m flare with 700K wall temperature case. It is also observed that the azimuthal wave numbers vary slightly with wall temperature and flare radii and that β_z rapidly approaches zero towards the upper frequency portion of the stability diagram normally associated with first-mode instability, in the cases where first- and second-mode instability regions are in close proximity.

4.2.2 LPSE

An LPSE analysis was also performed on frequencies where instability was detected on the 1m long flared cones, to provide an estimate of integrated disturbance amplitude. Second-mode results are shown in figure 4, while first-mode results are shown in figure 5. It is noticed that second-mode dominates the transitional dynamics of the 3m-300K, 4m-400K and 5m-500K cones. The first-mode becomes dominant for the 6m-600K case. For the 7m-700K case, the first-mode continues to dominate transition but the distinction between second-mode and the $\beta_z = 0$ portion of the stability diagram, often associated with the first-mode, becomes ambiguous. Thus, the 5m-500K case appears to be a good candidate for goal 1 (first-mode dynamics in a second-mode dominated boundary layer) and the 6m-600K case appears to be a good candidate for goal 2 (second-mode evolving in a first-mode dominated boundary layer). The 7m-700K case provides an example of a case where the first- and second-mode dynamical mechanisms interact. However, this interaction does not dominate the transitional dynamics, as such experimental investigation would not be possible. Thus, this case only partially satisfies goal 3 and a continued parameter study is being conducted in an effort to further suppress first-mode instability such that the dynamics of competing first- and second-mode mechanisms can be studied.

4.2.3 Note on Phase Locking

It is important to clarify goal 3: first-mode – second-mode interactions. Following Carpenter et al. [103], there are two criteria for traveling wave interaction: 1) The first is Phase Locking. This occurs when the relative phase speeds of the waves is zero. 2) The second is that the relative phase of the waves must be such that interaction occurs. This will be case and wave dependent. Satisfaction of these two conditions may lead to wave interactions that can alter the transitional dynamics of the boundary layer. From the phase speeds calculated with LPSE (figures 4.6 and 4.5), it is evident that phase locking between the first- and second-modes is unlikely to occur. However, it is still possible to study cases where the mechanisms generating first- and second-mode instability overlap (viscous instability mechanism may couple with the acoustic mechanism).

4.2.4 Görtler Modes

In addition to first- and second-mode instability, flared cones are also susceptible to Görtler instability Chynoweth et al. [15]. For the individual analysis of goals 1 and 2, the presence of Görtler instability does not effect the numerical investigation, but may play a significant role in the actual transitional dynamics of the system and hence would be present in experimental data. Sivasubramanian et al. [104] and Hader et al. [105] have extensively study the formation of streaks on flared cones. Figure 4.9 shows the presence of Görtler instability at a section 0.456m from the cone tip for the 3m-250K, 3m-300K and 3m-350K cases. Notice that the most unstable Görtler modes fall in a wavenumber range of around 0.7-0.8. This is roughly 4 times that observed for the first-mode instability, which may limit interactions. Also, the Görtler instability strength dampens with increased radius of curvature, so it is anticipated that the presence of Görtler instability will not have a significant effect on future first mode – second mode interactions studies (though this should be checked explicitly). It is also interesting to note the sensitivity of the Görtler instability to wall temperature. Görtler instability arises due to concave geometry curvature and is not often associated with wall temperature effects. Though, here it is observed that increasing wall temperature appears to dampen the Görtler instability.

4.2.5 Summary

The intent of this work was to design Mach 5 flared cones for future studies of first mode – second mode interactions with the goal to study three cases: 1) The dynamics of a first-mode instability in a second- mode dominated boundary layer. 2) The dynamics of a second-mode instability in a first-mode dominated boundary layer. 3) The transitional dynamics of a boundary layer in which the first- and second-mode instability mechanisms interact. Via linear stability analysis (LST, LPSE) it was determined that a 5m- 500K flared cone design is a good candidate for goal 1; a 6m-600K flared cone is a good candidate for goal 2; a 7m-700K flared cone design can be used to partially study goal 3. However, for goal 3, direct interaction between first- and second-modes via phase locking is unlikely and ultimately the transitional dynamics will be first-mode dominated. Thus, goal 3 requires further revision. Though, it does allow for numerical study of interactions between the viscous and acoustic mechanisms responsible for generating first- and second-mode instability. Finally, it was noted (perhaps somewhat surprisingly) that increased wall temperature has the effect to dampen Görtler instability in the cases studied.

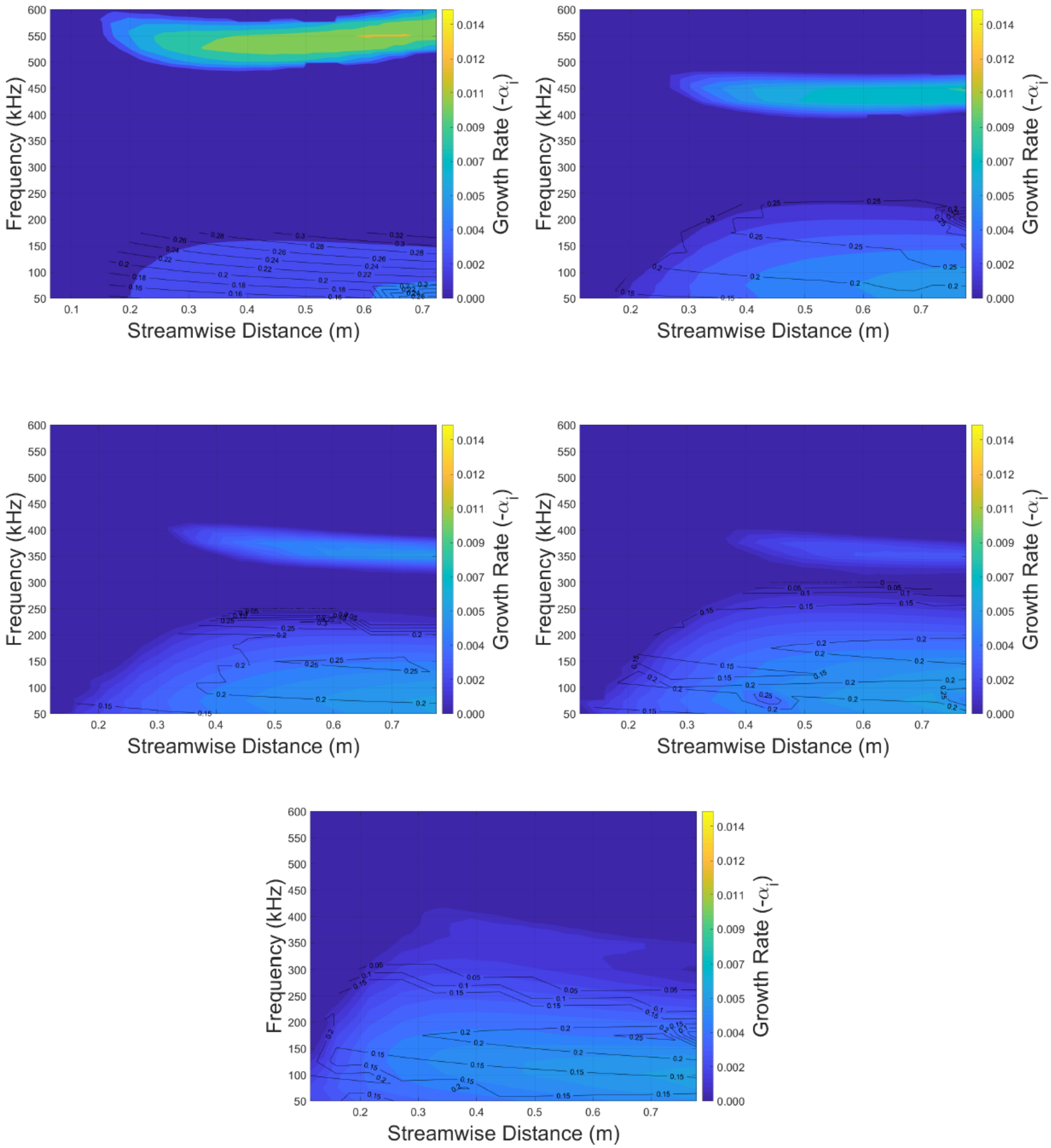

Figure 4.4: LST base stability diagrams of 1m long flared cones for each basic flow state with varying wall temperature (300K-700K) and flare radius (3m-7m). Top row left-to-right: 300K wall temperature 3m flare, 400k wall temperature 4m flare, 500K wall temperature 5m flare. Bottom row left-to-right: 600K wall temperature 6m flare, 700K wall temperature 7m flare.

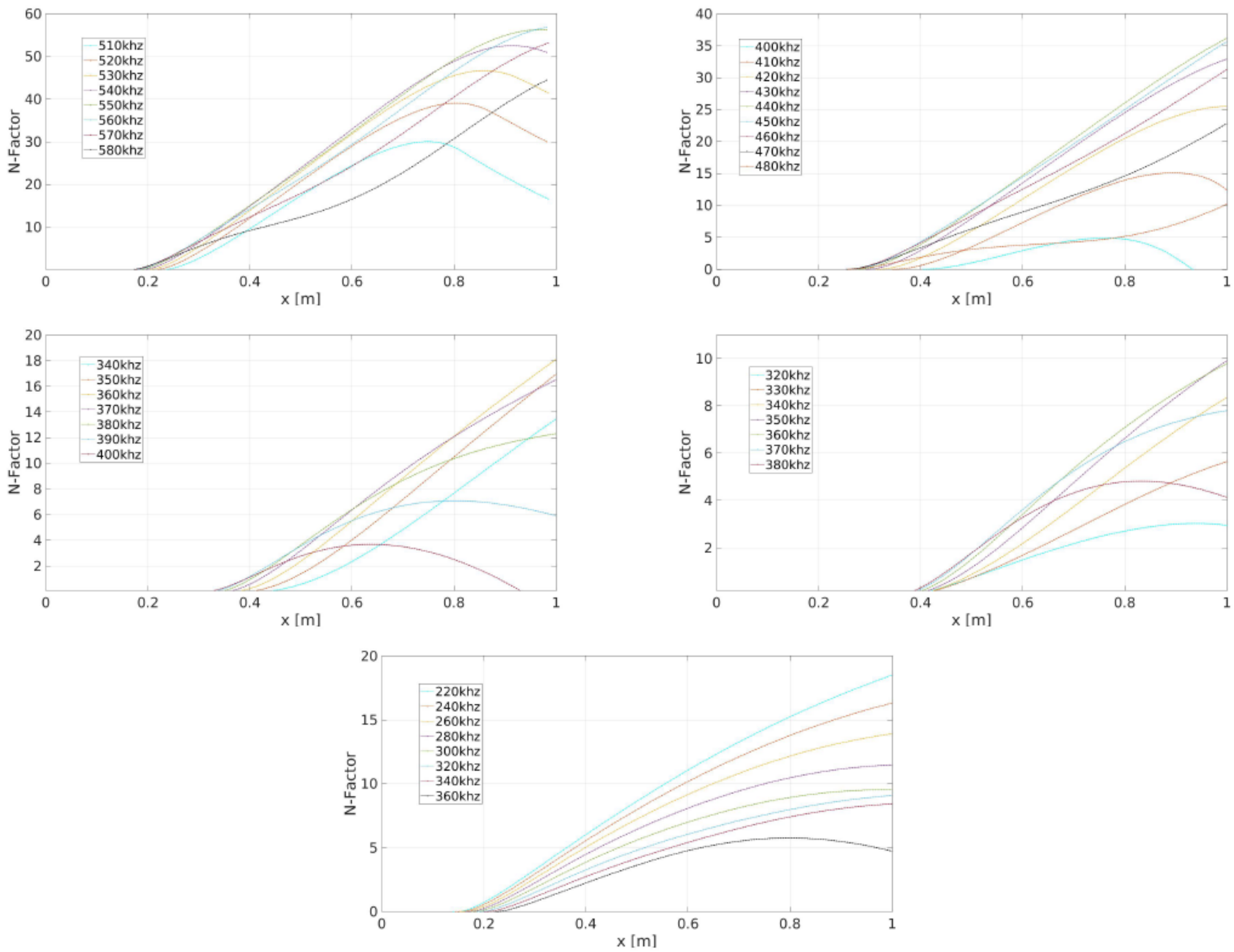

Figure 4.5: LPSE on second modes upper left: 3m flare 300k; upper right: 4m flare 400k; middle left: 5m flare 500k; middle right: 6m flare 600k; lower: 7m flare 700k

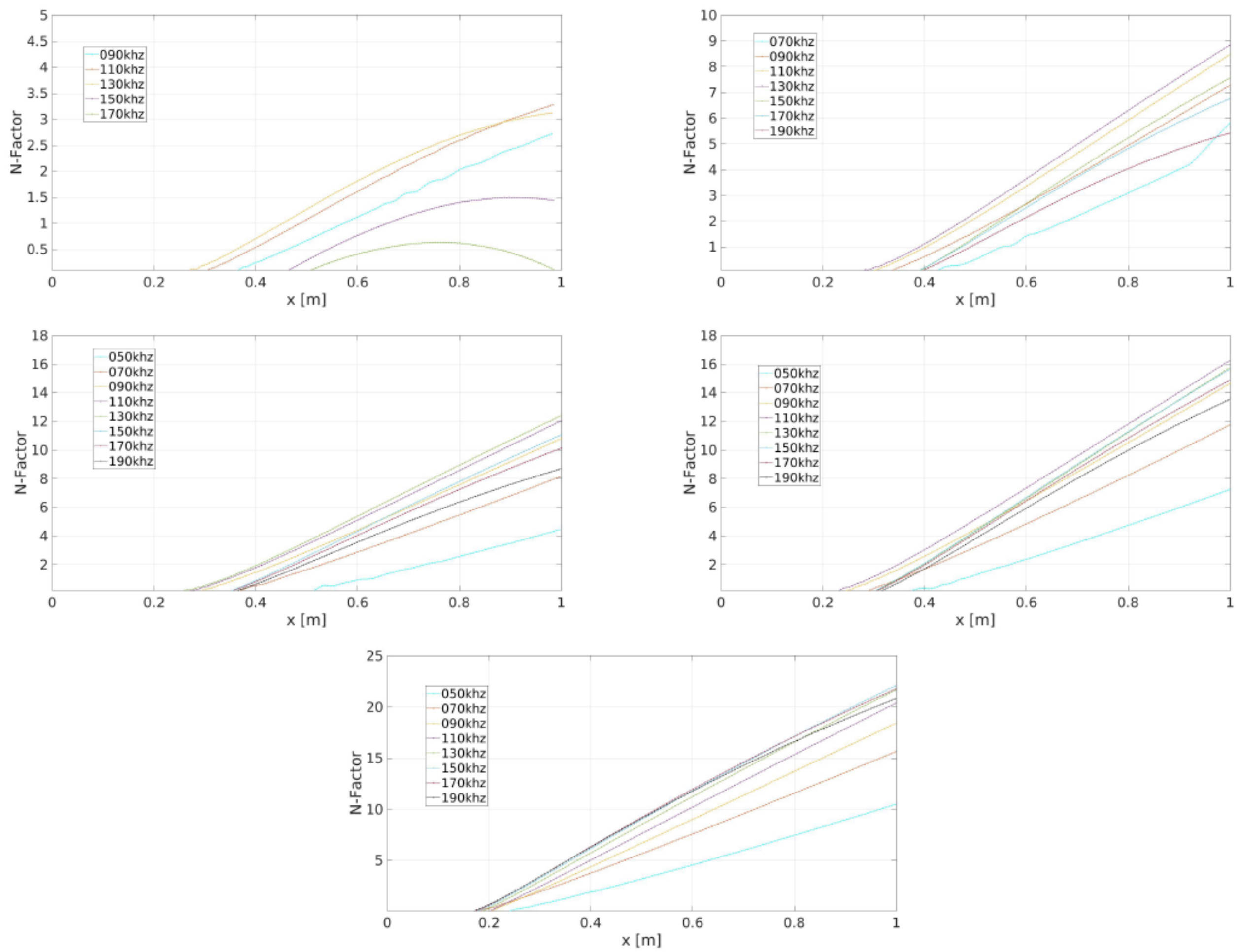

Figure 4.6: LPSE on first modes upper left: 3m flare 300k; upper right: 4m flare 400k; middle left: 5m flare 500k; middle right: 6m flare 600k; lower: 7m flare 700k

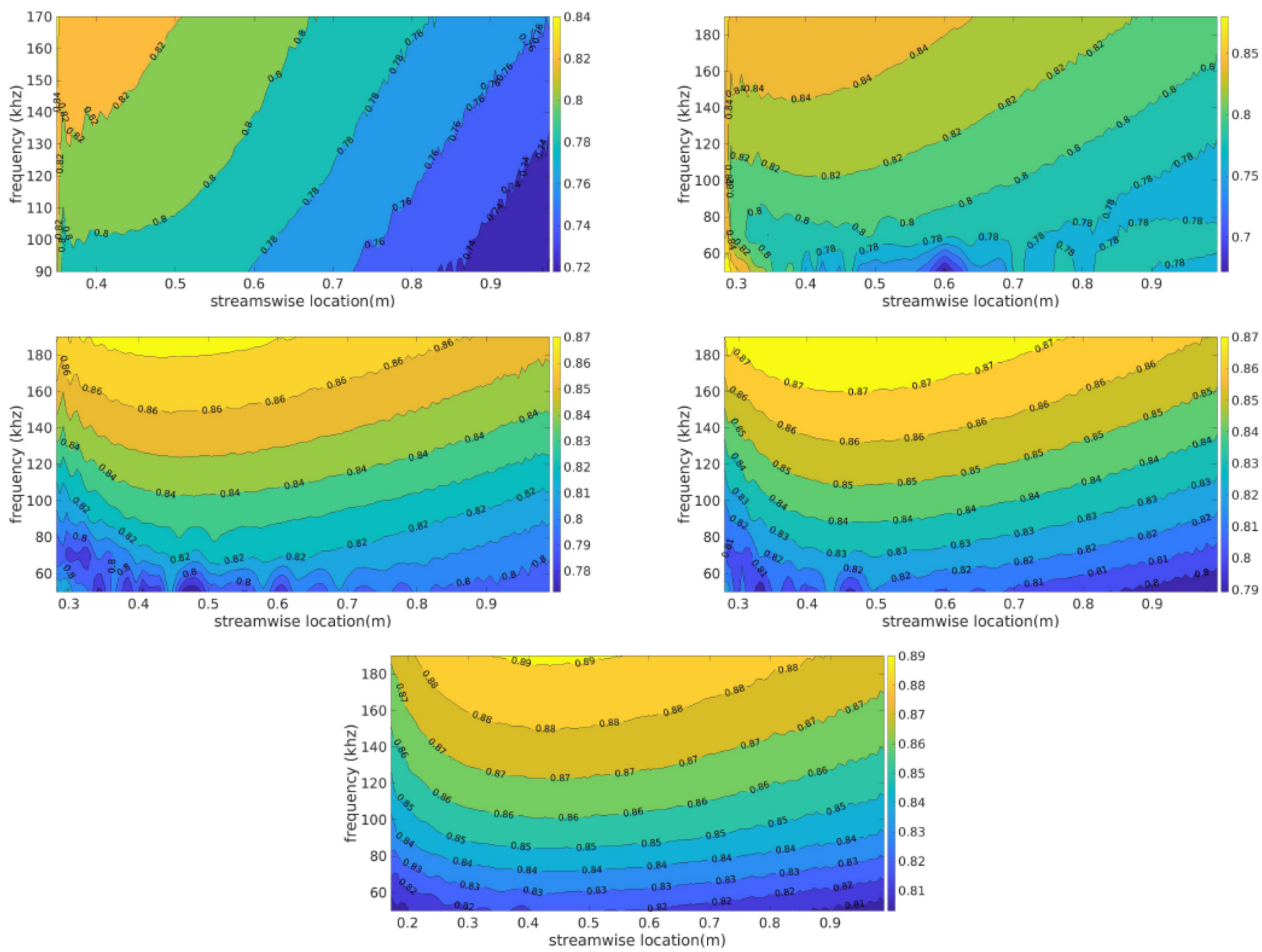

Figure 4.7: Phase speeds of first modes upper left: 3m flare 300k; upper right: 4m flare 400k; middle left: 5m flare 500k; middle right: 6m flare 600k; lower: 7m flare 700k

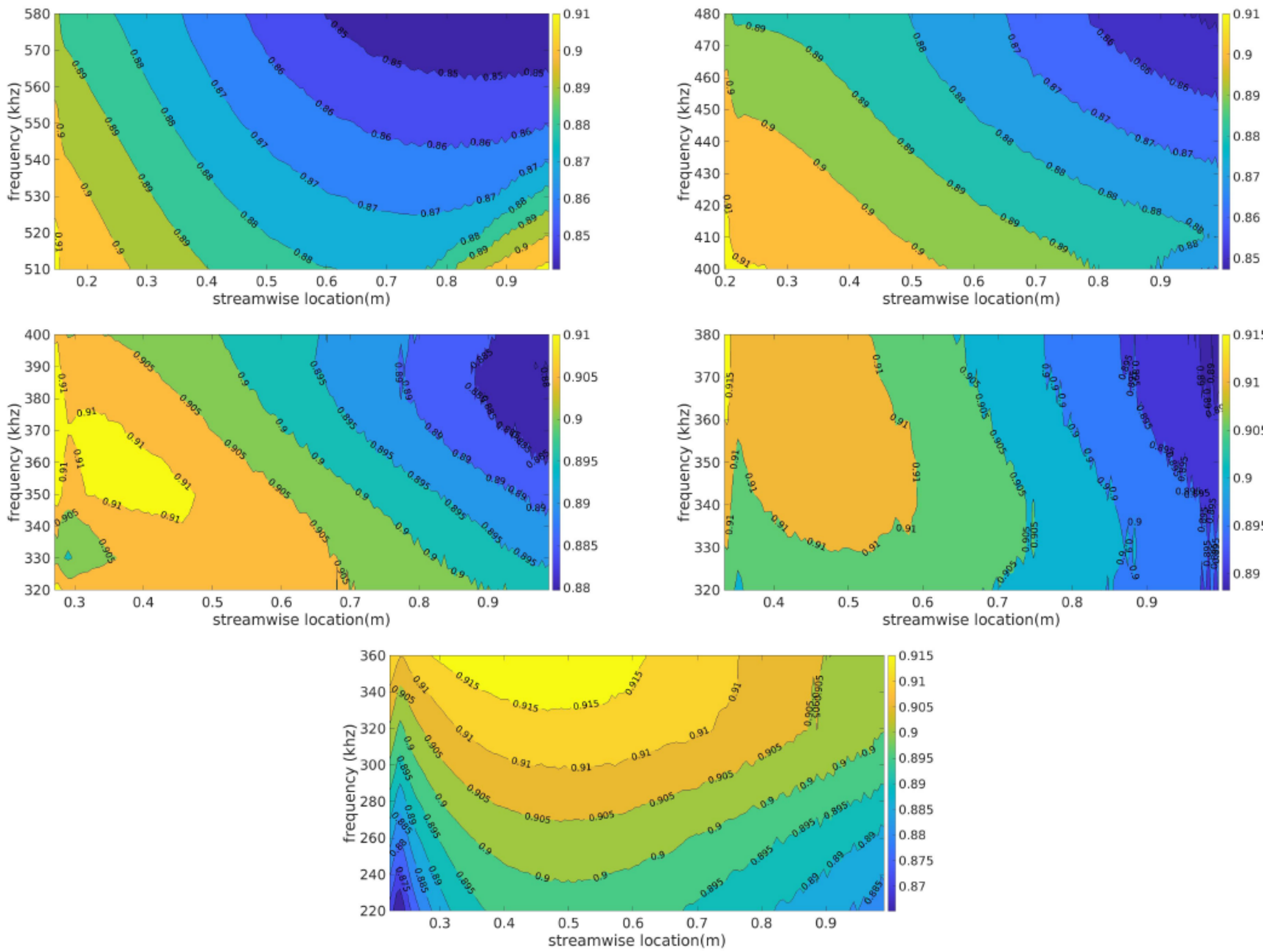

Figure 4.8: Phase speeds of second modes upper left: 3m flare 300k; upper right: 4m flare 400k; middle left: 5m flare 500k; middle right: 6m flare 600k; lower: 7m flare 700k

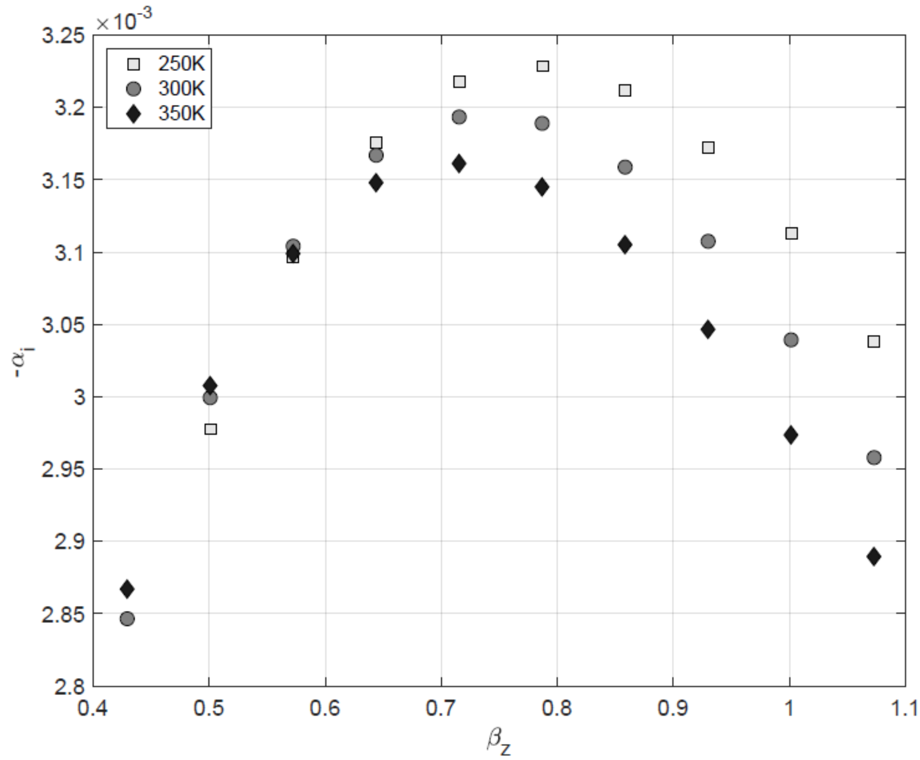

Figure 4.9: Görtler instability modes evaluated at 0.456m streamwise location for the 3m radius are cones at 250K, 300K and 350K wall temperatures.

Chapter 5

ON THE DYNAMICS OF SECOND MODE MODIFIED FIRST MODE INSTABILITY

The following chapter is adapted from [72]

This chapter is to provide insight into the interactions between Mack's acoustic 2nd mode and the lower frequency oblique 1st mode instabilities, as per goal 1 in chapter 4. In particular, the so called "nonlinear detuning" mechanism (Kuehl et al. [14]) will be isolated, in which a nonlinearly evolving 2nd mode instability modifying the mean flow is investigated. How this modification then affects the dynamics of 1st mode instability, which is simultaneously present in the flows, is also studied. This approach allows us to isolate the detuning effect from direct mode-mode interactions, such that the interactions between first and second mode instability can be more thoroughly understood.

5.1 Basic States

It is known that wall heating/cooling and geometry curvature both exhibit a controlling influence over first- and second-mode instability. From Liang et al.[98], a 1.1m long flared cone with 600K wall temperature and 6m flare radius seemed to indicate a good case to study 2nd mode modified 1st modes. The N-factors for both the 1st and 2nd Mack modes are significant but with a 1st mode dominance. This case may provide some valuable insight into how 2nd modes via the mean flow distortion, can affect 1st mode growth. Here, the steady and laminar basic state solutions are calculated utilizing US3D. For this study, the flow parameters similar to the nominal operating conditions of the Mach 5 Ludwig Quiet tunnel at the University of Arizona were utilized.

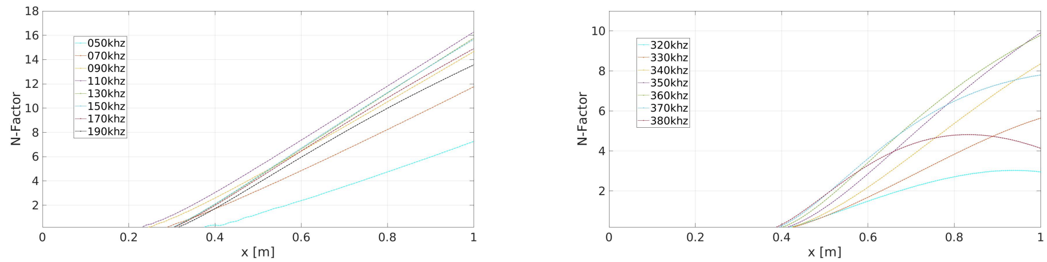

Figure 5.1: LPSE calculations of the 1st (left) and 2nd (right) mode frequencies for a 600K wall temperature 6m flared cone

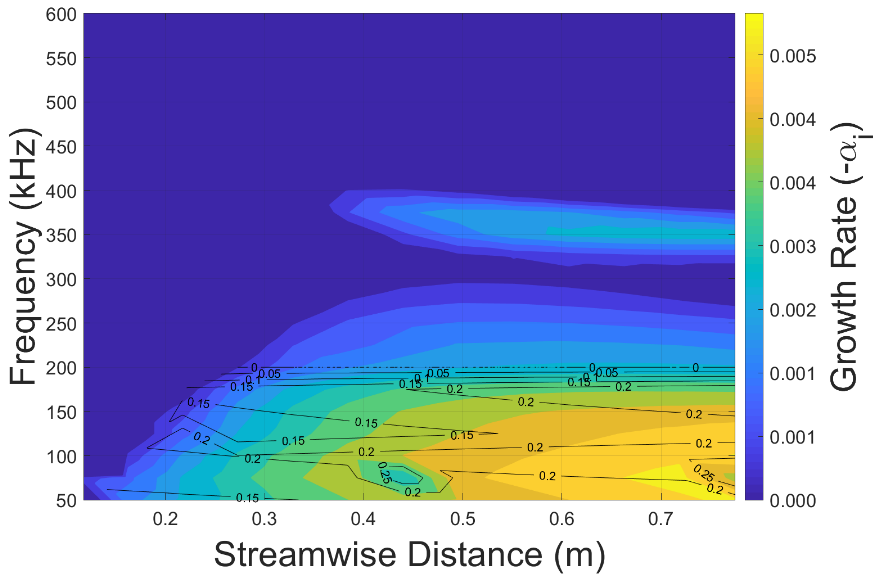

Figure 5.2: LST calculations of the 600K wall temperature 6m flared cone

A 1.1m long cone with a 6m flare radius and a 7 degree opening angle was used. To identify a flared cone as "sharp", a small but finite (≈1mm to allow the model to be physically realized) cone tip radius of 1mm is specified. With the 3D CAD model of the cone, Pointwise was utilized to create the computational domain. This 2D grid is then rotationally extruded 1 degree around the central-axis of the cone to resolve a "slice", which is sufficient as we are considering cones at 0 angle-of-attack (AOA).

M_∞	$\rho_\infty(kg/m^3)$	$T_\infty(K)$	$U_\infty(m/s)$
5	$1.362*10^{-1}$	66.667	818.3337

Table 5.1: Basic state flow conditions

$r_{flare}(m)$	Cone length (m)	Tip radius (m)	Opening angle $(°)$	$T_{wall}(K)$
6	1.1	0.001	7	600

Table 5.2: Geometry parameters

5.2 Methodology

For boundary layer stability, the modal growth interpretation of transition can be generalized: First, with an initial small amplitude disturbance initiated by free stream or boundary imperfections, governed by linear dynamics. Then, as the disturbance amplitude is increased, nonlinear effects become dominant and can lead to spectral broadening and subsequent flow transition. These nonlinear effects are generally referred to as the "nonlinear saturation" mechanisms which involves the loss of energy from the primary modes into the harmonics and mean flow distortion. This energy exchange ultimately focuses on the energy loss to harmonics.

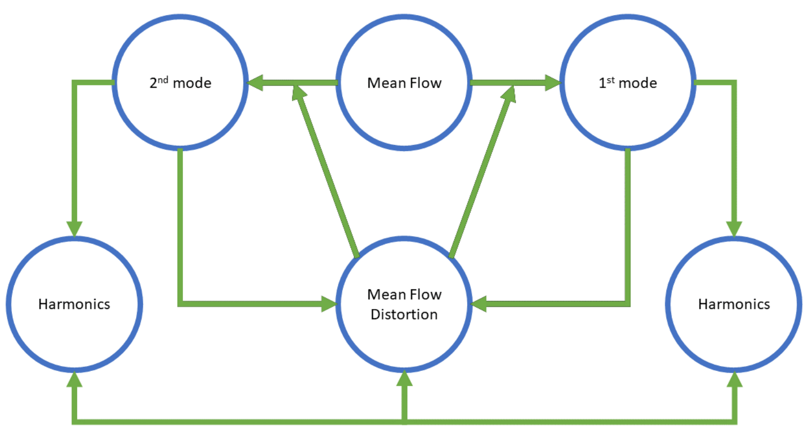

Figure 5.3: A schematic of the energy flow and coupling between the primary Mack modes, harmonics and mean flow distortion. Adapted from Kuehl (2017)[16]

Often in the model growth scenario, the effect of "nonlinear detuning" from

Kuehl et al. [14] is overlooked. That is, as the primary mode instability grows in amplitude, it loses energy to harmonics and also distorts or modifies the mean flow, often accounted for in a nonlinear stability analysis as a mean flow distortion (MFD) mode. This MFD can feedback onto the primary mode disturbance by affecting the energy flow from the basic state into the primary mode. This can be either a negative or positive feedback. For the present study, we consider a basic flow state which is first mode dominated but also contains second mode instability. NPSE analysis is conducted with an increasing amplitudes on the 2nd mode frequencies to analyze its affect on the behavior of the MFD and 1st mode frequencies. In this way, we are able to lay the foundation for future studies where we can isolate and understand a particular aspect of the nonlinear interactions that exists between multiple primary instability modes. This knowledge is then helpful for understanding the full nonlinear interactions between modes.

5.3 Results

5.3.1 NPSE & MFD

The most amplified Mack second modes are determined to be in the region of 350 kHz. NPSE is calculated with this 350 kHz primary second mode along with a 330 kHz and 370 kHz lower and upper side lobes respectively, which lies within the second mode dominated region. The primary first mode is located at 100 kHz. It is noted that for this basic state, there are no direct harmonic interactions between the first and second mode. The initial amplitude of the first mode is kept at 10^8. The second mode amplitudes are varied from 10^5, 10^3, 10^2, 10^1. The top left plot in figure 4 depicts our reference case. A first mode dominated boundary layer with small amplitude second modes. In this case, the 1st mode induced MFD may be self-detuning the 1st mode and affecting second mode growth. A full "perturbed basic state" analysis is required to determine the extent to which these effects are present (analysis to be conducted). However, as the second mode amplitude is increased, the MFD is dominated by second mode growth, which then appears to significantly modulate the 1st mode growth. Thus, this appears to indicate scenario in which energy flows from the second mode to the MFD, which then modulates the base flow to alter first mode growth.

5.3.2 Energetics Analysis

To better understand these nonlinear interactions, the energetics of the 1st mode is evaluated with increasing second mode amplitude $\sim 1m$ downstream from the nose tip. It was recently emphasized by Liang et al. [1] that 1st mode energetics are distinct from TS wave energetics, the former being driven by processes at/near the generalized inflection point while the later is driven by processes at the wall. Details of the energetics derivation can be found in Liang et al. [1], which results in an energy accounting of the disturbance modes of

$$\underbrace{\frac{\bar{\rho}}{2}\frac{\bar{D}\langle\vec{u'}^2\rangle}{Dt}+\frac{\gamma M^2}{2\bar{\rho}c^2}\frac{\bar{D}\langle\vec{P'}^2\rangle}{Dt}}_{\text{dist. energy}}=\langle\underbrace{-\bar{\rho}u'v'\frac{\partial\bar{U}}{dy}-\bar{\rho}v'w'\frac{\partial\bar{W}}{dy}}_{\text{velocity advective}}\underbrace{-\left(\vec{u}'\cdot\vec{\nabla}\right)p'-\gamma M^2P'\left(\vec{\nabla}\cdot\vec{u'}\right)}_{div.\ acst.\ pwr}\rangle. \tag{5.1}$$

where $M^2=\frac{U_e^2}{\gamma RT_e}$, $c=\sqrt{\frac{\gamma P}{\rho}}$, $\gamma=c_p/c_v$, $\mathbf{u}^2=u^2+v^2+w^2$ (with u and v being the streamwise and wall normal components of velocity respectively for the 2D case and w the spanwise velocity component), T is temperature, ρ is density and P is pressure. We have assumed 3D flow that is parallel in the X and Z directions. It should be noted that the energy norm derived here is consistent with the energy norm used in the analysis of compressible turbulence [**?**]. It is also very similar to the Chu energy norm [**?**], if pressure is expanded into density and temperature perturbation quantities, which is very popular in optimal growth studies [**?**].

Note, figure legends have been labeled as follows: UV indicates tradition Reynolds Stress $-\bar{\rho}u'v'\frac{\partial\bar{U}}{dy}$. UDxP, VDyP and WDzP indicate the components of $-\left(\vec{u}'\cdot\vec{\nabla}\right)p'$. PDxU, PDyV and PDzW indicate the components of $-\gamma M^2P'\left(\vec{\nabla}\cdot\vec{u'}\right)$. All DAP indicates the profile of all the divergence of acoustic power terms, with Thermal Total being the integral total, positive indicating an energy source. Advective Total is the integral of the traditional velocity advective Reynolds Stress terms (UV), positive indicating an energy source. Total is the sum of Thermal Total and Advective Total.

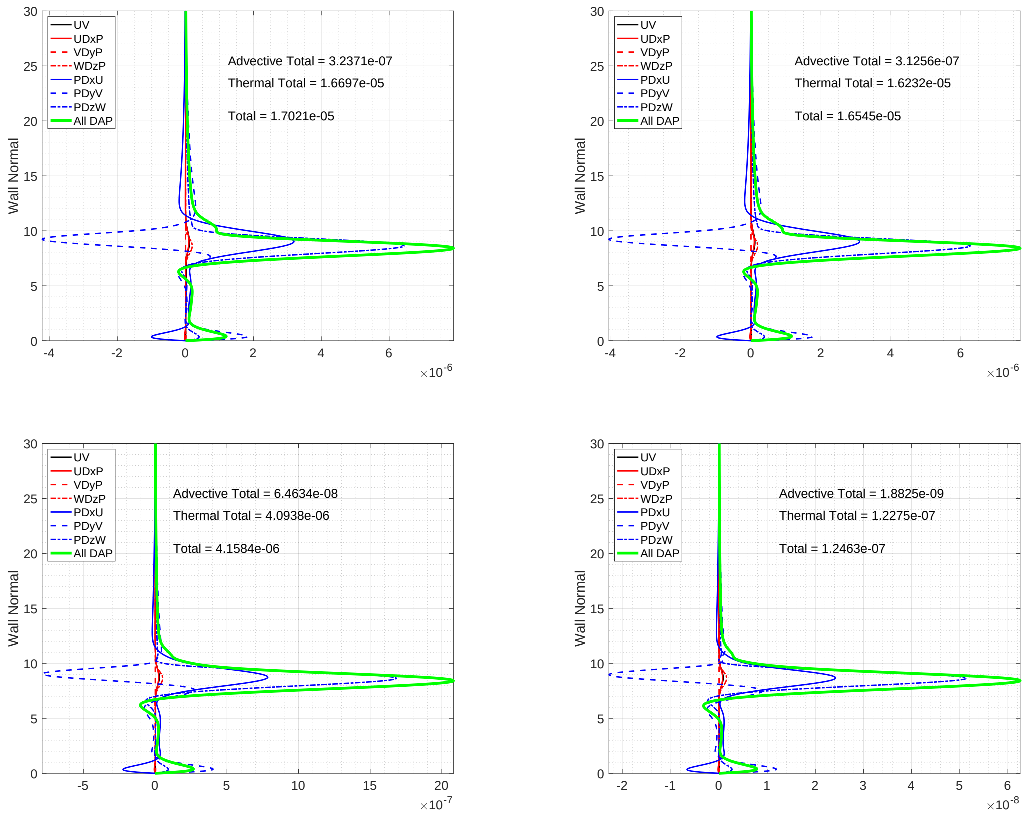

Figure 5.4: 1st mode energetics calculations of the NPSE case with increasing 2nd mode disturbance amplitude. 2nd mode initial amplitudes: Top left: 1e-5; Top right: 1e-3, Bottom left: 1e-2; Bottom right: 1e-1. 1st mode initial amplitude is set to 1e-8 in each case.

As second mode amplitude is increased, the growth of the 1st mode is significantly altered. The specific frequency disturbances involved in these cases, necessitate that this is not due to direct “sum and difference” nonlinear interactions, but instead due to the 2nd mode generated MFD affect on 1st mode evolution. The energetics analysis suggests that the 1st mode growth is driven by $p'\vec{\nabla} \cdot \vec{u'}$, concentrated in the vicinity of the generalized inflection point. While further research is required to confirm, we hypothesize that the MFD has altered the characteristics of the generalized inflection point and hence altered the growth of the 1st mode instability. This scenario is depicted in figure 5.5.

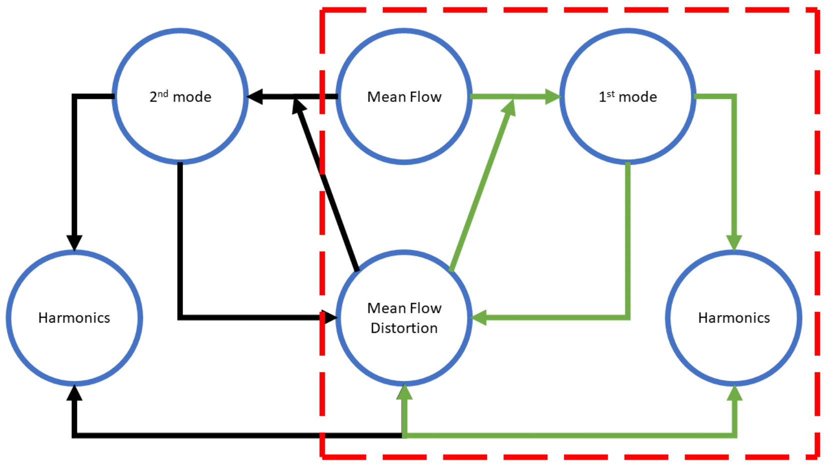

Figure 5.5: A schematic of the energy flow and coupling in a system indicating suppression of 1st mode growth resulted from the 2nd mode induced MFD. Adapted from Kuehl (2017)[16]

5.4 Conclusion

This study demonstrated the nonlinear detuning mechanism likely plays a significant role in the study of multi-mode interactions. A 1.1m, sharp cone with a flare radius of 6m and wall temperature of 600K, at Mach 5 was considered. It was found that the presence of a nonlinear 2nd mode wave can significantly influence the growth of a 1st mode wave, even when direct (i.e. traditional sum and difference) interactions are not present. An energetics analysis was conducted and it was hypothesized that the suppression of 1st mode growth resulted from the 2nd mode induced MFD modification of the generalized inflection point. However, further research is required to confirm this.

Chapter 6

VALIDATION OF POROUS IMPEDANCE BOUNDARY CONDITION FOR A PSE CODE

The following chapter is adapted from [106]

Study of methodologies which delay this transition may allow for the reduction for certain thermal management systems, thereby reducing weight and space, and increasing aerodynamic stability during sustained hypersonic flight. With the understanding that Mack's second mode is a thermoacoustic instability wave trapped within an acoustic impedance well within the boundary [35], methodologies for suppression of this second mode can be investigated. Passive control of boundary layer stability has been investigated both experimentally with porous surfaces of various makes and computationally with the application of impedance boundary conditions. Applications of Carbon- Carbon (C/C) based surfaces for the absorption of 2nd mode instability energy has been employed in previous studies [107, 108, 109, 110, 111, 112, 113]. For this chapter, a numerical study of axisymmetric flow over a sharp straight cone is performed with an impedance boundary condition based on the Homogeneous Absorber Theory (HAT) [114, 110, 113]. Results are compared with existing computational studies of the impedance boundary conditions applied with HAT and the suppression effectiveness of porous surfaces on unstable 2nd modes.

6.1 Basic States & Geometries

For this study, a straight conical geometry with 1m length, 2.5mm tip radius, 7° opening angle with a 300K isothermal wall is utilized. The geometry parameters are based on experiments by Wagner [110] in the DLR High Enthalpy Shock Tunnel Göttingen and computational studies by Sousa [113]; as tabulated in table 6.1. The flow

Cone length (m)	Tip radius (mm)	Opening angle $(°)$	$T_{wall}(K)$
1	2.5	7	300

Table 6.1: Geometry parameters

M_∞	$\rho_\infty(kg/m^3)$	$T_\infty(K)$	$U_\infty(m/s)$
7.4	$2.76 * 10^{-2}$	268	2422

Table 6.2: Basic state flow conditions

condition being studied is a M7.4 flow with $Re = 4.01e6\ m^{-1}$; freestream parameters are reported in table 6.2.

6.2 Boundary Conditions

With state equations assuming the decomposition as shown in equation 2.19, the pressure term can be derived under ideal gas assumptions $p = \rho RT$ such that $p = \bar{\rho}T' + \rho'\bar{T}$. Applying the impedance boundary condition from Sousa[113] where $p' = \rho_0 a_0 Z_*(\omega)v'(\omega)$, the wall boundary conditions becomes:

$$\bar{R}(\bar{\rho}T' + \rho'\bar{T}) - \rho_0 a_0 Z_*(\omega)v'(\omega) = 0 \tag{6.1}$$

where ρ_0 and a_0 are the base density and speed of sound respectively. Z_* is the specific acoustic impedance of the pores [113]. Upon non-dimensionalization the boundary conditions becomes

$$v' = \frac{1}{Z_*\gamma M}\left(\bar{\rho}T' + \rho'\bar{T}\right) \tag{6.2}$$

6.3 Material Parameters

The absorption characteristics of porous materials are dependent on several material parameters [108]. The porosity ϕ, flow resistivity Ξ and structure factor κ are notably important.

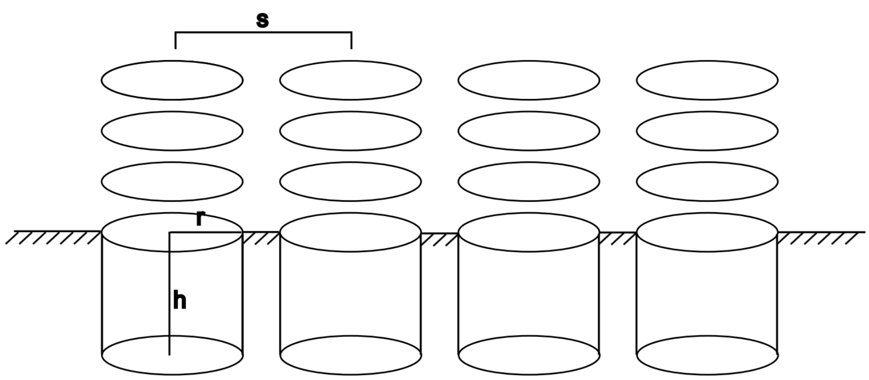

Figure 6.1: Example diagram of pores

6.3.1 Porosity:

The porosity ϕ is defined as a relationship between the volumes of the pore V_{pore} and total volume of the material V_{tot}. If the pore structure can be approximated as a long cylindrical tube, $V_{pore} = \pi r^2 h$. For ordered cylindrical pore patterns, the porosity can be approximated as follows

$$\phi = \frac{V_p}{V_{tot}} \approx \pi \frac{r^2}{s^2} \tag{6.3}$$

where r and s denote the radius of the pore and spacing between pores respectively. The pore aspect ratio can also be defined when given the depth of the pore h as:

$$\text{Aspect Ratio} = \frac{h}{2r} \tag{6.4}$$

6.3.2 Flow Resistivity:

The flow resistivity Ξ ($MPa\frac{s}{m^2}$) describes the effectiveness of the air flow through the material. It can also be denoted as the ratio between the resistivity R_s and thickness of the material (depth of the pore) h [108].

$$\Xi = \frac{R_s}{h} \tag{6.5}$$

The resistivity R_s can be defined as

$$R_s = \frac{p_1 - p_2}{U} \tag{6.6}$$

with p_1 and p_2 being the upstream and downstream pressure of the absorber and U being the velocity at the porous surface. Specific flow resistivity characterizes the ease of which air can enter the material and the resistance it encounters within the porous material, which can give an indication of how well the material absorbs and transmits sound waves.

6.3.3 Structure Factor:

The structure factor κ of a porous material also plays an important role as it describes an approximation of the pore pathway inside the material. This parameter is not measured for randomly structured porous elements but is instead estimated from the acoustic performance of the absorber and gives an indication of how much of the pore's volume is involved in the absorption process [108]. $\kappa = 1$ indicates that the entire volume of the pore is utilized for absorption. However in reality, the structure factor is generally greater than 1 due to inherent material properties and the random microstructure effects. Thus κ and can be defined as the ratio between the accessible pore volume $V_{access} = \phi V_{tot}$ and the pore volume which can be accelerated by acoustic pressure V_{accel} [108].

$$\kappa = \frac{V_{access}}{V_{accel}} \tag{6.7}$$

6.3.4 Breaking Frequency:

The breaking frequency ω_k is generally used as an preliminary identifier of the efficiency of the absorber material and is defined as

$$\omega_k = \frac{\Xi\phi}{\rho_0\kappa} \tag{6.8}$$

where Ξ is the flow resistivity, ϕ is the porosity and ρ_0 is the base density at the wall. Frequencies above the breaking frequency is expected to have "good" absorption characteristics while likewise, frequencies below would be expected to have poor absorption effectiveness [108]. Experimental characterization of these parameters have shown that commonly, porous surface materials must generally have thickness h at least $\frac{1}{10}$ of a wavelength to absorb incident sound. h thickness must also be $\frac{1}{4}$ of a wavelength to completely absorb all sound [115] [116].

It is noted that for sufficiently small pore radius with interactions between neighboring pores being weak, the disturbances caused by longitudinal and transverse waves in the porous layer can be neglected [100]. Generally, pore radius and spacing (and consequently, porosity) are much smaller than the disturbance wavelengths in the boundary layer, which in-turn, is closely related to the boundary layer thickness. It may be possible that larger porosity parameters will start to affect the boundary layer and induce instability mechanisms in the boundary layer associated with high surface roughness and becomes an receptivity problem [100]. It is also noted that the highest absorption occurs furthest from the rear section of the porous surface. Absorption of the lower frequencies are more effective as thickness is increased [115] [116].

6.4 Homogeneous Absorber Theory

From Muller [114], Sousa et al. [113], Wagner et al. [108, 109] the Homogeneous Absorber Theory (HAT) can be utilized to estimate the specific acoustic impedance both experimentally and computationally. The specific acoustic impedance of a finite thickness wall can be estimated utilizing HAT can be defined as a complex function scaled by the theoretical specific acoustic impedance of that of an infinite thickness porous wall Z_∞. It is formulated by Sousa et al.[113] as:

$$Z_{HAT} = \underbrace{\left[\rho_0 a_0 \frac{\sqrt{\kappa}}{\phi}\sqrt{1 - i\frac{\omega_k}{\omega}}\right]}_{Z_\infty} \frac{1 + e^{-2ik_a h}}{1 - e^{-2ik_a h}} \cos\theta_i \tag{6.9}$$

where Z_∞ is the homogeneous porous absorber of infinite wall thickness, κ is the structure factor and ρ_0 and a_0 being the basic state density and speed of sound respectively, ω_k and $\omega = 2\pi f$ being the breaking frequency and angular frequency respectively. The complex absorber wave number k_a is defined as

$$k_a = k\sqrt{\kappa}\sqrt{1 - i\frac{\omega_k}{\omega}} \tag{6.10}$$

Aspect Ratio	Pore Height(mm)	Porosity(ϕ)	$\Xi(MPa{*}s/m^2)$	Structure fac.(κ)	Incidence Angle(θ_i)
25	5	0.15	25.7	8	30°

Table 6.3: Some selected porous wall material properties

The wave number k is defined as the ratio between the angular frequency and phase speed of the wave: $k = \frac{\omega}{c}$. The wave angle effects are taken to account as a correction factor to the specific acoustic impedance. The wave incidence angle θ_i is zero when the direction of the sound wave propagation is normal relative to the absorber surface [113, 114]. For this study, the material parameters including pore aspect ratio, porosity, flow resistivity, structure factor and the incidence angle of sound waves, tabulated in figure 6.3, were selected based on values utilized computationally and experimentally by Sousa et al. [113] and Wagner et al.[109] such that a comparison of data and results between cases can be easily performed.

6.5 LST

To estimate the effects that the impedance has on the stability calculations, the general LST v' boundary condition can be replaced by the boundary condition in equation 6.2. A zero impedance BC is run first to determine the wavenumber k and frequency ω of the unstable mode. These parameters can then be used as inputs into equations 6.9 and 6.10 to estimate Z_*. This is then fed back into the LST process, utilizing the newly calculated Z_*, such that the impedance is now nonzero and a function of k and ω of the unstable mode. This yields an adaptive Z_* that is tuned to the unstable mode at each x-location and frequency. The resulting complex Z_* can then be plotted as a function of streamwise location and frequency as depicted in figure 6.3. Hence these Z_* values from the LST analysis are "locally optimized" for the frequency and unstable mode at each streamwise location.

The impedance boundary condition is applied approximately from 0.182m to 0.950m from the tip of the cone. Impedance results were analysed in comparison to the modeling of the acoustic response of carbon/carbon (C/C) data as seen in figure

11 of Sousa et al.[113]. The calculated Z_* values for the most unstable mode at each frequency is then extracted and plotted in figure 6.4 and compared with the Z_* of C/C as extracted from Sousa et al. There are slight differences in the $Re(Z_*)$, however the specific impedance values from the HAT implementation in JoKHeR appears in better overall Z_* agreement with the reference C/C data than with the reference HAT model employed by Sousa.

The most unstable growth rate of the zero Z impedance case is $\alpha_i = -0.0117$ and the nonzero Z impedance case is $\alpha_i = -0.0095$ at approximately 400khz and 0.8m -0.9m downstream from the nose tip. This reduction in α_i is indicative of an overall suppression of the 2nd mode growth rate of the nonzero Z case in comparison with the zero Z impedance case as depicted in figure 6.2.

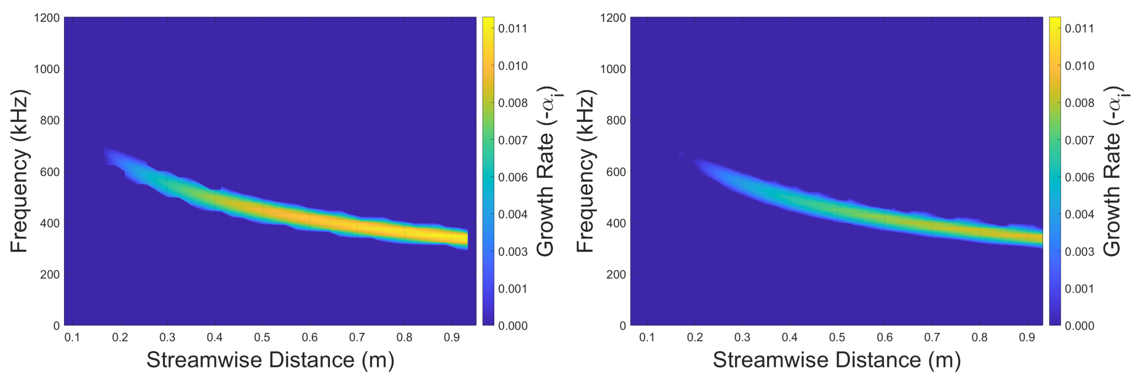

Figure 6.2: Stability diagrams of the base zero Z impedance case (left) and nonzero Z impedance case (right)

6.6 LPSE

An LPSE analysis was also performed on a 400 kHz unstable 2nd mode with its N-factor diagram shown in figure 6.5. The results are then compared to a solid wall case and C/C data extracted from Sousa et al. For the current case, the complex impedance of the most unstable mode at 400khz were determined to be $19.6 - i10.84$ while the reference impedance for C/C is $26 - i9.5$. These impedance values were then applied across the entire length of the cone and marched.

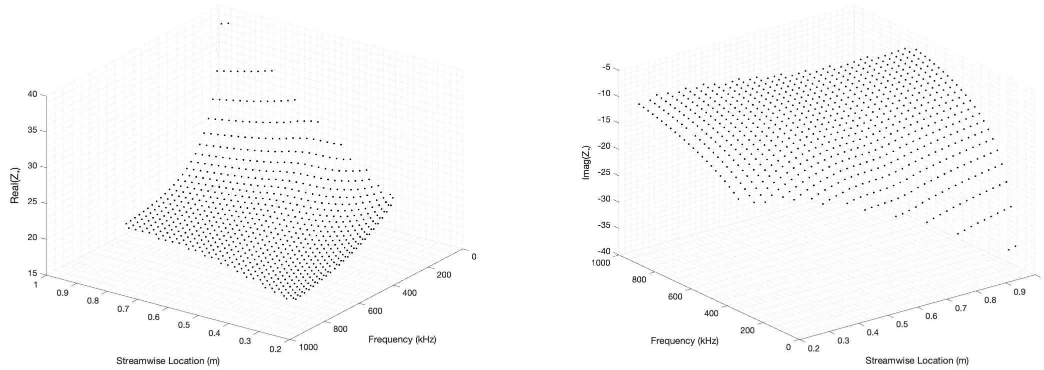

Figure 6.3: Values of Re(Z_*) (left) and Im(Z_*) (right) for a 400kHz unstable 2nd mode

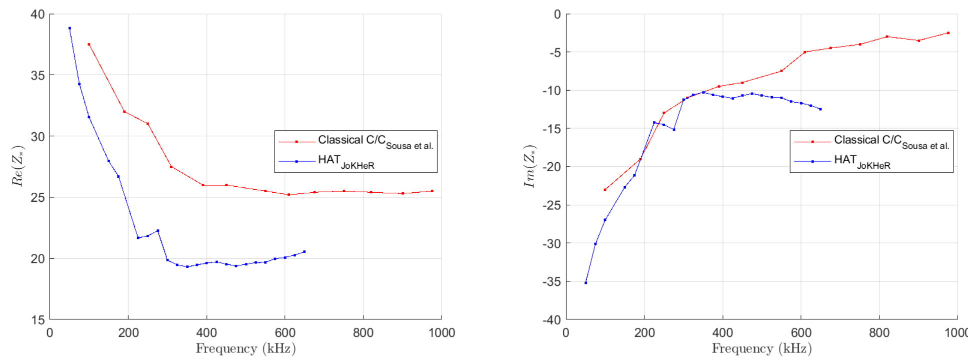

Figure 6.4: Comparison of JoKHeR Z_* and Classical C/C Z_* data from Sousa et al.

Between the solid wall and the current case, there is a noticeable decrease in N-factor with disturbance amplitude being reduced by a factor of around 5.9. This factor of reduction in unstable mode growth appears to be similar to the factor of reduction in the amplitudes of pressure modes at the wall, $||\hat{p}||$, seen in figure 13 of Sousa et. al[113]. Their DNS computations with the impedance boundary conditions applied shows an amplitude reduction factor of about 7.5. This is roughly a $\pm$25% error in comparison our factor of reduction in unstable growth rate. Discrepancies may be due to the slight differences in the initial setup of the basic states and stability calculations, however this percent error is considered acceptable for this preliminary benchmark study. It is also noted that the slight deviations between our estimated Z_* values which consequently yields a 25% error in predicted factor of reductions, can be alluding to the highly sensitive nature of variations in specific impedance values on the dynamics of the unstable modes.

A simple sensitivity study was conducted by calculating 0.75 and 1.25 times that of the current Z_* at 400khz. Also included for comparison is a case using C/C data from Sousa et al. (figure 6.5). Scaling down the impedance appears to significantly decrease the unstable mode growth rate more compared to scaling up. With the solid wall reference case, there is a factor of 4.3, 5.9 and 9.7 decrease in max N-factor amplitude for 1.25x, 1x and 0.75x the current Z_* case respectively. That is, a 25% decrease in impedance appears to yield a greater change in unstable mode growth rate in comparison with the unmodified current Z_* case than with a 25% increase in impedance. This indicates the highly sensitive nature of most unstable 2nd modes to deviations from the current locally optimized Z_*.

6.7 Conclusion

This study demonstrated the ability of PSE codes, particularly JoKHeR, to simulate the application of porous surfaces across conical geometries in an attempt to modify 2nd mode instabilities utilizing impedance boundary conditions formulated by the Homogeneous Absorber Theory. A M=7.4 freestream flow with $Re = 4.01e6\ m^{-1}$ run conditions was applied over a 1m long straight cone with a 2.5mm tip radius at a 7° opening angle. A high sensitivity to the impedance values on unstable 2nd mode growth rate was shown with an LPSE analysis by varying the scaling of the Z_* across the length of the geometry while analyzing its resulting unstable mode growth rate. It is also noted that the JoKHeR implementation of HAT appears to yield impedance values that have a closer agreement with C/C Z_* values than the HAT Z_* calculations from Sousa et al.[113]. Further work will be performed to determine the reasoning behind this discrepancy in results. It is surmised that the energy characteristics of the 2nd mode over porous surfaces will be modified with the new applied wall boundary condition, which can be investigated with an energetics analysis as explored in Kuehl

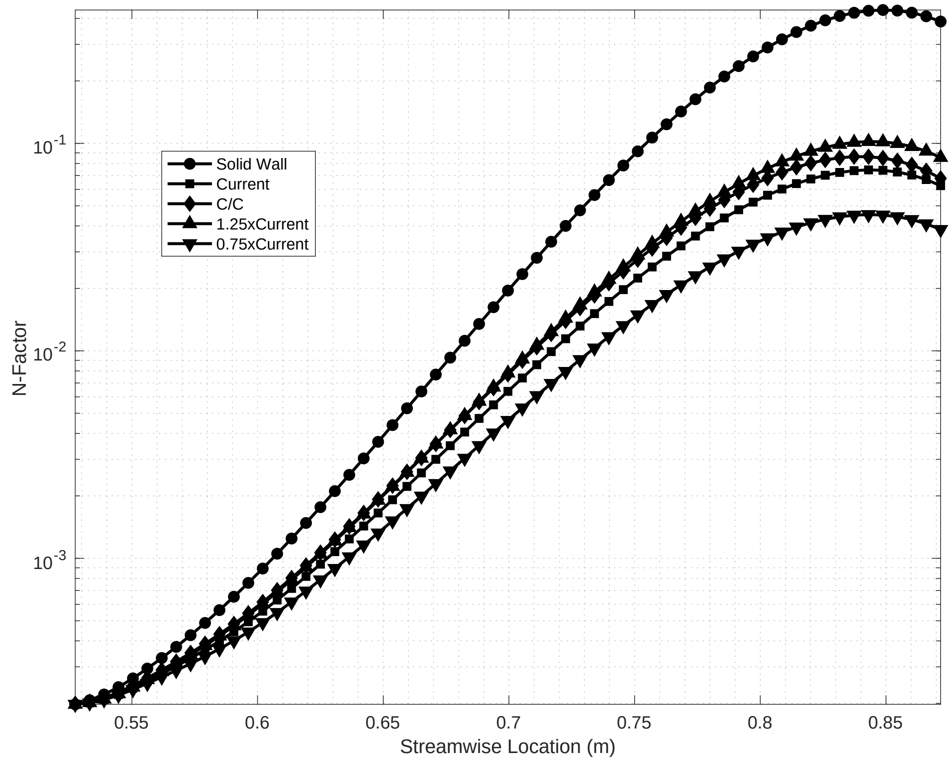

Figure 6.5: LPSE calculations of the solid wall base case (circle), porous wall with current calculated Z_* (square), C/C Z_* values extracted from Sousa et al. (diamond), porous wall with 1.25x current Z_* values (up triangle) and porous wall with 0.75x current Z_* values (down triangle).

(2017)[35] and Liang et al. (2023) [?]. Further work is also needed to examine the effects Z_* on non-primary unstable mode frequencies.

Chapter 7

SUMMARY AND FUTURE WORK

The work performed in this manuscript explored some of the physical mechanisms responsible for hypersonic boundary layer transition. High-speed boundary layer transition is dominated by the modal, exponential amplification of various Mack modes present within the boundary layer. An inviscid energetics analysis was performed and disturbances were classified based on their energetics signature on a Blasius boundary layer for a range of Mach numbers. This approach builds insight into the fundamental mechanisms governing various types of instability. It is shown that first mode instability is distinct from Tollmien–Schlichting instability, being driven by a phase shifting between streamwise velocity and pressure perturbations in the vicinity of the generalized inflection point and insensitive to the viscous no-slip condition. Further, it is suggested that the obliqueness of the first mode is associated with an inviscid flow invariant.

In order to study the first-mode – second-mode interactions in hypersonic boundary layers, a design investigation of Mach 5 flared cones was done with the goal to study three cases, restated here from chapter 4 as:

1. The dynamics of a first-mode instability in a second-mode dominated boundary layer.
2. The dynamics of a second-mode instability in a first-mode dominated boundary layer.
3. The transitional dynamics of a boundary layer in which the first- and second-mode instability mechanisms interact.

Via linear stability analysis (LST, LPSE) it was determined that a 5m-500K flared cone design is a good candidate for goal 1; a 6m-600K flared cone is a good candidate for goal 2; a 7m-700K flared cone design can be used to partially study goal 3. However, for goal 3, direct interaction between first- and second-modes via phase locking is unlikely and ultimately the transitional dynamics will be first-mode dominated. Thus, goal 3 requires further revision. Though, it does allow for numerical study of interactions between the viscous and acoustic mechanisms responsible for generating first- and second-mode instability. Finally, it was noted that increased wall temperature has the effect to dampen Goı̈tler instability in the cases studied.

With the understanding of the geometric requirements for 1st – 2nd mode interactions, a 1.1m long, 600K wall temperature flared cone (6m flare radius) at Arizona M5 conditions was then considered for the next phase of analysis. The focus of this study is to investigate the nonlinear interactions within hypersonic boundary layers with the coexistence of Mack's 1st and 2nd modes, with emphasis on goal 1. Specifically, emphasis is placed on the interactions and energetics of the 1st mode, MFD and the 2nd mode. It is found that as 2nd mode amplitudes are increased, the MFD significantly alters the 1st mode growth, indicating that the increased MFD from the 2nd mode disrupts energy flow from the mean flow to the 1st mode.

A study was performed where an impedance boundary condition IBC with formulation utilizing the HAT)was applied on to a PSE code and compared it to similar numerical computations. Specifically, a benchmark study is performed to validate the implementation of the impedance BC on the JoKHeR stability package and its ability to investigate the sensitivity of unstable modes to a scaled wall impedance. It is found that the JoKHeR implementation of the IBC predicts a factor of reduction in maximum unstable growth rate with 25 percent error compared to the implementation of the IBC and DNS analysis by Sousa et al. The high sensitivity of unstable mode growth rate to changes in the specific impedance is also found, as a 25 percent decrease in impedance appears to yield a greater change in modal growth in comparison with a 25 percent increase in impedance.

7.1 Works Completed to Date

The following works [98, 1, 72, 106] have been completed to date in an attempt to partially answer the aforementioned research questions respectively. Other open problems in hypersonics such as entropy layer effects on crossflow instabilities, nose blunteness effects on crossflow instabilities and the energy redistribution for NPSE methods were investigated in [46, 117, 118].

7.2 Future work

Further work is required to investigate goals 1 and 3. More validation of the suppression of mode growth via multi-mode induced MFD modification as seen in chapter 5 is also required. Studies into other mode interactions with the 1st and 2nd modes can be performed such as with crossflow and Goörtler modes to further understand the interaction and dynamics of competing instability modes in hypersonic boundary layers. Application of the IBC onto other relevant geometries is also of interest, such as onto the walls of a hypersonic wind tunnel nozzles to investigate the mitigation of 2nd mode instabilities in regions of transition to reduce flow contamination.

BIBLIOGRAPHY

[1] Tony Liang, Sulav Kafle, Arham Amin Khan, Pedro Paredes, and Joseph Kuehl. On the inviscid energetics of mack's first mode instability. *Theoretical and Computational Fluid Dynamics*, pages 1–15, 2022.

[2] J. D. Anderson Jr. *Fundamentals of Aerodynamics*. McGraw-Hill, 5th edition edition, 2011.

[3] Ernst Heinrich Hirschel et al. Basics of aerothermodynamics. 2005.

[4] John David Anderson. *Modern compressible flow: with historical perspective*, volume 12. McGraw-Hill New York, 1990.

[5] Thomas L Lewis and Richard D Banner. Boundary layer transition detection on the x-15 vertical fin using surface-pressure-fluctuation measurements. Technical report, 1971.

[6] F.M. White. *Viscous Fluid Flow*. McGraw-Hill international edition. McGraw-Hill, 2006.

[7] MV Morkovin. Transition in open flow systems-a reassessment. *Bull. Am. Phys. Soc.*, 39:1882, 1994.

[8] P. J. Schmid and D. S. Henningson. *Stability and Transition in Shear Flows*, volume 142. Springer, Applied Mathematical Science, 6th edition edition, 2001.

[9] Leslie M Mack. Boundary-layer linear stability theory. Technical report, California Inst of Tech Pasadena Jet Propulsion Lab, 1984.

[10] FT Smith. On the first-mode instability in subsonic, supersonic or hypersonic boundary layers. *Journal of Fluid Mechanics*, 198:127–153, 1989.

[11] William S Saric, Helen L Reed, and Edward B White. Stability and transition of three-dimensional boundary layers. *Annual review of fluid mechanics*, 35(1):413–440, 2003.

[12] William S Saric. Görtler vortices. *Annual Review of Fluid Mechanics*, 26(1):379–409, 1994.

[13] Matthew P Juniper, Ardeshir Hanifi, and Vassilios Theofilis. Modal stability theory: lecture notes from the flow-nordita summer school on advanced instability methods for complex flows, stockholm, sweden, 2013. *Applied Mechanics Reviews*, 66(2):024804, 2014.

[14] Joseph Kuehl. Nonlinear saturation versus nonlinear detuning: Quantification on a mach 6 flared cone. In *55th AIAA Aerospace Sciences Meeting*, page 0763, 2017.

[15] Brandon C Chynoweth, Steven P Schneider, Christoph Hader, Hermann Fasel, Armani Batista, Joseph Kuehl, Thomas J Juliano, and Bradley M Wheaton. History and progress of boundary-layer transition on a mach-6 flared cone. *Journal of Spacecraft and Rockets*, 56(2):333–346, 2019.

[16] J. Kuehl. Nonlinear saturation versus nonlinear detuning: Quantification on a mach 6 flared cone. *AIAA Paper 2017-0763*, 2017.

[17] NASA. *NASA's First 50 Years: Historical Perspectives; NASA 50 Anniversary Proceedings*. NASA, Washington, D.C., 2008.

[18] J. D. Anderson Jr. *Hypersonic and High-Temperature Gas Dynamics*. AIAA Education Series, 2nd edition edition, 2006.

[19] Lord Rayleigh. On the Stability, or Instability, of certain Fluid Motions. *Proceedings of the London Mathematical Society*, s1-11(1):57–72, 11 1879.

[20] Leslie M Mack. Early history of compressible linear stability theory. In *Laminar-Turbulent Transition: IUTAM Symposium, Sedona/AZ September 13–17, 1999*, pages 9–34. Springer, 2000.

[21] Lester Lees and Chia-Chiao Lin. *Investigation of the stability of the laminar boundary layer in a compressible fluid*. Number 1115. National Advisory Committee for Aeronautics, 1946.

[22] F Bertolotti. Compressible boundary layer stability analyzed with the pse equations. In *22nd Fluid Dynamics, Plasma Dynamics and Lasers Conference*, page 1637, 1991.

[23] M Gaster. On the effects of boundary-layer growth on flow stability. *Journal of Fluid Mechanics*, 66(3):465–480, 1974.

[24] Mujeeb R Malik. Hypersonic flight transition data analysis using parabolized stability equations with chemistry effects. *Journal of Spacecraft and Rockets*, 40(3):332–344, 2003.

[25] P.J. Schmid and D.S. Henningson. *Stability and Transition in Shear Flows*. Applied Mathematical Sciences. Springer New York, 2000.

[26] T. Herbert and F. P. Bertolotti. Stability analysis of nonparallel boundary layers. *Bulletin of American Physical Society 32*, 2079, 1987.

[27] Helen L Reed, William S Saric, and Daniel Arnal. Linear stability theory applied to boundary layers. *Annual review of fluid mechanics*, 28(1):389–428, 1996.

[28] Alexander Fedorov. Transition and stability of high-speed boundary layers. *Annual review of fluid mechanics*, 43:79–95, 2011.

[29] Hermann F Fasel, Jayahar Sivasubramanian, and Andreas Laible. Numerical investigation of transition in a flared cone boundary layer at mach 6. *Procedia IUTAM*, 14:26–35, 2015.

[30] William S Saric, Eli Reshotko, and Daniel Arnal. Hypersonic laminar-turbulent transition. *AGARD ADVISORY REPORT AGARD AR*, 2:2–2, 1998.

[31] Anatoli Tumin, Xiaowen Wang, and Xiaolin Zhong. Direct numerical simulation and the theory of receptivity in a hypersonic boundary layer. *Physics of Fluids*, 19(1):014101, 2007.

[32] Xiaolin Zhong and Xiaowen Wang. Direct numerical simulation on the receptivity, instability, and transition of hypersonic boundary layers. *Annual Review of Fluid Mechanics*, 44:527–561, 2012.

[33] Steven P Schneider. Hypersonic laminar–turbulent transition on circular cones and scramjet forebodies. *Progress in Aerospace Sciences*, 40(1-2):1–50, 2004.

[34] Thomas J Juliano, Steven P Schneider, Selin Aradag, and Doyle Knight. Quiet-flow ludwieg tube for hypersonic transition research. *AIAA journal*, 46(7):1757–1763, 2008.

[35] Joseph J Kuehl. Thermoacoustic interpretation of second-mode instability. *AIAA Journal*, 56(9):3585–3592, 2018.

[36] Ponnampalam Balakumar and Lewis Owens. Stability of hypersonic boundary layers on a cone at an angle of attack. In *40th Fluid Dynamics Conference and Exhibit*, page 4718, 2010.

[37] Graham V Candler, Heath B Johnson, Ioannis Nompelis, Vladimyr M Gidzak, Pramod K Subbareddy, and Michael Barnhardt. Development of the us3d code for advanced compressible and reacting flow simulations. In *53rd AIAA Aerospace Sciences Meeting*, page 1893, 2015.

[38] Pedro Paredes, Meelan M Choudhari, Fei Li, Joseph S Jewell, Roger L Kimmel, Eric C Marineau, and Guillaume Grossir. Nose-tip bluntness effects on transition at hypersonic speeds. *Journal of Spacecraft and Rockets*, 56(2):369–387, 2019.

[39] Joseph J Kuehl. Discrete-and finite-bandwidth-frequency distributions in nonlinear stability applications. *Physics of Fluids*, 29(2):024101, 2017.

[40] Helen L Reed, Eduardo Perez, Joseph Kuehl, Travis Kocian, and Nicholas Oliviero. Verification and validation issues in hypersonic stability and transition prediction. *Journal of Spacecraft and Rockets*, 52(1):29–37, 2015.

[41] William S Saric, Helen L Reed, and Edward J Kerschen. Boundary-layer receptivity to freestream disturbances. *Annual review of fluid mechanics*, 34:291, 2002.

[42] L. M. Mack. Boundary-layer stability theory. *Jet Propulsion Laboratory, Pasadena, CA.*, 900-277 Rev. A, 1969.

[43] W.S. Saric. *Hydrodynamic Stability.* Unpublished Manuscript, v.4.2 2010.

[44] L. M. Mack. Boundary-layer linear stability theory. *AGARD Report 709*, 1984.

[45] Armani Batista and Joseph J Kuehl. Local wall temperature effects on the second-mode instability. *Journal of Spacecraft and Rockets*, 57(3):580–595, 2020.

[46] Arham Amin Khan, Tony Liang, and Joseph Kuehl. Entropy layer modification of crossflow instability on yawed blunt cones. In *AIAA AVIATION 2021 FORUM*, page 2888, 2021.

[47] Brandon C Chynoweth. *A new roughness array for controlling the nonlinear breakdown of second-mode waves at Mach 6.* PhD thesis, Purdue University, 2015.

[48] Ioannis Nompelis, Travis Drayna, and Graham Candler. Development of a hybrid unstructured implicit solver for the simulation of reacting flows over complex geometries. In *34th AIAA Fluid Dynamics Conference and Exhibit*, page 2227.

[49] G. V. Candler, H. B. Johnson, I. Nompelis, P. K. Subbareddy, T. W. Drayna, V. Gidzak, and M. D. Barnhardt. Development of the us3d code for advanced compressible and reacting flow simulations. *AIAA Paper 2015-1893*, 2015.

[50] Joseph Kuehl, Eduardo Perez, and Helen Reed. Jokher: Npse simulations of hypersonic crossflow instability. In *50th AIAA Aerospace Sciences Meeting including the New Horizons Forum and Aerospace Exposition*, page 921, 2012.

[51] Alexander Fedorov and Anatoli Tumin. Initial-value problem for hypersonic boundary-layer flows. *AIAA journal*, 41(3):379–389, 2003.

[52] L Håkan Gustavsson. Initial-value problem for boundary layer flows. *The Physics of Fluids*, 22(9):1602–1605, 1979.

[53] Eric Forgoston and Anatoli Tumin. Initial-value problem for three-dimensional disturbances in a compressible boundary layer. *Physics of fluids*, 17(8), 2005.

[54] William O Criminale, Thomas Luther Jackson, and Ronald Douglas Joslin. *Theory and computation in hydrodynamic stability*. Cambridge University Press, 2018.

[55] M. Gaster. On the effects of boundary-layer growth on flow stability. *Journal of Fluid Mechanics*, 66(3):465–480, 1974.

[56] Thorwald Herbert. Parabolized stability equations. *Annual Review of Fluid Mechanics*, 29(1):245–283, 1997.

[57] Chau-Lyan Chang, Mujeeb Malik, Gordon Erlebacher, and M Hussaini. Compressible stability of growing boundary layers using parabolized stability equations. In *22nd Fluid Dynamics, Plasma Dynamics and Lasers Conference*, page 1636, 1991.

[58] R. D. Joslin, C. L. Streett, and C. L. Chang. 3-d incompressible spatial direct numerical simulation code validation study: A comparison with linear stability and parabolic stability equation theories in boundary-layer transition on a flat plate. *Report No. NASA TP-3205*, 1992.

[59] F. Li and M. R. Malik. On the nature of pse approximation. *Theoretical Computational Fluid Dynamics*, 8:253–273, 1996.

[60] M. Gaster. Simulation of swept-wing vortices using nonlinear parabolized stability equations. *Journal of Fluid Mechanics*, 405(3):325–349, 2000.

[61] G. Stuckert and H. Reed. Linear disturbances in hypersonic, chemically reacting shock layer. *AIAA Journal*, 32(7):1384–1393, 1994.

[62] C. L. Chang, H. Vinh, and M. R. Malik. Hypersonic boundary-layer stability with chemical reactions using pse. *AIAA Paper No. 97-2012*, 1997.

[63] H. B. Johnson, T. G. Seipp, and G. V. Candler. Numerical study of hypersonic reacting boundary layer transition on cones. *Physics of Fluids*, 10(10):2676–2685, 1998.

[64] M. R. Malik. Hypersonic flight transition data analysis using parabolized stability equations with chemistry effects. *Journal of Spacecraft and Rockets*, 40(3):332–344, 2003.

[65] C. L. Chang. The langley stability and transition analysis code (lastrac) version 1.2 user manual. *Report No. NASA/TM-2004-213233*, 2004.

[66] H. B. Johnson and G. V. Candler. Hypersonic boundary layer stability analysis using pse-chem. *AIAA Paper 2005-5023*, 2005.

[67] F. Li, M. Choudhari, C. L. Chang, and J. White. Analysis of instabilities in non-axisymmetric hypersonic boundary layers over cones. *10th AIAA/ASME Joint Thermophysics and Heat Transfer Conference*, 2010.

[68] Vassilios Theofilis. Global linear instability. *Annual Review of Fluid Mechanics*, 43:319–352, 2011.

[69] P. Paredes, V. Theofilis, D. Rodriguez, and J. A. Tendero. The pse-3d instability analysis methodology for flows depending strongly on two and weakly on the third spatial dimension. *AIAA Paper 2011-3752*, 2011.

[70] T. Kocian, E. Perez, N. Oliviero, J. Kuehl, and H. Reed. Hypersonic stability analysis of a flared cone. *AIAA Paper 2013-0667*, 2013.

[71] Eduardo Perez, Helen L Reed, and Joseph Kuehl. Instabilities on a hypersonic yawed straight cone. In *43rd AIAA Fluid Dynamics Conference*, page 2879, 2013.

[72] Tony Liang, Arham Amin Khan, and Joseph Kuehl. On the dynamics of second mode modified first mode instability. In *AIAA SCITECH 2023 Forum*, page 0870, 2023.

[73] J. J. Kuehl. Discrete- and finite-bandwidth-frequency distributions in nonlinear stability applications. *Physics of Fluids*, 29:024101–1–024101–8, 2017, 2017.

[74] J. Kuehl, H. Reed, T. Kocian, and N. Oliviero. Bandwidth effects on mack-mode instability. *AIAA Paper 2014-2777*, 2014.

[75] John P Boyd. *Chebyshev and Fourier spectral methods*. Courier Corporation, 2001.

[76] Paul T Dawkins, Steven R Dunbar, and Rod W Douglass. The origin and nature of spurious eigenvalues in the spectral tau method. *Journal of Computational Physics*, 147(2):441–462, 1998.

[77] David Bourne. Hydrodynamic stability, the chebyshev tau method and spurious eigenvalues. *Continuum Mechanics and Thermodynamics*, 15:571–579, 2003.

[78] David R Gardner, Steven A Trogdon, and Rod W Douglass. A modified tau spectral method that eliminates spurious eigenvalues. *Journal of Computational Physics*, 80(1):137–167, 1989.

[79] Yousef Saad. *Numerical methods for large eigenvalue problems: revised edition*. SIAM, 2011.

[80] Lawrence R Rabiner and Bernard Gold. Theory and application of digital signal processing. *Englewood Cliffs: Prentice-Hall*, 1975.

[81] Eric W. Weisstein. Cross-correlation. MathWorld–A Wolfram Web Resource, 2002.

[82] J. A. Masad and R. Abid. On transition in supersonic and hypersonic boundary layers. *International Journal of Engineering Science*, 33(13):1893–1919, 1995.

[83] Lindsay Kirk and Graham Candler. Geometric effects on the amplification of first mode instability waves. In *51st AIAA Aerospace Sciences Meeting including the New Horizons Forum and Aerospace Exposition*, page 261, 2013.

[84] F. T. Smith. On the first-mode instability in subsonic, supersonic or hypersonic boundary layers. *Journal of Fluid Mechanics*, 198:127–153, 1989.

[85] A Fedorov and A Tumin. High-speed boundary-layer instability: Old terminology and a new framework. *AIAA Journal*, 49(8):1647–1657, 2011.

[86] Alexander Fedorov. Transition and stability of high-speed boundary layers. *Annual Review of Fluid Mechanics*, 43:79–95, 2011.

[87] Ming Dong, Yinhui Liu, and Xuesong Wu. Receptivity of inviscid modes in supersonic boundary layers due to scattering of free-stream sound by localised wall roughness. *Journal of Fluid Mechanics*, 896(A23):doi:10.1017/jfm.2020.358, 2020.

[88] Ming Dong and Lei Zhao. An asymptotic theory of the roughness impact on inviscid mack modes in super/hypersonic boundary layers. *Journal of Fluid Mechanics*, 913(A22):doi:10.1017/jfm.2020.1146, 2021.

[89] G. K. Batchelor. *An Introduction to Fluid Dynamics*. Cambridge University Press, 1967.

[90] F. Nicoud and T. Poinsot. Thermoacoustic instabilities: Should the rayleigh criterion be extended to include entropy changes? *Combustion and Flame*, 142:153–159, 2005.

[91] Ankita Mittal and Sharath S Girimaji. Mathematical framework for analysis of internal energy dynamics and spectral distribution in compressible turbulent flows. *Physical Review*, 4(4):042601, https://doi.org/10.1103/PhysRevFluids.4.042601 2019.

[92] B.T. Chu. On the energy tranfer to small disturbances in fluid flow (part 1),. *Acta Mechanica*, 1(3):215, 1965.

[93] Ethan A. Vogel and James G. Coder. A novel entropy normalization scheme for characterization of highly compressible flows. *Theoretical and Computational Fluid Dynamics*, 36:641–670, 2022.

[94] Frank M. White. *Viscous Fluid Flow*. McGraw-Hill Education, 1991.

[95] David F. Rogers. *Laminar Flow Analysis*. Cambridge University Press, 1992.

[96] P. G. Drazin and W. H. Reed. *Hydrodynamic Stability*. Cambridge University Press, second edition edition, 2004.

[97] J. Kuehl. Thermoacoustic interpretation of second-mode instability. *AIAA Journal*, 56(9):3585–3592, 2018, doi:https://doi.org/10.2514/1.J057015.

[98] Tony Liang, Arham A Khan, and Joseph Kuehl. Design of a mach 5 flared cone for first-, second-mode mechanisms interactions. In *AIAA Scitech 2021 Forum*, page 1853, 2021.

[99] Heath Johnson, Chris Alba, Graham Candler, Matthew MacLean, Timothy Wadhams, and Michael Holden. Boundary-layer stability analysis of the hypersonic international flight research transition experiments. *Journal of Spacecraft and Rockets*, 45(2):228–236, 2008.

[100] Alexander V. Fedorov, Norman D. Malmuth, Adam Rasheed, and Hans G. Hornung. Stabilization of hypersonic boundary layers by porous coatings. *AIAA Journal*, 39(4):605–610, 2001.

[101] K Stetson. Nosetip bluntness effects on cone frustum boundary layer transition in hypersonic flow. In *16th Fluid and Plasmadynamics Conference*, page 1763, 1983.

[102] Brandon C Chynoweth. *Measurements of transition dominated by the second-mode instability at Mach 6*. PhD thesis, Purdue University, 2018.

[103] Jeffrey R Carpenter, Edmund W Tedford, Eyal Heifetz, and Gregory A Lawrence. Instability in stratified shear flow: Review of a physical interpretation based on interacting waves. *Applied Mechanics Reviews*, 64(6), 2011.

[104] Jayahar Sivasubramanian and Hermann F Fasel. Numerical investigation of shockwave boundary layer interactions in supersonic flows. In *54th AIAA Aerospace Sciences Meeting*, page 0613, 2016.

[105] Christoph Hader and Hermann F Fasel. Fundamental resonance breakdown for a flared cone at mach 6. In *55th AIAA Aerospace Sciences Meeting*, page 0765, 2017.

[106] Tony Liang and Joseph Kuehl. Validation of porous impedance boundary condition for a pse code. In *AIAA AVIATION 2023 Forum*, page 3290, 2023.

[107] Alexander Wagner, Markus Kuhn, Jan Martinez Schramm, and Klaus Hannemann. Experiments on passive hypersonic boundary layer control using ultrasonically absorptive carbon–carbon material with random microstructure. *Experiments in Fluids*, 54:1–10, 2013.

[108] A. Wagner, K. Hannemann, and M. Kuhn. Ultrasonic absorption characteristics of porous carbon–carbon ceramics with random microstructure for passive hypersonic boundary layer transition control. *Experiments in Fluids*, 55:1–9, 2014.

[109] A. Wagner, C. Martinez Schramm, J.and Dittert, V. Sousa, D. I. Patel, and C. Scalo. Experimental and numerical acoustic characterization of ultrasonically absorptive porous materials. *AIAA 2018 Joint Thermophysics and Heat Transfer Conference*, 2018.

[110] A. Wagner. *Passive Hypersonic Boundary Layer Transition Control Using Ultrasonically Absorptive Carbon–Carbon Ceramic with Random Microstructure*. PhD dissertation, Katholieke Universiteit Leuven, 2014.

[111] Alexander Wagner, Klaus Hannemann, and Markus Kuhn. Ultrasonic absorption characteristics of porous carbon–carbon ceramics with random microstructure for passive hypersonic boundary layer transition control. *Experiments in fluids*, 55(6):1750, 2014.

[112] Viola Wartemann, Heinrich Lüdeke, and Neil D Sandham. Numerical investigation of hypersonic boundary-layer stabilization by porous surfaces. *AIAA journal*, 50(6):1281–1290, 2012.

[113] V.C.B. Sousa, D. Patel, J.D. Chapelier, V. Wartemann, A. Wagner, and C. Scalo. Numerical investigation of second-mode attenuation over carbon/carbon porous surfaces. *Journal of Spacecraft and Rockets*, 56:319–332, 2019.

[114] G. Müller and M. Möser. Handbook of engineering acoustics. *Springer Science & Business Media*, 2012.

[115] M. A. Kuczmarski and J. C. Johnston. Acoustic absorption in porous materials. *NASA/TM—2011-216995. (NASA Glenn Research Center, Cleveland, OH)*, 2011.

[116] T.J. Cox and O.P. D'antonio. Acoustic absorbers and diffusers: theory, design and application. *London and New York: Spon Press*, 2004.

[117] Arham Amin Khan, Tony Liang, and Joseph Kuehl. Influence of nose bluntness on crossflow instability. *Journal of Spacecraft and Rockets*, 59(5):1713–1725, 2022.

[118] Arham Amin Khan, Tony Liang, Armani Batista, and Joseph Kuehl. On energy redistribution for the nonlinear parabolized stability equations method. *Fluids*, 7(8):264, 2022.

Appendix A

DISCRETIZATION SCHEMES

A.1 Backward Finite Difference Scheme

$$\frac{\partial \phi'_{i,j}}{\partial y} = \frac{\phi'_{i,j-2} - 8\phi'_{i,j-1} + 8\phi'_{i,j+1} - \phi'_{i,j+2}}{12\Delta y}$$

$$\frac{\partial^2 \phi'_{i,j}}{\partial y^2} = \frac{-\phi'_{i,j-2} + 16\phi'_{i,j-1} - 30\phi'_{i,j-1} + 16\phi'_{i,j+1} - \phi'_{i,j+2}}{12(\Delta y)^2}$$

A.2 Central Finite Difference Scheme

$$\frac{\partial \phi_{i+1,j}}{\partial x} = \frac{3\phi_{i+1,j} - 4\phi_{i,j} + \phi_{i-1,j}}{2\Delta x}$$

Appendix B

DISTURBANCE NAVIER STOKES EQUATIONS

B.1 Conservation of mass

$$
\begin{aligned}
\frac{\partial \bar{\rho}}{\partial t} + \frac{\partial \rho'}{\partial t} + \frac{\partial}{\partial x}(\bar{\rho}\bar{u}) + \frac{\partial}{\partial x}(\bar{\rho}\tilde{u}) + \frac{\partial}{\partial x}(\rho'\bar{u}) + \frac{\partial}{\partial x}(\rho'\tilde{u}) \\
+ \frac{\partial}{\partial y}(\bar{\rho}\bar{v}) + \frac{\partial}{\partial y}(\bar{\rho}\tilde{v}) + \frac{\partial}{\partial y}(\rho'\bar{v}) + \frac{\partial}{\partial y}(\rho'\tilde{v}) \\
+ \frac{\partial}{\partial z}(\bar{\rho}\bar{w}) + \frac{\partial}{\partial z}(\bar{\rho}w') + \frac{\partial}{\partial z}(\rho'\bar{w}) + \frac{\partial}{\partial z}(\rho'w') = 0
\end{aligned}
$$

B.2 Conservation of momentum

B.2.1 X-momentum

$$\bar{\rho}\frac{\partial \bar{u}}{\partial t} + \bar{\rho}\frac{\partial \tilde{u}}{\partial t} + \rho'\frac{\partial \bar{u}}{\partial t} + \rho'\frac{\partial \tilde{u}}{\partial t}$$

$$+ \bar{\rho}\bar{u}\frac{\partial \bar{u}}{\partial x} + \bar{\rho}\bar{u}\frac{\partial \bar{u}}{\partial x} + \bar{\rho}\tilde{u}\frac{\partial \bar{u}}{\partial x} + \bar{\rho}\tilde{u}\frac{\partial \bar{u}}{\partial x} + \rho'\bar{u}\frac{\partial \bar{u}}{\partial x} + \rho'\bar{u}\frac{\partial \tilde{u}}{\partial x} + \rho'\tilde{u}\frac{\partial \bar{u}}{\partial x} + \rho'\tilde{u}\frac{\partial \tilde{u}}{\partial x}$$

$$+ \bar{\rho}\bar{v}\frac{\partial \bar{u}}{\partial y} + \bar{\rho}\bar{v}\frac{\partial \bar{u}}{\partial y} + \bar{\rho}\tilde{v}\frac{\partial \bar{u}}{\partial y} + \bar{\rho}\tilde{v}\frac{\partial \bar{u}}{\partial y} + \rho'\bar{v}\frac{\partial \bar{u}}{\partial y} + \rho'\bar{v}\frac{\partial \tilde{u}}{\partial y} + \rho'\tilde{v}\frac{\partial \bar{u}}{\partial y} + \rho'\tilde{v}\frac{\partial \tilde{u}}{\partial y}$$

$$+ \bar{\rho}\bar{w}\frac{\partial \bar{u}}{\partial z} + \bar{\rho}\bar{w}\frac{\partial \bar{u}}{\partial z} + \bar{\rho}w'\frac{\partial \bar{u}}{\partial z} + \bar{\rho}w'\frac{\partial \bar{u}}{\partial z} + \rho'\bar{w}\frac{\partial \bar{u}}{\partial z} + \rho'\bar{w}\frac{\partial \tilde{u}}{\partial z} + \rho'w'\frac{\partial \bar{u}}{\partial z} + \rho'w'\frac{\partial \tilde{u}}{\partial z}$$

$$= -\left(\frac{\partial}{\partial x}(\bar{\rho}\bar{T}) + \frac{\partial}{\partial x}(\bar{\rho}\tilde{T}) + \frac{\partial}{\partial x}(\rho'\bar{T}) + \frac{\partial}{\partial x}(\rho'\tilde{T})\right)$$

$$+ \frac{1}{Re}\frac{\partial}{\partial x}\left[2\left(\bar{\mu}\frac{\partial \bar{u}}{\partial x} + \bar{\mu}\frac{\partial \tilde{u}}{\partial x} + \mu'\frac{\partial \bar{u}}{\partial x} + \mu'\frac{\partial \tilde{u}}{\partial x}\right)\right.$$

$$\left. + \left(\bar{\lambda}\frac{\partial \bar{u}}{\partial x} + \bar{\lambda}\frac{\partial \tilde{u}}{\partial x} + \bar{\lambda}\frac{\partial \bar{v}}{\partial y} + \bar{\lambda}\frac{\partial \tilde{v}}{\partial y} + \bar{\lambda}\frac{\partial \bar{w}}{\partial z} + \bar{\lambda}\frac{\partial w'}{\partial z} + \lambda'\frac{\partial \bar{u}}{\partial x} + \lambda'\frac{\partial \tilde{u}}{\partial x} + \lambda'\frac{\partial \bar{v}}{\partial y} + \lambda'\frac{\partial \tilde{v}}{\partial y} + \lambda'\frac{\partial \bar{w}}{\partial z} + \lambda'\frac{\partial w'}{\partial z}\right)\right]$$

$$+ \frac{1}{Re}\frac{\partial}{\partial y}\left(\bar{\mu}\frac{\partial \bar{u}}{\partial y} + \bar{\mu}\frac{\partial \tilde{u}}{\partial y} + \mu'\frac{\partial \bar{u}}{\partial y} + \mu'\frac{\partial \tilde{u}}{\partial y} + \bar{\mu}\frac{\partial \bar{v}}{\partial x} + \bar{\mu}\frac{\partial \tilde{v}}{\partial x} + \mu'\frac{\partial \bar{v}}{\partial x} + \mu'\frac{\partial \tilde{v}}{\partial x}\right)$$

$$+ \frac{1}{Re}\frac{\partial}{\partial z}\left(\bar{\mu}\frac{\partial \bar{u}}{\partial z} + \bar{\mu}\frac{\partial \tilde{u}}{\partial z} + \mu'\frac{\partial \bar{u}}{\partial z} + \mu'\frac{\partial \tilde{u}}{\partial z} + \bar{\mu}\frac{\partial \bar{w}}{\partial x} + \bar{\mu}\frac{\partial w'}{\partial x} + \mu'\frac{\partial \bar{w}}{\partial x} + \mu'\frac{\partial w'}{\partial x}\right)$$

B.2.2 Y-momentum

$$\bar{\rho}\frac{\partial\bar{v}}{\partial t}+\bar{\rho}\frac{\partial\tilde{v}}{\partial t}+\rho'\frac{\partial\bar{v}}{\partial t}+\rho'\frac{\partial\tilde{v}}{\partial t}$$

$$+\bar{\rho}\bar{u}\frac{\partial\bar{v}}{\partial x}+\bar{\rho}\bar{u}\frac{\partial\bar{v}}{\partial x}+\bar{\rho}\tilde{u}\frac{\partial\bar{v}}{\partial x}+\bar{\rho}\tilde{u}\frac{\partial\bar{v}}{\partial x}+\rho'\bar{u}\frac{\partial\bar{v}}{\partial x}+\rho'\bar{u}\frac{\partial\tilde{v}}{\partial x}+\rho'\tilde{u}\frac{\partial\bar{v}}{\partial x}+\rho'\tilde{u}\frac{\partial\tilde{v}}{\partial x}$$

$$+\bar{\rho}\bar{v}\frac{\partial\bar{v}}{\partial y}+\bar{\rho}\bar{v}\frac{\partial\bar{v}}{\partial y}+\bar{\rho}\tilde{v}\frac{\partial\bar{v}}{\partial y}+\bar{\rho}\tilde{v}\frac{\partial\bar{v}}{\partial y}+\rho'\bar{v}\frac{\partial\bar{v}}{\partial y}+\rho'\bar{v}\frac{\partial\tilde{v}}{\partial y}+\rho'\tilde{v}\frac{\partial\bar{v}}{\partial y}+\rho'\tilde{v}\frac{\partial\tilde{v}}{\partial y}$$

$$+\bar{\rho}\bar{w}\frac{\partial\bar{v}}{\partial z}+\bar{\rho}\bar{w}\frac{\partial\bar{v}}{\partial z}+\bar{\rho}w'\frac{\partial\bar{v}}{\partial z}+\bar{\rho}w'\frac{\partial\bar{v}}{\partial z}+\rho'\bar{w}\frac{\partial\bar{v}}{\partial z}+\rho'\bar{w}\frac{\partial\tilde{v}}{\partial z}+\rho'w'\frac{\partial\bar{v}}{\partial z}+\rho'w'\frac{\partial\tilde{v}}{\partial z}$$

$$=-\left(\frac{\partial}{\partial y}(\bar{\rho}\bar{T})+\frac{\partial}{\partial y}(\bar{\rho}\tilde{T})+\frac{\partial}{\partial y}(\rho'\bar{T})+\frac{\partial}{\partial y}(\rho'\tilde{T})\right)$$

$$+\frac{1}{Re}\frac{\partial}{\partial x}\left(\bar{\mu}\frac{\partial\bar{v}}{\partial x}+\bar{\mu}\frac{\partial\tilde{v}}{\partial x}+\mu'\frac{\partial\bar{v}}{\partial x}+\mu'\frac{\partial\tilde{v}}{\partial x}+\bar{\mu}\frac{\partial\bar{u}}{\partial y}+\bar{\mu}\frac{\partial\tilde{u}}{\partial y}+\mu'\frac{\partial\bar{u}}{\partial y}+\mu'\frac{\partial\tilde{u}}{\partial y}\right)$$

$$+\frac{1}{Re}\frac{\partial}{\partial y}\left[2\left(\bar{\mu}\frac{\partial\bar{v}}{\partial y}+\bar{\mu}\frac{\partial\tilde{v}}{\partial y}+\mu'\frac{\partial\bar{v}}{\partial y}+\mu'\frac{\partial\tilde{v}}{\partial y}\right)\right.$$

$$\left.+\left(\bar{\lambda}\frac{\partial\bar{u}}{\partial x}+\bar{\lambda}\frac{\partial\tilde{u}}{\partial x}+\bar{\lambda}\frac{\partial\bar{v}}{\partial y}+\bar{\lambda}\frac{\partial\tilde{v}}{\partial y}+\bar{\lambda}\frac{\partial\bar{w}}{\partial z}+\bar{\lambda}\frac{\partial w'}{\partial z}+\lambda'\frac{\partial\bar{u}}{\partial x}+\lambda'\frac{\partial\tilde{u}}{\partial x}+\lambda'\frac{\partial\bar{v}}{\partial y}+\lambda'\frac{\partial\tilde{v}}{\partial y}+\lambda'\frac{\partial\bar{w}}{\partial z}+\lambda'\frac{\partial w'}{\partial z}\right)\right]$$

$$+\frac{1}{Re}\frac{\partial}{\partial z}\left(\bar{\mu}\frac{\partial\bar{v}}{\partial z}+\bar{\mu}\frac{\partial\tilde{v}}{\partial z}+\mu'\frac{\partial\bar{v}}{\partial z}+\mu'\frac{\partial\tilde{v}}{\partial z}+\bar{\mu}\frac{\partial\bar{w}}{\partial y}+\bar{\mu}\frac{\partial w'}{\partial y}+\mu'\frac{\partial\bar{w}}{\partial y}+\mu'\frac{\partial w'}{\partial y}\right)$$

B.2.3 Z-momentum

$$\bar{\rho}\frac{\partial \bar{w}}{\partial t} + \bar{\rho}\frac{\partial \tilde{w}}{\partial t} + \rho'\frac{\partial \bar{w}}{\partial t} + \rho'\frac{\partial \tilde{w}}{\partial t}$$

$$+ \bar{\rho}\bar{u}\frac{\partial \bar{w}}{\partial x} + \bar{\rho}\bar{u}\frac{\partial \bar{w}}{\partial x} + \bar{\rho}\tilde{u}\frac{\partial \bar{w}}{\partial x} + \bar{\rho}\tilde{u}\frac{\partial \bar{w}}{\partial x} + \rho'\bar{u}\frac{\partial \bar{w}}{\partial x} + \rho'\bar{u}\frac{\partial w'}{\partial x} + \rho'\tilde{u}\frac{\partial \bar{w}}{\partial x} + \rho'\tilde{u}\frac{\partial w'}{\partial x}$$

$$+ \bar{\rho}\bar{v}\frac{\partial \bar{w}}{\partial y} + \bar{\rho}\bar{v}\frac{\partial \bar{w}}{\partial y} + \bar{\rho}\tilde{v}\frac{\partial \bar{w}}{\partial y} + \bar{\rho}\tilde{v}\frac{\partial \bar{w}}{\partial y} + \rho'\bar{v}\frac{\partial \bar{w}}{\partial y} + \rho'\bar{v}\frac{\partial w'}{\partial y} + \rho'\tilde{v}\frac{\partial \bar{w}}{\partial y} + \rho'\tilde{v}\frac{\partial w'}{\partial y}$$

$$+ \bar{\rho}\bar{w}\frac{\partial \bar{w}}{\partial z} + \bar{\rho}\bar{w}\frac{\partial \bar{w}}{\partial z} + \bar{\rho}w'\frac{\partial \bar{w}}{\partial z} + \bar{\rho}w'\frac{\partial \bar{w}}{\partial z} + \rho'\bar{w}\frac{\partial \bar{w}}{\partial z} + \rho'\bar{w}\frac{\partial w'}{\partial z} + \rho'w'\frac{\partial \bar{w}}{\partial z} + \rho'w'$$

$$= -\left(\frac{\partial}{\partial z}(\bar{\rho}\bar{T}) + \frac{\partial}{\partial z}(\bar{\rho}\tilde{T}) + \frac{\partial}{\partial z}(\rho'\bar{T}) + \frac{\partial}{\partial z}(\rho'\tilde{T})\right)$$

$$+ \frac{1}{Re}\frac{\partial}{\partial x}\left(\bar{\mu}\frac{\partial \bar{w}}{\partial x} + \bar{\mu} + \mu'\frac{\partial \bar{w}}{\partial x} + \mu' + \bar{\mu}\frac{\partial \bar{u}}{\partial z} + \bar{\mu}\frac{\partial \tilde{u}}{\partial z} + \mu'\frac{\partial \bar{u}}{\partial z} + \mu'\frac{\partial \tilde{u}}{\partial z}\right)$$

$$+ \frac{1}{Re}\frac{\partial}{\partial y}\left(\bar{\mu}\frac{\partial \bar{w}}{\partial y} + \bar{\mu} + \mu'\frac{\partial \bar{w}}{\partial y} + \mu' + \bar{\mu}\frac{\partial \bar{v}}{\partial z} + \bar{\mu}\frac{\partial \tilde{v}}{\partial z} + \mu'\frac{\partial \bar{v}}{\partial z} + \mu'\frac{\partial \tilde{v}}{\partial z}\right)$$

$$+ \frac{1}{Re}\frac{\partial}{\partial z}\left[2\left(\bar{\mu}\frac{\partial \bar{w}}{\partial z} + \bar{\mu}\frac{\partial w'}{\partial z} + \mu'\frac{\partial \bar{w}}{\partial z} + \mu'\frac{\partial w'}{\partial z}\right)\right.$$

$$\left.+\left(\bar{\lambda}\frac{\partial \bar{u}}{\partial x}+\bar{\lambda}\frac{\partial \tilde{u}}{\partial x}+\bar{\lambda}\frac{\partial \bar{v}}{\partial y}+\bar{\lambda}\frac{\partial \tilde{v}}{\partial y}+\bar{\lambda}\frac{\partial \bar{w}}{\partial z}+\bar{\lambda}\frac{\partial w'}{\partial z}+\lambda'\frac{\partial \bar{u}}{\partial x}+\lambda'\frac{\partial \tilde{u}}{\partial x}+\lambda'\frac{\partial \bar{v}}{\partial y}+\lambda'\frac{\partial \tilde{v}}{\partial y}+\lambda'\frac{\partial \bar{w}}{\partial z}+\lambda'\frac{\partial w'}{\partial z}\right)\right]$$

B.3 Conservation of Energy

$$
\begin{aligned}
&\bar{\rho}\bar{c}_p\frac{\partial \bar{T}}{\partial t} + \bar{\rho}\bar{c}_p\frac{\partial \tilde{T}}{\partial t} + \bar{\rho}c_p'\frac{\partial \bar{T}}{\partial t} + \bar{\rho}c_p'\frac{\partial \tilde{T}}{\partial t} + \rho'\bar{c}_p\frac{\partial \bar{T}}{\partial t} + \rho'\bar{c}_p\frac{\partial \tilde{T}}{\partial t} + \rho'c_p'\frac{\partial \bar{T}}{\partial t} + \rho'c_p'\frac{\partial \tilde{T}}{\partial t} \\
&+ \Bigg(\bar{\rho}\bar{c}_p\bar{u}\frac{\partial \bar{T}}{\partial x} + \bar{\rho}\bar{c}_p\bar{u}\frac{\partial \bar{T}}{\partial x} + \bar{\rho}\bar{c}_p\tilde{u}\frac{\partial \bar{T}}{\partial x} + \bar{\rho}\bar{c}_p\tilde{u}\frac{\partial \bar{T}}{\partial x} + \rho'\bar{c}_p\bar{u}\frac{\partial \bar{T}}{\partial x} + \rho'\bar{c}_p\bar{u}\frac{\partial \tilde{T}}{\partial x} + \rho'\bar{c}_p\tilde{u}\frac{\partial \bar{T}}{\partial x} + \rho'\bar{c}_p\tilde{u}\frac{\partial \tilde{T}}{\partial x} \\
&+ \bar{\rho}\bar{c}_p\bar{v}\frac{\partial \bar{T}}{\partial y} + \bar{\rho}\bar{c}_p\bar{v}\frac{\partial \bar{T}}{\partial y} + \bar{\rho}\bar{c}_p\tilde{v}\frac{\partial \bar{T}}{\partial y} + \bar{\rho}\bar{c}_p\tilde{v}\frac{\partial \bar{T}}{\partial y} + \rho'\bar{c}_p\bar{v}\frac{\partial \bar{T}}{\partial y} + \rho'\bar{c}_p\bar{v}\frac{\partial \tilde{T}}{\partial y} + \rho'\bar{c}_p\tilde{v}\frac{\partial \bar{T}}{\partial y} + \rho'\bar{c}_p\tilde{v}\frac{\partial \tilde{T}}{\partial y} \\
&+ \bar{\rho}\bar{c}_p\bar{w}\frac{\partial \bar{T}}{\partial z} + \bar{\rho}\bar{c}_p\bar{w}\frac{\partial \bar{T}}{\partial z} + \bar{\rho}\bar{c}_p w'\frac{\partial \bar{T}}{\partial z} + \bar{\rho}\bar{c}_p w'\frac{\partial \bar{T}}{\partial z} + \rho'\bar{c}_p\bar{w}\frac{\partial \bar{T}}{\partial z} + \rho'\bar{c}_p\bar{w}\frac{\partial \tilde{T}}{\partial z} + \rho'\bar{c}_p w'\frac{\partial \bar{T}}{\partial z} + \rho'\bar{c}_p w'\frac{\partial \tilde{T}}{\partial z}\Bigg) \\
&+ \Bigg(\bar{\rho}c_p'\bar{u}\frac{\partial \bar{T}}{\partial x} + \bar{\rho}c_p'\bar{u}\frac{\partial \bar{T}}{\partial x} + \bar{\rho}c_p'\tilde{u}\frac{\partial \bar{T}}{\partial x} + \bar{\rho}c_p'\tilde{u}\frac{\partial \bar{T}}{\partial x} + \rho'c_p'\bar{u}\frac{\partial \bar{T}}{\partial x} + \rho'c_p'\bar{u}\frac{\partial \tilde{T}}{\partial x} + \rho'c_p'\tilde{u}\frac{\partial \bar{T}}{\partial x} + \rho'c_p'\tilde{u}\frac{\partial \tilde{T}}{\partial x} \\
&+ \bar{\rho}c_p'\bar{v}\frac{\partial \bar{T}}{\partial y} + \bar{\rho}c_p'\bar{v}\frac{\partial \bar{T}}{\partial y} + \bar{\rho}c_p'\tilde{v}\frac{\partial \bar{T}}{\partial y} + \bar{\rho}c_p'\tilde{v}\frac{\partial \bar{T}}{\partial y} + \rho'c_p'\bar{v}\frac{\partial \bar{T}}{\partial y} + \rho'c_p'\bar{v}\frac{\partial \tilde{T}}{\partial y} + \rho'c_p'\tilde{v}\frac{\partial \bar{T}}{\partial y} + \rho'c_p'\tilde{v}\frac{\partial \tilde{T}}{\partial y} \\
&+ \bar{\rho}c_p'\bar{w}\frac{\partial \bar{T}}{\partial z} + \bar{\rho}c_p'\bar{w}\frac{\partial \bar{T}}{\partial z} + \bar{\rho}c_p' w'\frac{\partial \bar{T}}{\partial z} + \bar{\rho}c_p' w'\frac{\partial \bar{T}}{\partial z} + \rho'c_p'\bar{w}\frac{\partial \bar{T}}{\partial z} + \rho'c_p'\bar{w}\frac{\partial \tilde{T}}{\partial z} + \rho'c_p' w'\frac{\partial \bar{T}}{\partial z} + \rho'c_p' w'\frac{\partial \tilde{T}}{\partial z}\Bigg) \\
&= \frac{1}{PrRe}\Bigg[\frac{\partial}{\partial x}\left(\bar{\kappa}\frac{\partial \bar{T}}{\partial x} + \bar{\kappa}\frac{\partial \tilde{T}}{\partial x} + \kappa'\frac{\partial \bar{T}}{\partial x} + \kappa'\frac{\partial \tilde{T}}{\partial x}\right) + \frac{\partial}{\partial y}\left(\bar{\kappa}\frac{\partial \bar{T}}{\partial y} + \bar{\kappa}\frac{\partial \tilde{T}}{\partial y} + \kappa'\frac{\partial \bar{T}}{\partial y} + \kappa'\frac{\partial \tilde{T}}{\partial y}\right) \\
&\qquad + \frac{\partial}{\partial z}\left(\bar{\kappa}\frac{\partial \bar{T}}{\partial z} + \bar{\kappa}\frac{\partial \tilde{T}}{\partial z} + \kappa'\frac{\partial \bar{T}}{\partial z} + \kappa'\frac{\partial \tilde{T}}{\partial z}\right)\Bigg]
\end{aligned}
$$

$$
+ (\gamma - 1) M^2 \left[\frac{\partial}{\partial t}(\bar{\rho}\bar{T} + \bar{\rho}\tilde{T} + \rho'\bar{T} + \rho'\tilde{T}) \right.
$$

$$
+\bar{u}\frac{\partial}{\partial x}(\bar{\rho}\bar{T})+\bar{u}\frac{\partial}{\partial x}(\bar{\rho}\tilde{T})+\bar{u}\frac{\partial}{\partial x}(\rho'\bar{T})+\bar{u}\frac{\partial}{\partial x}(\rho'\tilde{T})+\tilde{u}\frac{\partial}{\partial x}(\bar{\rho}\bar{T})+\tilde{u}\frac{\partial}{\partial x}(\bar{\rho}\tilde{T})+\tilde{u}\frac{\partial}{\partial x}(\rho'\bar{T})+\tilde{u}\frac{\partial}{\partial x}(\rho'\tilde{T})
$$

$$
+\bar{v}\frac{\partial}{\partial y}(\bar{\rho}\bar{T})+\bar{v}\frac{\partial}{\partial y}(\bar{\rho}\tilde{T})+\bar{v}\frac{\partial}{\partial y}(\rho'\bar{T})+\bar{v}\frac{\partial}{\partial y}(\rho'\tilde{T})+\tilde{v}\frac{\partial}{\partial y}(\bar{\rho}\bar{T})+\tilde{v}\frac{\partial}{\partial y}(\bar{\rho}\tilde{T})+\tilde{v}\frac{\partial}{\partial y}(\rho'\bar{T})+\tilde{v}\frac{\partial}{\partial y}(\rho'\tilde{T})
$$

$$
\left. +\bar{w}\frac{\partial}{\partial z}(\bar{\rho}\bar{T})+\bar{w}\frac{\partial}{\partial z}(\bar{\rho}\tilde{T})+\bar{w}\frac{\partial}{\partial z}(\rho'\bar{T})+\bar{w}\frac{\partial}{\partial z}(\rho'\tilde{T})+w'\frac{\partial}{\partial z}(\bar{\rho}\bar{T})+w'\frac{\partial}{\partial z}(\bar{\rho}\tilde{T})+w'\frac{\partial}{\partial z}(\rho'\bar{T})+w'\frac{\partial}{\partial z}(\rho'\tilde{T}) \right]
$$

$$+\frac{\gamma-1}{Re}M^2\Bigg[2\Bigg(\bar{\mu}\left(\frac{\partial\bar{u}}{\partial x}\right)^2+\bar{\mu}\frac{\partial\bar{u}}{\partial x}\frac{\partial\tilde{u}}{\partial x}+\bar{\mu}\frac{\partial\tilde{u}}{\partial x}\frac{\partial\bar{u}}{\partial x}+\bar{\mu}\left(\frac{\partial\tilde{u}}{\partial x}\right)^2+\mu'\left(\frac{\partial\bar{u}}{\partial x}\right)^2+\mu'\frac{\partial\bar{u}}{\partial x}\frac{\partial\tilde{u}}{\partial x}+\mu'\frac{\partial\tilde{u}}{\partial x}\frac{\partial\bar{u}}{\partial x}+\mu'\left(\frac{\partial\tilde{u}}{\partial x}\right)^2\Bigg)$$

$$+2\Bigg(\bar{\mu}\left(\frac{\partial\bar{v}}{\partial y}\right)^2+\bar{\mu}\frac{\partial\bar{v}}{\partial y}\frac{\partial\tilde{v}}{\partial y}+\bar{\mu}\frac{\partial\tilde{v}}{\partial y}\frac{\partial\bar{v}}{\partial y}+\bar{\mu}\left(\frac{\partial\tilde{v}}{\partial y}\right)^2+\mu'\left(\frac{\partial\bar{v}}{\partial y}\right)^2+\mu'\frac{\partial\bar{v}}{\partial y}\frac{\partial\tilde{v}}{\partial y}+\mu'\frac{\partial\tilde{v}}{\partial y}\frac{\partial\bar{v}}{\partial y}+\mu'\left(\frac{\partial\tilde{v}}{\partial y}\right)^2\Bigg)$$

$$+2\Bigg(\bar{\mu}\left(\frac{\partial\bar{w}}{\partial z}\right)^2+\bar{\mu}\frac{\partial\bar{w}}{\partial z}\frac{\partial w'}{\partial z}+\bar{\mu}\frac{\partial w'}{\partial z}\frac{\partial\bar{w}}{\partial z}+\bar{\mu}\left(\frac{\partial w'}{\partial z}\right)^2+\mu'\left(\frac{\partial\bar{w}}{\partial z}\right)^2+\mu'\frac{\partial\bar{w}}{\partial z}\frac{\partial w'}{\partial z}+\mu'\frac{\partial w'}{\partial z}\frac{\partial\bar{w}}{\partial z}+\mu'\left(\frac{\partial w'}{\partial z}\right)^2\Bigg)$$

$$+\Bigg[\bar{\mu}\left(\frac{\partial\bar{v}}{\partial x}\right)^2+\bar{\mu}\frac{\partial\bar{v}}{\partial x}\frac{\partial\tilde{v}}{\partial x}+\bar{\mu}\frac{\partial\bar{v}}{\partial x}\frac{\partial\bar{u}}{\partial y}+\bar{\mu}\frac{\partial\bar{v}}{\partial x}\frac{\partial\tilde{u}}{\partial y}+\bar{\mu}\frac{\partial\tilde{v}}{\partial x}\frac{\partial\bar{v}}{\partial x}+\bar{\mu}\left(\frac{\partial\tilde{v}}{\partial x}\right)^2+\bar{\mu}\frac{\partial\tilde{v}}{\partial x}\frac{\partial\bar{u}}{\partial x}+\bar{\mu}\frac{\partial\tilde{v}}{\partial x}\frac{\partial\tilde{u}}{\partial x}$$

$$+\bar{\mu}\frac{\partial\bar{u}}{\partial y}\frac{\partial\bar{v}}{\partial x}+\bar{\mu}\frac{\partial\bar{u}}{\partial y}\frac{\partial\tilde{v}}{\partial x}+\bar{\mu}\left(\frac{\partial\bar{u}}{\partial x}\right)^2+\bar{\mu}\frac{\partial\bar{u}}{\partial y}\frac{\partial\tilde{u}}{\partial y}+\bar{\mu}\frac{\partial\tilde{u}}{\partial y}\frac{\partial\bar{v}}{\partial x}+\bar{\mu}\frac{\partial\tilde{u}}{\partial y}\frac{\partial\tilde{v}}{\partial x}+\bar{\mu}\frac{\partial\tilde{u}}{\partial y}\frac{\partial\bar{u}}{\partial y}+\bar{\mu}\left(\frac{\partial\tilde{u}}{\partial x}\right)^2$$

$$+\mu'\left(\frac{\partial\bar{v}}{\partial x}\right)^2+\mu'\frac{\partial\bar{v}}{\partial x}\frac{\partial\tilde{v}}{\partial x}+\mu'\frac{\partial\bar{v}}{\partial x}\frac{\partial\bar{u}}{\partial y}+\mu'\frac{\partial\bar{v}}{\partial x}\frac{\partial\tilde{u}}{\partial y}+\mu'\frac{\partial\tilde{v}}{\partial x}\frac{\partial\bar{v}}{\partial x}+\mu'\left(\frac{\partial\tilde{v}}{\partial x}\right)^2+\mu'\frac{\partial\tilde{v}}{\partial x}\frac{\partial\bar{u}}{\partial x}+\mu'\frac{\partial\tilde{v}}{\partial x}\frac{\partial\tilde{u}}{\partial x}$$

$$+\mu'\frac{\partial\bar{u}}{\partial y}\frac{\partial\bar{v}}{\partial x}+\mu'\frac{\partial\bar{u}}{\partial y}\frac{\partial\tilde{v}}{\partial x}+\mu'\left(\frac{\partial\bar{u}}{\partial x}\right)^2+\mu'\frac{\partial\bar{u}}{\partial y}\frac{\partial\tilde{u}}{\partial y}+\mu'\frac{\partial\tilde{u}}{\partial y}\frac{\partial\bar{v}}{\partial x}+\mu'\frac{\partial\tilde{u}}{\partial y}\frac{\partial\tilde{v}}{\partial x}+\mu'\frac{\partial\tilde{u}}{\partial y}\frac{\partial\bar{u}}{\partial y}+\mu'\left(\frac{\partial\tilde{u}}{\partial x}\right)^2\Bigg]$$

$$+\Bigg[\bar{\mu}\left(\frac{\partial\bar{w}}{\partial x}\right)^2+\bar{\mu}\frac{\partial\bar{w}}{\partial x}+\bar{\mu}\frac{\partial\bar{w}}{\partial x}\frac{\partial\bar{u}}{\partial z}+\bar{\mu}\frac{\partial\bar{w}}{\partial x}\frac{\partial\tilde{u}}{\partial z}+\bar{\mu}\frac{\partial w'}{\partial x}\frac{\partial\bar{w}}{\partial x}+\bar{\mu}\left(\frac{\partial w'}{\partial x}\right)^2+\bar{\mu}\frac{\partial w'}{\partial x}\frac{\partial\bar{u}}{\partial z}+\bar{\mu}\frac{\partial w'}{\partial x}\frac{\partial\tilde{u}}{\partial z}$$

$$+\bar{\mu}\frac{\partial\bar{u}}{\partial z}\frac{\partial\bar{w}}{\partial x}+\bar{\mu}\frac{\partial\bar{u}}{\partial z}\frac{\partial w'}{\partial x}+\bar{\mu}\left(\frac{\partial\bar{u}}{\partial x}\right)^2+\bar{\mu}\frac{\partial\bar{u}}{\partial z}\frac{\partial\tilde{u}}{\partial z}+\bar{\mu}\frac{\partial\tilde{u}}{\partial z}\frac{\partial\bar{w}}{\partial x}+\bar{\mu}\frac{\partial\tilde{u}}{\partial z}\frac{\partial w'}{\partial x}+\bar{\mu}\frac{\partial\tilde{u}}{\partial z}\frac{\partial\bar{u}}{\partial z}+\bar{\mu}\left(\frac{\partial\tilde{u}}{\partial x}\right)^2$$

$$+\mu'\left(\frac{\partial\bar{w}}{\partial x}\right)^2+\mu'\frac{\partial\bar{w}}{\partial x}\frac{\partial w'}{\partial x}+\mu'\frac{\partial\bar{w}}{\partial x}\frac{\partial\bar{u}}{\partial z}+\mu'\frac{\partial\bar{w}}{\partial x}\frac{\partial\tilde{u}}{\partial z}+\mu'\frac{\partial w'}{\partial x}\frac{\partial\bar{w}}{\partial x}+\mu'\left(\frac{\partial w'}{\partial x}\right)^2+\mu'\frac{\partial w'}{\partial x}\frac{\partial\bar{u}}{\partial z}+\mu'\frac{\partial w'}{\partial x}\frac{\partial\tilde{u}}{\partial z}$$

$$+\mu'\frac{\partial\bar{u}}{\partial z}\frac{\partial\bar{w}}{\partial x}+\mu'\frac{\partial\bar{u}}{\partial z}+\mu'\left(\frac{\partial\bar{u}}{\partial z}\right)^2+\mu'\frac{\partial\bar{u}}{\partial z}\frac{\partial\tilde{u}}{\partial z}+\mu'\frac{\partial\tilde{u}}{\partial z}\frac{\partial\bar{w}}{\partial x}+\mu'\frac{\partial\tilde{u}}{\partial z}+\mu'\frac{\partial\tilde{u}}{\partial z}\frac{\partial\bar{u}}{\partial z}+\mu'\left(\frac{\partial\tilde{u}}{\partial z}\right)^2\Bigg]$$

$$+\Bigg[\bar{\mu}\left(\frac{\partial\bar{w}}{\partial y}\right)^2+\bar{\mu}\frac{\partial\bar{w}}{\partial y}+\bar{\mu}\frac{\partial\bar{w}}{\partial y}\frac{\partial\bar{v}}{\partial z}+\bar{\mu}\frac{\partial\bar{w}}{\partial y}\frac{\partial\tilde{v}}{\partial z}+\bar{\mu}\frac{\partial w'}{\partial y}\frac{\partial\bar{w}}{\partial y}+\bar{\mu}\left(\frac{\partial w'}{\partial y}\right)^2+\bar{\mu}\frac{\partial w'}{\partial y}\frac{\partial\bar{v}}{\partial z}+\bar{\mu}\frac{\partial w'}{\partial y}\frac{\partial\tilde{v}}{\partial z}$$

$$+\bar{\mu}\frac{\partial\bar{v}}{\partial z}\frac{\partial\bar{w}}{\partial y}+\bar{\mu}\frac{\partial\bar{v}}{\partial z}\frac{\partial w'}{\partial y}+\bar{\mu}\left(\frac{\partial\bar{v}}{\partial z}\right)^2+\bar{\mu}\frac{\partial\bar{v}}{\partial z}\frac{\partial\tilde{v}}{\partial z}+\bar{\mu}\frac{\partial\tilde{v}}{\partial z}\frac{\partial\bar{w}}{\partial y}+\bar{\mu}\frac{\partial\tilde{v}}{\partial z}\frac{\partial w'}{\partial y}+\bar{\mu}\frac{\partial\tilde{v}}{\partial z}\frac{\partial\bar{v}}{\partial z}+\bar{\mu}\left(\frac{\partial\tilde{v}}{\partial x}\right)^2$$

$$+\mu'\left(\frac{\partial\bar{w}}{\partial y}\right)^2+\mu'\frac{\partial\bar{w}}{\partial y}+\mu'\frac{\partial\bar{w}}{\partial y}\frac{\partial\bar{v}}{\partial z}+\mu'\frac{\partial\bar{w}}{\partial y}\frac{\partial\tilde{v}}{\partial z}+\mu'\frac{\partial w'}{\partial y}\frac{\partial\bar{w}}{\partial y}+\mu'\left(\frac{\partial w'}{\partial y}\right)^2+\mu'\frac{\partial w'}{\partial y}\frac{\partial\bar{v}}{\partial z}+\mu'\frac{\partial w'}{\partial y}\frac{\partial\tilde{v}}{\partial z}$$

$$+\mu'\frac{\partial\bar{v}}{\partial z}\frac{\partial\bar{w}}{\partial y}+\mu'\frac{\partial\bar{v}}{\partial z}\frac{\partial w'}{\partial y}+\mu'\left(\frac{\partial\bar{v}}{\partial z}\right)^2+\mu'\frac{\partial\bar{v}}{\partial z}\frac{\partial\tilde{v}}{\partial z}+\mu'\frac{\partial\tilde{v}}{\partial z}\frac{\partial\bar{w}}{\partial y}+\mu'\frac{\partial\tilde{v}}{\partial z}\frac{\partial w'}{\partial y}+\mu'\frac{\partial\tilde{v}}{\partial z}\frac{\partial\bar{v}}{\partial z}+\mu'\left(\frac{\partial\tilde{v}}{\partial x}\right)^2\Bigg]\Bigg]$$

$$
\begin{aligned}
&+\frac{\gamma-1}{Re}M^2\Bigg[\bar{\lambda}\left(\frac{\partial\bar{u}}{\partial x}\right)^2+\bar{\lambda}\frac{\partial\bar{u}}{\partial x}\frac{\partial\tilde{u}}{\partial x}+\bar{\lambda}\frac{\partial\bar{u}}{\partial x}\frac{\partial\bar{u}}{\partial y}+\bar{\lambda}\frac{\partial\bar{u}}{\partial x}+\bar{\lambda}\frac{\partial\bar{u}}{\partial x}\frac{\partial\bar{w}}{\partial z}+\bar{\lambda}\frac{\partial\bar{u}}{\partial x}\frac{\partial w'}{\partial z}\\
&\quad+\bar{\lambda}\frac{\partial\tilde{u}}{\partial x}\frac{\partial\bar{u}}{\partial x}+\bar{\lambda}\left(\frac{\partial\tilde{u}}{\partial x}\right)^2+\bar{\lambda}\frac{\partial\tilde{u}}{\partial x}\frac{\partial\bar{v}}{\partial y}+\bar{\lambda}\frac{\partial\tilde{u}}{\partial x}\frac{\partial\tilde{v}}{\partial y}+\bar{\lambda}\frac{\partial\tilde{u}}{\partial x}\frac{\partial\bar{w}}{\partial z}+\bar{\lambda}\frac{\partial\tilde{u}}{\partial x}\frac{\partial w'}{\partial z}
\end{aligned}
$$

$$
+\bar{\lambda}\frac{\partial\bar{v}}{\partial y}\frac{\partial\bar{u}}{\partial x}+\bar{\lambda}\frac{\partial\tilde{v}}{\partial y}\frac{\partial\tilde{u}}{\partial x}+\bar{\lambda}\left(\frac{\partial\bar{v}}{\partial y}\right)^2+\bar{\lambda}\frac{\partial\bar{v}}{\partial y}\frac{\partial\tilde{v}}{\partial y}+\bar{\lambda}\frac{\partial\bar{v}}{\partial y}\frac{\partial\bar{w}}{\partial z}+\bar{\lambda}\frac{\partial\bar{v}}{\partial y}\frac{\partial w'}{\partial z}
$$

$$
+\bar{\lambda}\frac{\partial\tilde{v}}{\partial y}\frac{\partial\bar{u}}{\partial x}+\bar{\lambda}\frac{\partial\tilde{v}}{\partial y}\frac{\partial\tilde{v}}{\partial x}+\bar{\lambda}\frac{\partial\bar{v}}{\partial y}\frac{\partial\tilde{v}}{\partial y}+\bar{\lambda}\left(\frac{\partial\tilde{v}}{\partial y}\right)^2+\bar{\lambda}\frac{\partial\tilde{v}}{\partial y}\frac{\partial\bar{w}}{\partial z}+\bar{\lambda}\frac{\partial\tilde{v}}{\partial y}\frac{\partial w'}{\partial z}
$$

$$
+\bar{\lambda}\frac{\partial\bar{w}}{\partial z}\frac{\partial\bar{u}}{\partial x}+\bar{\lambda}\frac{\partial\bar{w}}{\partial z}\frac{\partial\tilde{u}}{\partial x}+\bar{\lambda}\frac{\partial\bar{w}}{\partial z}\frac{\partial\bar{v}}{\partial y}+\bar{\lambda}\frac{\partial\bar{w}}{\partial z}\frac{\partial\tilde{v}}{\partial y}+\bar{\lambda}\left(\frac{\partial\bar{w}}{\partial z}\right)^2+\bar{\lambda}\frac{\partial\bar{w}}{\partial z}\frac{\partial w'}{\partial z}
$$

$$
+\bar{\lambda}\frac{\partial w'}{\partial z}\frac{\partial\bar{u}}{\partial x}+\bar{\lambda}\frac{\partial w'}{\partial z}\frac{\partial\tilde{u}}{\partial x}+\bar{\lambda}\frac{\partial w'}{\partial z}\frac{\partial\bar{v}}{\partial y}+\bar{\lambda}\frac{\partial w'}{\partial z}\frac{\partial\tilde{v}}{\partial y}+\bar{\lambda}\frac{\partial w'}{\partial z}\frac{\partial\bar{w}}{\partial z}+\bar{\lambda}\left(\frac{\partial w'}{\partial z}\right)^2
$$

$$\lambda'\left(\frac{\partial\bar{u}}{\partial x}\right)^2+\lambda'\frac{\partial\bar{u}}{\partial x}\frac{\partial\tilde{u}}{\partial x}+\lambda'\frac{\partial\bar{u}}{\partial x}\frac{\partial\bar{u}}{\partial y}+\lambda'\frac{\partial\bar{u}}{\partial x}+\lambda'\frac{\partial\bar{u}}{\partial x}\frac{\partial\bar{w}}{\partial z}+\lambda'\frac{\partial\bar{u}}{\partial x}\frac{\partial w'}{\partial z}$$

$$+\lambda'\frac{\partial\tilde{u}}{\partial x}\frac{\partial\bar{u}}{\partial x}+\lambda'\left(\frac{\partial\tilde{u}}{\partial x}\right)^2+\lambda'\frac{\partial\tilde{u}}{\partial x}\frac{\partial\bar{v}}{\partial y}+\lambda'\frac{\partial\tilde{u}}{\partial x}\frac{\partial\tilde{v}}{\partial y}+\lambda'\frac{\partial\tilde{u}}{\partial x}\frac{\partial\bar{w}}{\partial z}+\lambda'\frac{\partial\tilde{u}}{\partial x}\frac{\partial w'}{\partial z}$$

$$+\lambda'\frac{\partial\bar{v}}{\partial y}\frac{\partial\bar{u}}{\partial x}+\lambda'\frac{\partial\tilde{v}}{\partial y}\frac{\partial\tilde{u}}{\partial x}+\lambda'\left(\frac{\partial\bar{v}}{\partial y}\right)^2+\lambda'\frac{\partial\bar{v}}{\partial y}\frac{\partial\tilde{v}}{\partial y}+\lambda'\frac{\partial\bar{v}}{\partial y}\frac{\partial\bar{w}}{\partial z}+\lambda'\frac{\partial\bar{v}}{\partial y}\frac{\partial w'}{\partial z}$$

$$+\lambda'\frac{\partial\tilde{v}}{\partial y}\frac{\partial\bar{u}}{\partial x}+\lambda'\frac{\partial\tilde{v}}{\partial y}\frac{\partial\tilde{v}}{\partial x}+\lambda'\frac{\partial\bar{v}}{\partial y}\frac{\partial\tilde{v}}{\partial y}+\lambda'\left(\frac{\partial\tilde{v}}{\partial y}\right)^2+\lambda'\frac{\partial\tilde{v}}{\partial y}\frac{\partial\bar{w}}{\partial z}+\lambda'\frac{\partial\tilde{v}}{\partial y}\frac{\partial w'}{\partial z}$$

$$+\lambda'\frac{\partial\bar{w}}{\partial z}\frac{\partial\bar{u}}{\partial x}+\lambda'\frac{\partial\bar{w}}{\partial z}\frac{\partial\tilde{u}}{\partial x}+\lambda'\frac{\partial\bar{w}}{\partial z}\frac{\partial\bar{v}}{\partial y}+\lambda'\frac{\partial\bar{w}}{\partial z}\frac{\partial\tilde{v}}{\partial y}+\lambda'\left(\frac{\partial\bar{w}}{\partial z}\right)^2+\lambda'\frac{\partial\bar{w}}{\partial z}\frac{\partial w'}{\partial z}$$

$$+\lambda'\frac{\partial w'}{\partial z}\frac{\partial\bar{u}}{\partial x}+\lambda'\frac{\partial w'}{\partial z}\frac{\partial\tilde{u}}{\partial x}+\lambda'\frac{\partial w'}{\partial z}\frac{\partial\bar{v}}{\partial y}+\lambda'\frac{\partial w'}{\partial z}\frac{\partial\tilde{v}}{\partial y}+\lambda'\frac{\partial w'}{\partial z}\frac{\partial\bar{w}}{\partial z}+\lambda'\left(\frac{\partial w'}{\partial z}\right)^2\Bigg]$$

Appendix C

PERMISSIONS

C.1 Theoretical and Computational Fluid Dynamics [1]

SPRINGER NATURE LICENSE
TERMS AND CONDITIONS

Dec 24, 2023

This Agreement between University of Delaware -- Tony Liang ("You") and Springer Nature ("Springer Nature") consists of your license details and the terms and conditions provided by Springer Nature and Copyright Clearance Center.

License Number	5695371248911
License date	Dec 24, 2023
Licensed Content Publisher	Springer Nature
Licensed Content Publication	Theoretical and Computational Fluid Dynamics
Licensed Content Title	On the inviscid energetics of Mack's first mode instability
Licensed Content Author	Tony Liang et al
Licensed Content Date	Dec 22, 2022
Type of Use	Thesis/Dissertation
Requestor type	academic/university or research institute
Format	print and electronic
Portion	full article/chapter
Will you be translating?	no

Circulation/distribution	1 - 29
Author of this Springer Nature content	yes
Title of new work	Multi-mode Instabilities Arising in Hypersonic Flow Conditions For Aerospace Applications
Institution name	University of Delaware
Expected presentation date	Jan 2024
Requestor Location	University of Delaware 130 Academy St. NEWARK, DE 19716 United States Attn: University of Delaware
Total	0.00 USD

Terms and Conditions

Springer Nature Customer Service Centre GmbH Terms and Conditions

The following terms and conditions ("Terms and Conditions") together with the terms specified in your [RightsLink] constitute the License ("License") between you as Licensee and Springer Nature Customer Service Centre GmbH as Licensor. By clicking 'accept' and completing the transaction for your use of the material ("Licensed Material"), you confirm your acceptance of and obligation to be bound by these Terms and Conditions.

1. Grant and Scope of License

1. 1. The Licensor grants you a personal, non-exclusive, non-transferable, non-sublicensable, revocable, world-wide License to reproduce, distribute, communicate to the public, make available, broadcast, electronically transmit or create derivative works using the Licensed Material for the purpose(s) specified in your RightsLink Licence Details only. Licenses are granted for the specific use requested in the order and for no other use, subject to these Terms and Conditions. You acknowledge and agree that the rights granted to you under this License do not include the right to modify, edit, translate, include in collective works, or create derivative works of the

Licensed Material in whole or in part unless expressly stated in your RightsLink Licence Details. You may use the Licensed Material only as permitted under this Agreement and will not reproduce, distribute, display, perform, or otherwise use or exploit any Licensed Material in any way, in whole or in part, except as expressly permitted by this License.

1. 2. You may only use the Licensed Content in the manner and to the extent permitted by these Terms and Conditions, by your RightsLink Licence Details and by any applicable laws.

1. 3. A separate license may be required for any additional use of the Licensed Material, e.g. where a license has been purchased for print use only, separate permission must be obtained for electronic re-use. Similarly, a License is only valid in the language selected and does not apply for editions in other languages unless additional translation rights have been granted separately in the License.

1. 4. Any content within the Licensed Material that is owned by third parties is expressly excluded from the License.

1. 5. Rights for additional reuses such as custom editions, computer/mobile applications, film or TV reuses and/or any other derivative rights requests require additional permission and may be subject to an additional fee. Please apply to journalpermissions@springernature.com or bookpermissions@springernature.com for these rights.

2. Reservation of Rights

Licensor reserves all rights not expressly granted to you under this License. You acknowledge and agree that nothing in this License limits or restricts Licensor's rights in or use of the Licensed Material in any way. Neither this License, nor any act, omission, or statement by Licensor or you, conveys any ownership right to you in any Licensed Material, or to any element or portion thereof. As between Licensor and you, Licensor owns and retains all right, title, and interest in and to the Licensed Material subject to the license granted in Section 1.1. Your permission to use the Licensed Material is expressly conditioned on you not impairing Licensor's or the applicable copyright owner's rights in the Licensed Material in any way.

3. Restrictions on use

3. 1. Minor editing privileges are allowed for adaptations for stylistic purposes or formatting purposes provided such alterations do not alter the original meaning or intention of the Licensed Material and the new figure(s) are still accurate and representative of the Licensed Material. Any other changes including but not limited to, cropping, adapting, and/or omitting material that affect the meaning, intention or moral rights of the author(s) are strictly prohibited.

3. 2. You must not use any Licensed Material as part of any design or trademark.

3. 3. Licensed Material may be used in Open Access Publications (OAP), but any such reuse must include a clear acknowledgment of this permission visible at the same time as the figures/tables/illustration or abstract and which must indicate that